

Conceptual Design Report

A Precision Measurement of the Neutral Pion Lifetime via the Primakoff Effect

Jefferson Lab Experiment E99-014

The PrimEx Collaboration

March 3, 2000

K. Baker, L. Gan, A. Gasparian (spokesperson and contact person),
 J. Goity, P. Gueye, C. Keppel, L. Tang
Hampton University, Hampton, VA

B. Asavapibhop, R. Hicks, K. Kumar, D. Lawrence, R. Miskimen (spokesperson),
 G. Peterson, J. Shaw
University of Massachusetts, Amherst, MA

A. Ahmidouch, S. Danagoulian (spokesperson), C. Jackson, S. Mtingwa
North Carolina A&T State University, Greensboro, NC

D. Dale (spokesperson), T. Gorringe, W. Korsch, V. Zeps, P. Zolnierczuk
University of Kentucky, Lexington, KY

E. Chudakoff, R. Ent, V. Gyurjyan, M. Ito, B. Wojtsekhowski,
 J.P. Chen, E. Smith
Thomas Jefferson National Accelerator Facility, Newport News, VA

A.M. Bernstein, D. Hasell, S. Kowalski, T. Lee
Massachusetts Institute of Technology, Cambridge, MA

D. Sober, H. Crannell
The Catholic University of America, Washington, DC

G. Davidenko, A. Dolgolenko, G. Dzyubenko, A. Evdokimov,
 M. Kubantsev, I. Larin, A. Sitnikov, V. Vishnyakov
Institute for Theoretical and Experimental Physics, Moscow, Russia

M. Khandaker, V. Punjabi, C. Salgado
Norfolk State University, Norfolk, VA

A. Nathan
University of Illinois, Urbana, IL

W. Briscoe, L. Murphy
George Washington University, Washington, DC

I. Aznauryan, H. Egiyan, S. Gevorgyan, A. Margaryan, K. Egiyan, S. Stepanyan,
 H. Voskanyan, A. Ketikyan, A. Shahinyan, Y. Sharabian, A. Petrosyan
Yerevan Physics Institute, Yerevan, Armenia

A. Glamazdin, A. Omelaenko
Kharkov Institute of Physics and Technology, Kharkov, Ukraine

A. Afanasev
North Carolina Central University, Durham, NC

B. Milbrath
Eastern Kentucky University, Richmond, KY

A.I. Fix, V.A. Tryasuchev
Tomsk Polytechnical University, Tomsk, Russia

R. Minehart, B. Stevens
University of Virginia, Charlottesville, VA

Contents

1	Executive Summary	4
2	Introduction	7
2.1	Physics Motivation	7
2.2	Previous experiments	8
2.2.1	The direct method	8
2.2.2	Measurements using $\gamma\gamma$ collisions	9
2.2.3	Measurements using the Primakoff effect	9
2.3	The Approved TJNAF Experiment	10
2.4	Utilization of the Apparatus for Future Measurements	11
2.4.1	$\eta(\eta') \rightarrow \gamma\gamma$ decay widths	11
2.4.2	Observation of Multi-photon Final States	12
2.4.3	Other Experiments at JLab	13
3	Experimental Instrumentation	21
3.1	Overview	21
3.2	The photon beam line	21
3.2.1	Beamline Instrumentation: Overview	24
3.2.2	Superharp	24
3.2.3	Intensity/Profile On-line Monitor	25
3.2.4	Estimated Budget	26
3.2.5	The Tagged Photon System	26
3.3	Luminosity Monitors	27
3.3.1	Photon Flux Calibration with a Total Absorption Counter	28
3.3.2	On-line Luminosity Monitoring – Pair Production	30
3.3.3	Pair production luminosity monitor dipole	31
3.3.4	Estimated Budget	31
3.4	Energy Calibration	37
3.5	Primakoff Targets	37
3.5.1	Measuring the target thickness	39
3.5.2	Estimated Budget	40
3.6	The Hybrid Calorimeter (HYCAL)	40
3.6.1	Lead Glass Detectors	41
3.6.2	Lead Tungstate Detectors	43
3.6.3	The Calorimeter Frame	43
3.6.4	Estimated Budget	46
3.6.5	Resolutions	46
3.7	The Charged Particle Veto	49
3.7.1	Estimated Budget	53
3.8	Gain Monitoring System	53
3.8.1	Laser performance requirements	55
3.8.2	Comparison of light sources	57

3.8.3	Estimated Budget	57
3.9	Data Acquisition Electronics	57
3.9.1	Simulations and results	61
3.9.2	Estimated Budget	66
4	Experimental Considerations	71
4.1	Count rate estimates and beamtime	71
4.2	Background rates	71
4.2.1	Accidentals	74
4.2.2	Correlated $\gamma\gamma$ backgrounds	78
4.2.3	π^0 backgrounds from the photon beamline	78
4.3	Pion final state interactions	80
4.4	Experimental uncertainties	86
5	Collaboration Management	93
6	Institutional Responsibilities	94
7	Milestone Schedule	95
8	Manpower Summary	97
9	Budget Summary	98
10	Summary	99

1 Executive Summary

Our collaboration has proposed a test of the most fundamental prediction of low energy QCD. We will perform a high precision measurement of the $\pi^0 \rightarrow \gamma\gamma$ decay rate which is dominated by the axial anomaly. This proposal was submitted to Jefferson Lab PAC15 and was approved with an A^- rating in January 1999. The experiment will measure the cross section for π^0 production with tagged photons incident on the Coulomb field of nuclei. The precision of this measurement will be $\simeq 1.4\%$. The experiment utilizes the Hall B photon tagger and requires a new detector for the $\pi^0 \rightarrow \gamma\gamma$ decay measurement. This document gives details of how the measurement will be performed, the accuracy that is required for each component, and the design of the required equipment. This includes the targets, beam monitoring systems, detector and electronics, as well as the manpower requirements, collaboration commitments, timetable, and costs. Some future extensions of the apparatus to related experiments are also given.

In the chiral limit, the predicted amplitude for the $\pi^0 \rightarrow \gamma\gamma$ decay rate is:

$$A_{\gamma\gamma} = \alpha N_c / (3\pi f_\pi) = 2.513 \cdot 10^{-2} GeV^{-1} \quad (1)$$

where N_c is the number of colors in QCD and $f_\pi = 92.42 MeV$ is the pion decay constant. The number given above is for the accepted value of $N_c = 3$. The predicted decay width is

$$\Gamma = m_\pi^3 |A_{\gamma\gamma}|^2 / (64\pi) = 7.725 eV. \quad (2)$$

The decay amplitude given above is exact in the chiral limit, *i.e.*, when the u- and d-quark masses vanish. In this case, the anomaly is saturated by the π^0 pole. However the real world current-quark masses are of the order of 5-7 MeV. There are several sources of corrections due to this explicit breaking of chiral symmetry. The most important one is a manifestation of the so-called non-renormalization theorem of the anomaly due to Adler and Bardeen, and does not change the form of the amplitude given above. It merely replaces the value of f_π in the chiral limit by the measured value determined from π^+ decay. The second type of correction stems from the mixing of the π^0 with the η and η' . An estimate of this correction gives an increase of about 2% in the π^0 width. Finally, other corrections due to contributions to the saturation of the chiral anomaly by heavier mesons (such as the π^0) can change the width of the π^0 by several parts per thousand.

Three general experimental techniques have been used to measure the π^0 radiative width; direct measurement of the lifetime through decay in flight, $\gamma\gamma$ collisions, and the Primakoff effect. The results of these experiments are not in good agreement. The result obtained from the most recent experiment, a direct decay measurement at CERN in 1985, is nearly two standard deviations below the value predicted from theory. The current experimental average cited by the Particle Data Group, 7.84 ± 0.56 eV, is in reasonable agreement with the predicted value. However, the present quality of the experimental knowledge of the width is not commensurate with the precision of the theoretical prediction. Given the importance of this process and the present state of experiment, it is clear that a new, high precision measurement of the π^0 radiative width is needed. A modern measurement at the 1.5%

accuracy level would fill this important experimental gap and would test the prediction of the axial anomaly at the present level of theoretical precision. This is arguably one of the most fundamental experiments that can be performed with few GeV electrons.

The experiment will measure the π^0 width via small angle coherent photoproduction of the π^0 in the Coulomb field of a nucleus, i.e. the Primakoff effect. This experiment will use tagged photons as the incident beam, and a hybrid detector consisting of lead glass and lead tungstate crystals to detect the two photons from the π^0 decays. A pair spectrometer that uses the physics production target as a converter will provide a measurement of the relative photon flux in the experiment.

The photon tagger in JLab Hall B will be used at an electron beam energy of 6 GeV. Only the highest 20% of photon energies from the tagger focal plane will be used, giving photon energies from 4.6 GeV to 5.7 GeV. This will be the first Primakoff measurement of the π^0 radiative width to use tagged photons; previous measurements have used untagged bremsstrahlung beams. The π^0 production targets are 5% radiation length of ^{12}C , ^{116}Sn , and ^{208}Pb placed downstream of the tagger magnet. Target thicknesses will be mapped to the level of 0.7% using an X-ray attenuation method. An important check on the systematic uncertainties will be provided by taking data on several targets over a range of tagged photon energies, thereby verifying that the data follow the Primakoff cross section predictions which vary as $Z^2 E^4$.

The Hybrid Calorimeter (HYCAL) will be a state-of-the art detector designed to provide precise position and energy measurements of the π^0 decay photons. It will consist of an array of 663 modules of $4.25 \times 4.25 \times 34 \text{ cm}^3$ lead glass Cherenkov detectors in a 28×28 matrix, with an inner array of 480 modules of $2.125 \times 2.125 \times 20.0 \text{ cm}^3$ lead tungstate (PbWO_4) crystal detectors in a 22×22 matrix. A ten element veto counter scintillator array in front of the HYCAL will be used to veto charged particles. The detector will be positioned 7.5 meters downstream of the production target, and will have a central $4.25 \times 4.25 \text{ cm}^2$ hole left open to enable the photon beam to pass through the detector. A light monitoring system based on a nitrogen pulsed laser and an optical fiber light distribution system will be used to monitor the gain stability of the 1,143 channels in the detector. The light monitoring system itself will be gain stabilized to the level of 0.2% using a feedback system based on an electro-optical crystal. Anticipated resolutions for 5.7 GeV incident photons are 3.3 MeV in two-photon invariant mass, 52 MeV in π^0 energy, and 0.016 degrees in π^0 angle.

Charged particles produced in the target are swept away from HYCAL by a 15 kG-m sweep dipole magnet on the beamline just downstream of the target. The photon flux will be monitored during data production runs by a pair spectrometer in front of HYCAL. The pair spectrometer uses the physics target as a converter, and the sweeping dipole placed just downstream of the target. Electrons and positrons will be detected on either side of the beam in a series of eight plastic scintillator telescopes on each side of the beamline. The pair spectrometer will be calibrated against the rates in a total absorption counter at low beam currents, and will provide continuous real time relative monitoring throughout the data taking.

The electronic trigger developed for HYCAL requires the detection of two photons with energies greater than 0.5 GeV. This provides high acceptance for π^0 events and high efficiency

for background rejection. The real data and background trigger rates are both estimated at the few Hz level.

Combining the estimated sources of error in quadrature gives a total error of 1.4% in the π^0 radiative width. The two largest contributions to the error are from uncertainties in the target thickness (0.7%) and the photon flux (1%). This CDR details how we intend to minimize these and other sources of errors. We believe the estimated errors are conservative, and that we should do no worse than a total uncertainty of 1.4% in the width. This will reduce the experimental error on the π^0 radiative width by approximately a factor of five from the PDG average, subjecting the most fundamental prediction of low energy QCD to a severe experimental test.

Under \$1.0 M in grant agency funds are requested to build and buy the detectors and electronics for this experiment. The largest parts of this are for HYCAL (\$416.0k) and the DAQ electronics (\$355.3k). In addition to this, Jefferson Lab will provide approximately \$402.0k for beam line devices and to prepare the Hall B infrastructure for the staging of this experiment. Fermi Lab will provide ADC's for the experiment at a cost of approximately \$168k. Brookhaven National Lab will provide the magnet and power supply for the sweep dipole at a cost of approximately \$87k. Commitments from members of the PrimEx collaboration total approximately \$823k, not including personnel or shop time. The largest part of this commitment is from ITEP for the use of their lead glass calorimeters to be used in the construction of HYCAL. Including funds from all sources, the total cost of the experiment is approximately \$2.2M.

The experimental apparatus described herein, in conjunction with the existing experimental equipment at Jefferson Lab, will be well suited to detecting photons and neutral mesons produced at low momentum transfer. For this reason, other experiments that might be performed with the proposed Primakoff facility are under investigation. A natural extension of the π^0 experiment is to measure the η and η' radiative widths. There has been a long standing disagreement between the Primakoff experiment of Browman *et al.* in 1974 and the $e^+e^- \rightarrow e^+e^-\eta$ experiments. For the η' there are no Primakoff measurements of the radiative width. Another possibility is to study final states with more than two photons, such as the $\gamma\gamma \rightarrow \pi^0\pi^0$ reaction. This reaction is generally considered to be an important theoretical laboratory for low energy QCD, with sensitivity to the π^0 polarizability.

We conclude that the prospects for an extended program of physics at Jefferson Lab using the proposed experimental apparatus are bright.

2 Introduction

2.1 Physics Motivation

The two-photon decay mode of the π^0 reveals one of the most profound symmetry issues in QCD, namely, the explicit breaking of a classical symmetry by the quantum fluctuations of the quark fields coupling to a gauge field[1]. This phenomenon, called anomalous symmetry breaking, is of pure quantum mechanical origin. In QCD, there are several observable phenomena that originate from anomalies. One is connected with the couplings of the quarks to the gluons. This is the so called axial anomaly by which the conservation of the axial U(1) symmetry of the classical Lagrangian of QCD is broken in the limit where two or more quarks are massless, and the divergence of the corresponding axial-vector current becomes proportional to the product $\vec{E}^a \cdot \vec{B}^a$ of the chromo-electric and chromo-magnetic fields. The axial anomaly of interest to us involves the corresponding coupling of the quarks to photons[2]. The π^0 couples to the isotriplet axial-vector current $\bar{q} I_3 \gamma_\mu \gamma_5 q$, where $q = (u, d)$, and I_3 is the third isospin generator. If we limit ourselves to two quark flavors, the electromagnetic current is given by $\bar{q} (1/6 + I_3/2) \gamma_\mu q$. When coupling to the photon, the isosinglet and isotriplet components of the electromagnetic current lead to an anomaly that explicitly breaks the symmetry associated with the axial-vector current $\bar{q} I_3 \gamma_\mu \gamma_5 q$, and this in turn directly affects the coupling of the π^0 to two photons. The predicted anomalous decay amplitude is given by [1, 2]:

$$A_{\gamma\gamma} = \alpha N_c / (3\pi f_\pi) = 2.513 \cdot 10^{-2} GeV^{-1} \quad (3)$$

where N_c is the number of colors in QCD, and $f_\pi = 92.42 \pm 0.25 MeV$ [3] is the pion decay constant. The number given above is for the accepted value of $N_c = 3$.

The width of the $\pi^0 \rightarrow \gamma\gamma$ decay predicted by the anomaly is

$$\Gamma = m_\pi^3 |A_{\gamma\gamma}|^2 / (64\pi) = 7.725 \pm 0.044 eV, \quad (4)$$

with a 0.6% uncertainty due to the experimental error in f_π . The current experimental value is $7.84 \pm 0.56 eV$ [3] and is in good agreement with the predicted value. This number is an average of several experiments[3] which will be discussed in Sec. 2.

The decay amplitude given above is exact in the chiral limit, *i.e.*, when the u- and d-quark masses vanish. In this case, the anomaly is saturated by the π^0 pole. However, the real world current-quark masses are of the order of 7 MeV. There are two sources of corrections due to this explicit breaking of chiral symmetry. The first and most important does not change the form of the amplitude given above. It merely replaces the value of f_π in the chiral limit by the measured value determined from π^+ decay[4, 5]. This is a manifestation of the so-called non-renormalization theorem of the anomaly due to Adler and Bardeen. The second correction is due to the mixing of the π^0 with the η and the η' . A calculation based on the assumption that the decay constant of the η' is equal to f_π , and on values of the quark mass ratios $(m_u - m_d)/m_s$ and $(m_u - m_d)/(m_u + m_d)$ estimated in several ways, shows that these mixings can add up to 2.5% to the π^0 width. A further correction can be induced by terms in the $O(p^6)$ chiral Lagrangian. Such terms would emerge from corrections to the saturation

of the anomaly by excited mesons such as the π' . These contributions are suppressed by a factor of m_q/m_{meson} , and would thus be of the order of a few parts per thousand to 1%. Estimates of $O(p^6)$ terms have been done in Nambu-Jona-Lasinio type models[6], finding an increase in the π^0 width of 0.8% to 1.3%. Thus, an increase of the π^0 width of the order of 2 to 3% due to chiral symmetry breaking of the quark masses seems quite likely.

In conclusion, the theoretical prediction of $\Gamma(\pi^0 \rightarrow \gamma\gamma)$ by the axial anomaly[1, 2] is the most accurate prediction in QCD, and depends only on the number of colors. The contributions to this decay from higher order (quark mass) terms are of the order of $\simeq 2\%$ and are calculable. The present experimental knowledge of this rate is at the $\simeq 10\%$ level, and in view of the importance of this prediction, it should be tested to a level of accuracy which is consistent with the theoretical uncertainties. The proposed measurement at the $\simeq 1.4\%$ accuracy level fills this important experimental gap, and is arguably one of the most fundamental experiments that can be performed with few GeV electrons.

2.2 Previous experiments

In view of the fundamental nature of the axial anomaly, it is important to measure the π^0 lifetime as accurately as possible. The present experimental knowledge of the $\pi^0 \rightarrow \gamma\gamma$ width is summarized in figure 1, along with the projected error of our proposed experiment. In this figure the predictions of the axial anomaly (equation 2) with the $\simeq 2\%$ theoretical uncertainty[7] due to loop corrections are presented. Three experimental techniques have been used to measure the neutral pion width: the direct method, $\gamma\gamma$ collisions, and the Primakoff effect. In addition, a future experiment planned for Hall A at TJNAF [8] will measure the slope of the pion form factor $F_{\gamma\gamma^*\pi^0}(q^2)$ at low q^2 using the small angle scattering capabilities of the Hall A Møller polarimeter.

2.2.1 The direct method

A direct measurement of the π^0 lifetime can be made by observation of the decay distance between the production and decay points. This has proven difficult because of the high spatial resolution which is required due to the short lifetime, $\tau \simeq 10^{-16}$ sec. To be able to discern distinct production and decay points, one must take advantage of relativistic time dilation to have the pion survive long enough in the laboratory frame. Additionally, good knowledge of the energy distribution of the produced pions is necessary in order to extract the lifetime via this method.

The first measurement utilizing such a technique was performed at the CERN PS in 1963 [17]. The precision achieved was 17%. This experiment is not used in the particle data book average. In 1985, an improved version of this technique was employed at the CERN SPS. In this experiment, a 450 GeV/c proton impinged upon two tungsten foils whose separation was variable. The first foil served as the π^0 production target, and the second foil converted the π^0 decay photons to electron-positron pairs which were subsequently detected. For a small foil separation, some of the π^0 's decayed after the second foil, whereas for a large separation, essentially all of the π^0 's decayed before the second foil. Thus, by measuring the positron rates for three different foil spacings ranging from 5 to 250 μ m,

the authors were able to determine the lifetime. The dominant systematic errors arise from uncertainties in the π^0 spectrum which was not measured but was assumed to be the arithmetic mean of the π^+ and π^- spectra. In addition, corrections had to be made for the Dalitz decay of the π^0 's, conversion of the photons in the π^0 production target, prompt positron and photon production, and positrons from the decay of η 's. A pion lifetime of $\tau_{\pi^0} = (0.897 \pm 0.022 \pm 0.017) \times 10^{-16}$ seconds was obtained[9], corresponding to a width of $\Gamma_{\pi^0} = (7.34 \pm 0.18 \pm 0.11)$ eV.

It is interesting to note that this experiment, the most precise of those performed to date, gives a result which is smaller than the chiral anomaly prediction[1, 2]. Also note that the loop corrections tend to increase the predicted width. As such, this experiment provides impetus for a more precise measurement employing a different technique.

2.2.2 Measurements using $\gamma\gamma$ collisions

The π^0 width has been measured using electron-positron collisions at DESY via $e^+e^- \rightarrow e^+e^-\gamma^*\gamma^* \rightarrow e^+e^-\pi^0 \rightarrow e^+e^-\gamma\gamma$ [16]. The incident leptons are scattered at very small angles and are not detected in the final state. In so doing, they radiate quasi-real photons that couple to the π^0 which is subsequently identified in an invariant $\gamma\gamma$ mass spectrum. The photons were detected using the Crystal Ball detector which consisted of a large array of NaI(Tl) crystals providing 93% solid angle coverage. Contributions to the systematic error included luminosity normalization, detector efficiencies, cosmic ray rejection, and beam-gas collisions. The latter effect arises from the production of π^0 's via the interaction of the leptons with the residual gas in the beam pipe. The resulting width obtained was $\Gamma_{\pi^0} = (7.7 \pm 0.5 \pm 0.5)$ eV, very close to the prediction of the anomaly but with a relatively large error. The value obtained in this experiment is the same as the Particle Data Book average but was not included in this average[3].

2.2.3 Measurements using the Primakoff effect

The Primakoff effect, *i.e.* photopion production from the Coulomb field of a nucleus (see figure 2)[10], has been used in a number of experiments to study the π^0 lifetime [11, 12, 13, 14]. The production of π^0 's in the Coulomb field of a nucleus by real photons is essentially the inverse of the decay $\pi^0 \rightarrow \gamma\gamma$, and the cross section for this process thus provides a measure of the π^0 lifetime.

Using bremsstrahlung beams of energy 4.4 GeV and 6.6 GeV at Cornell, Browman *et al.* [11] measured the Primakoff cross sections on several nuclei, and obtained a total decay width of $\Gamma_{\pi^0} = (8.02 \pm 0.42)$ eV. However, as was pointed out in [7, 16] the quoted error, does not have any contribution from uncertainties in the luminosity or detection efficiency (see Table 1 of [11]), and is an underestimate. An analogous measurement of the η width [15] using the Primakoff effect employing a very similar setup and analysis techniques is not in agreement with other experiments.

The other two Primakoff measurements shown in figure 1 were performed with bremsstrahlung beams of 1.5 and 2.0 GeV at DESY[12] and 1.1 GeV at Tomsk[13]. From figure 1 it can be seen that the DESY measurement is high compared to the theoretical prediction

and the Particle Data Book average. Although both of these measurements have relatively large errors they were included in the Particle Data Book Average[3]. An older Primakoff experiment performed with 0.95 and 1.0 GeV bremsstrahlung beams at Frascati[14] has not been included in the Particle Data Book average and is not shown in figure 1.

In view of the strong interest in the subject, the dispersion of the previous results, and the recent availability of high intensity, high energy tagged photon beams, a high precision, state-of-the-art measurement of the π^0 lifetime is desirable. In particular, the Hall B tagged photon facility at TJNAF will enable a measurement which will offer two distinct advantages over previous measurements involving bremsstrahlung beams: (1) the quasi-monochromatic nature of the tagged beam will enable a clean kinematical separation of the Primakoff mechanism from various background processes, and (2) the tagging technique will enable significantly better control of systematic errors associated with the photon flux normalization.

2.3 The Approved TJNAF Experiment

We plan to use the quasi-monochromatic photons of energy 4.6-5.7 GeV from the Hall B photon tagging facility to measure the absolute cross section of small angle π^0 photoproduction from the Coulomb field of complex nuclei. The invariant mass and angle of the pion will be reconstructed by detecting the π^0 decay photons from the $\pi^0 \rightarrow \gamma\gamma$ reaction.

For unpolarized photons, the Primakoff cross section is given by[12]:

$$\frac{d^3\sigma_P}{d\Omega} = \Gamma_{\gamma\gamma} \frac{8\alpha Z^2 \beta^3 E^4}{m^3 Q^4} |F_{e.m.}(Q)|^2 \sin^2\theta_\pi \quad (5)$$

where $\Gamma_{\gamma\gamma}$ is the pion decay width, Z is the atomic number, m , β , θ_π are the mass, velocity and production angle of the pion, E is the energy of incoming photon, Q is the momentum transfer to the nucleus, and $F_{e.m.}(Q)$ is the nuclear electromagnetic form factor, corrected for final state interactions of the outgoing pion.

As the Primakoff effect is not the only mechanism for pion photoproduction at high energies, some care must be taken to isolate it from competing processes. In particular, the full cross section is given by:

$$\frac{d^3\sigma}{d\Omega_\pi} = \frac{d\sigma_P}{d\Omega} + \frac{d\sigma_C}{d\Omega} + \frac{d\sigma_I}{d\Omega} + 2 \cdot \sqrt{\frac{d\sigma_P}{d\Omega} \cdot \frac{d\sigma_C}{d\Omega}} \cos(\phi_1 + \phi_2) \quad (6)$$

where the Primakoff cross section, $\frac{d\sigma_P}{d\Omega}$, is given by equation (3). The nuclear coherent cross section is given by:

$$\frac{d\sigma_C}{d\Omega} = C \cdot A^2 |F_N(Q)|^2 \sin^2\theta_\pi \quad (7)$$

and the incoherent cross section is:

$$\frac{d\sigma_I}{d\Omega} = \xi A(1 - G(Q)) \frac{d\sigma_H}{d\Omega} \quad (8)$$

where A is the nucleon number, $C \sin^2\theta_\pi$ is the square of the isospin and spin independent part of the neutral meson photoproduction amplitude on a single nucleon, $|F_N(Q)|$ is the

form factor for the nuclear matter distribution in the nucleus, (corrected for final state interactions of the outgoing pion), ξ is the absorption factor of the incoherently produced pions, $1 - G(Q)$ is a factor which reduces the cross section at small momentum transfer due to the Pauli exclusion principle, and $\frac{d\sigma_H}{d\Omega}$ is the π^0 photoproduction cross section on a single nucleon. The relative phase between the Primakoff and nuclear coherent amplitudes without final state interactions is given by ϕ_1 , and the phase shift of the outgoing pion due to final state interactions in the final state is given by ϕ_2 .

Kinematical considerations enable one to separate the Primakoff effect from other photopion production mechanisms. The Primakoff cross section is zero for pions emitted along the incident photon direction, has a sharp maximum at an angle $\theta_\pi \sim m_\pi^2/2E_\pi^2$, and falls rapidly to zero at larger angles. It is proportional to Z^2 , and its peak value is roughly proportional to E^4 . The nuclear coherent cross section for spin zero nuclei is also zero in the forward direction, but has a broad maximum outside the angular region of the Primakoff effect, and falls at larger angles as shown in figures 3 and 4, where the amplitudes are normalized to the Cornell data[11], and distortion effects are included. It is expected to vary little with energy[12]. Measurements of the nuclear effects at larger angles are necessary to determine the unknown parameters in the production mechanism and thus make an empirical determination of the nuclear contribution in the Primakoff peak region. Consequently, this experiment requires a π^0 detector with good angular resolution to eliminate nuclear coherent production, and good energy resolution in the decay photon detection will enable an invariant mass cut to suppress multi-photon backgrounds.

We are planning to take extensive data to test the experimental accuracy of the proposed measurements. These are based on the fact that the production of neutral pions via the Primakoff effect is primarily an electromagnetic phenomenon and, therefore, can be accurately calculated. The main features of the Primakoff effect (listed above) will be used to test the accuracy of our data: 1) We will take data with sufficient angular resolution to check the shape of the Primakoff peak after the coherent nuclear and nuclear-Primakoff interference amplitudes, which will be determined empirically by larger angle data, have been subtracted; 2) three spin zero targets (^{12}C , ^{116}Sn , ^{208}Pb) will be used. These have form factors which have been well studied by electron scattering experiments, and can be used to test the Z^2 dependence of the cross section; and 3) the E^4 dependence of the cross section will be measured in the energy range from 4.6 to 5.7 GeV. The study of the Primakoff peak as a function of these three variables should add a great deal of confidence to the measurement, and can be used to empirically determine the systematic errors.

2.4 Utilization of the Apparatus for Future Measurements

2.4.1 $\eta(\eta') \rightarrow \gamma\gamma$ decay widths

The apparatus we are constructing to measure the π^0 lifetime can be used for other measurements. The most straightforward extension is to measure the two photon width for the η meson. We are also exploring the possibility of measuring the two photon η' decay width. These decays are also dominated by the anomaly. Furthermore, the relatively large mass of the η' has a subtle effect on the anomaly[18]. In addition, there is the effect of SU(3)

breaking which causes π, η, η' mixing[1, 5]. As mentioned previously, this caused a theoretical increase of $\simeq 2\%$ in the π^0 width and much larger changes in the η and η' widths[1]. The precise experimental determination of the η and $\eta' \rightarrow \gamma\gamma$ widths, leading to a good determination of the $\eta - \eta'$ mixing angle, would have a strong impact on the study of isospin breaking through the $\eta \rightarrow \pi\pi\pi$ decay, whose absolute rate is determined using the $\eta \rightarrow \gamma\gamma$ width. The present experimental knowledge of the η meson width is presented in figure 5[3]. Most of the measurements in the figure have been done using two photon interactions in e^+e^- collisions. There is one exception which is the Cornell measurement of the η width[15] by the Primakoff effect. This gives a width which is significantly lower than those from e^+e^- collisions. This is the companion measurement to the π^0 width. It can be seen that all points from the e^+e^- collision data are in reasonable agreement with each other but not with the Primakoff measurement of the η [15]. As such, the η width should be remeasured by the Primakoff process using state-of-the-art experimental techniques.

The horizontal lines in figure 5 show the sensitivity of the η two photon decay width to the $\eta - \eta'$ mixing angle. Venugopal and Holstein[19] have determined the $\eta - \eta'$ mixing angle by simultaneously fitting data from η, η' reactions involving the anomaly- $\eta, \eta' \rightarrow \gamma\gamma, \pi^+\pi^-\gamma$. Their result, $\theta = -20.8^\circ \pm 3.2^\circ$, is shown in the figure. An improved measurement, such as that currently under study by the PrimEx collaboration, could provide an important constraint on this parameter.

The cross sections for the Primakoff effect to produce the η on ${}^4\text{He}$ and ${}^{12}\text{C}$ nuclei are presented in figure 6 and figure 7. Compared to the Primakoff effect to produce the π^0 , the η production has a significantly smaller cross section, and peaks at larger production angles. This is a consequence of the much larger mass of the η which significantly increases the momentum transfer at a given production angle. As a result the Primakoff peak is harder to distinguish from the nuclear coherent peak. One possible solution is to use lighter targets, such as ${}^4\text{He}$ or ${}^{12}\text{C}$, or a combination of these two.

2.4.2 Observation of Multi-photon Final States

The experimental equipment that we are planning to construct includes luminosity monitors, a highly segmented photon detector to observe the $\pi^0 \rightarrow \gamma\gamma$ decay photons at small angles, and a plastic scintillator to veto charged particles. This apparatus is thus highly efficient at detecting photons and light neutral mesons produced at low t (four momentum transfer). It is, therefore, quite suitable to observe processes in which the tagged incident photons produce multiple photons in the final state. This possibility leads to an interesting variety of observable multi-photon processes. Using virtual photons from the target we could observe the $\gamma\gamma \rightarrow \pi^0\pi^0$ reaction by making observations near the photon pole at $t = 0$. Some theoretical reasons for interest in this reaction include the possibility of measuring the π^0 polarizability[20] and checking the dynamical predictions of chiral perturbation theory[21, 22]. We also note that there have been some older two photon production experiments using the $e^+e^- \rightarrow e^+e^-\pi\pi$ reaction with both charged and neutral pions in the final state. The previous data are skimpy but there are plans at Frascati to perform more measurements, particularly for charged pion final states[22]. The possible future TJNAF effort in this field

would be complementary to the plans at Frascati.

An interesting variation on the axial anomaly theme is the diagram in which the incident photon interacts with a virtual π^0 from the target to produce an outgoing photon. This is the diagram for the $\pi^0 \rightarrow \gamma\gamma$ reaction turned on its side and is dominated by the axial anomaly. Physically this is the anomaly contribution to Compton scattering from the nucleon and is an integral part of this process. Isolation of this diagram by extrapolation to the pion pole at the unphysical point $t = m_\pi^2$ can lead to a measurement of this contribution to Compton scattering from the proton.

As was discussed in the previous section, the coherent production of neutral pions from the target nuclei is a background for the measurement of the π^0 lifetime. However, it is an interesting physical process in its own right. For example it can be used to measure the matter distribution of nuclei. When this is compared to the accurately measured charge distribution from electron scattering and μ mesic X-rays, one can obtain the neutron distribution. For this purpose one would have to extend our proposed measurement to include proton and ${}^4\text{He}$ targets to measure the $\gamma N \rightarrow \pi^0 N$ amplitudes. This relatively small extension of our experiment could lead to interesting results.

2.4.3 Other Experiments at JLab

We are also exploring ways in which a highly segmented electromagnetic calorimeter can be utilized in ongoing studies of baryon structure at TJNAF. In particular, the recent measurement of G_{E_p}/G_{M_p} by recoil polarization in Hall A (experiment 93-027) has revealed a significant difference in the Q^2 -dependence of the elastic electric and magnetic form factors of the proton starting at 1 GeV^2 and continuing to the highest Q^2 of the measurement at 3.5 GeV^2 [23]. Prior to this experiment, the uncertainties in G_{E_p} data were too large for the Q^2 -dependence of the data to be distinguished from the simple dipole shape.

An experiment was approved by TJNAF PAC15 (E-99-007) to extend the measurement of the G_{E_p}/G_{M_p} ratio to 5.6 GeV^2 in Hall A, where the maximum Q^2 is limited by the maximum momentum of the Hall A spectrometers. In view of the great scientific interest in extending these measurements to higher Q^2 , the FPP collaboration submitted a letter of intent to TJNAF PAC16 to measure G_{E_p}/G_{M_p} in Hall C in a Q^2 range of 6.5 to 9 GeV^2 . This letter of intent was favorably received by the PAC.

This measurement will require a new focal plane polarimeter in the HMS. In order to optimize the experiment, the solid angle of the electron arm will be matched to that of the HMS proton arm. Increasing Q^2 requires a large acceptance, non-magnetic detector for the scattered electron, such as the one being planned for the π^0 lifetime measurement. The high Q^2 G_{E_p}/G_{M_p} experiment is projected to run in 2004 or thereafter. The two collaborations are presently discussing the possibility of making use of the π^0 calorimeter for such future G_{E_p}/G_{M_p} measurements.

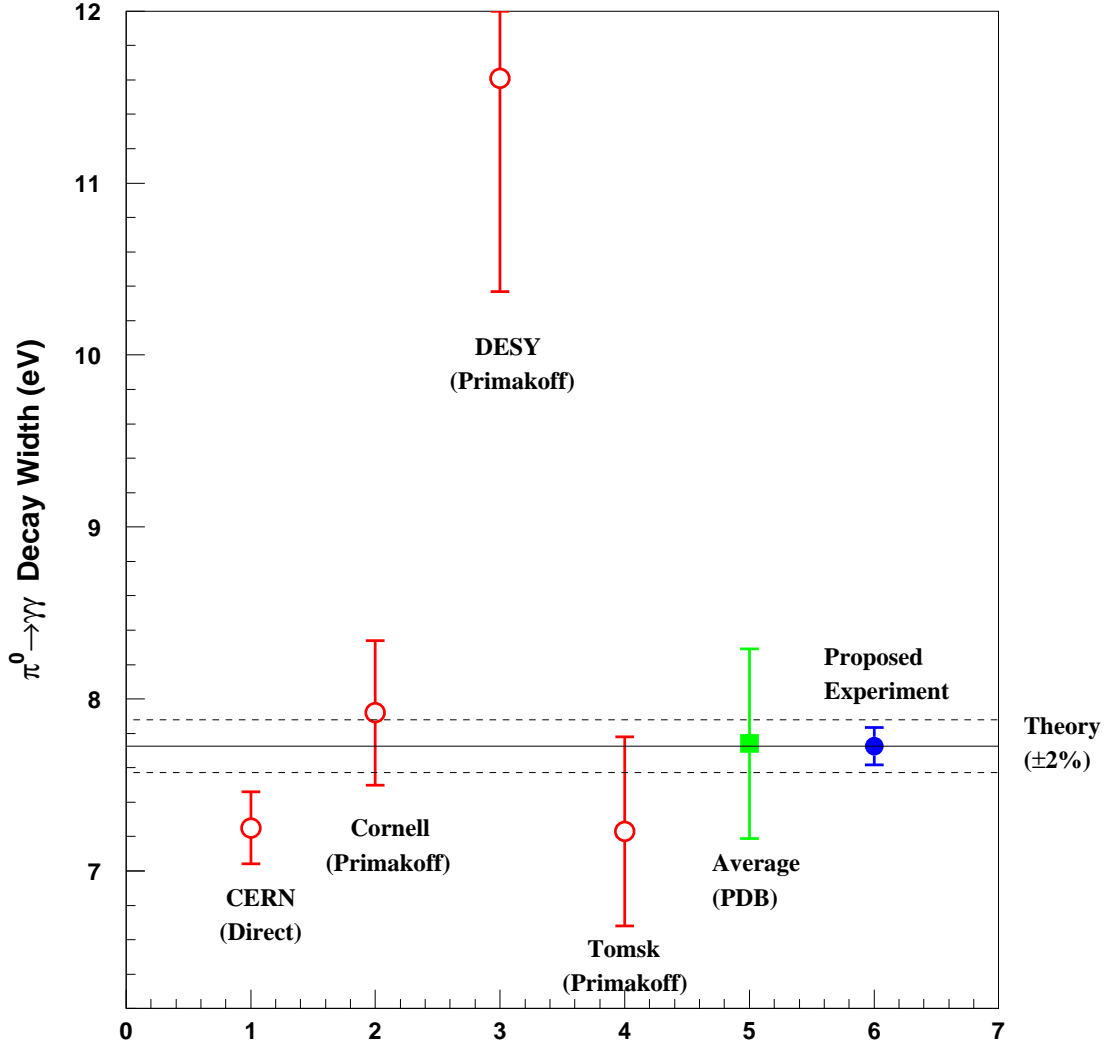


Figure 1: $\pi^0 \rightarrow \gamma\gamma$ decay width in eV. The horizontal line is the prediction of the axial anomaly (Eq. 2) [1, 2] with an estimated 2% error [7]. The experimental results with errors are for: 1) the direct method [9]; 2,3,4) the Primakoff method [11, 12, 13]; 5) Particle Data Book Average [3]; 6) the expected error for our future experiment, arbitrarily plotted to agree with the predicted value.

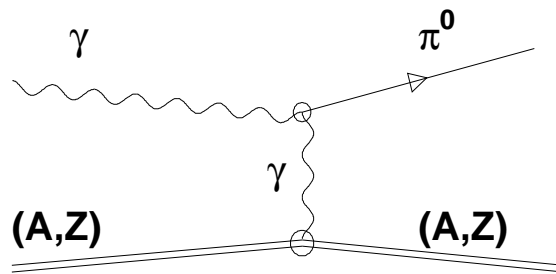


Figure 2: Schematic representation of the Coulomb photoproduction of neutral pions (Primakoff effect).

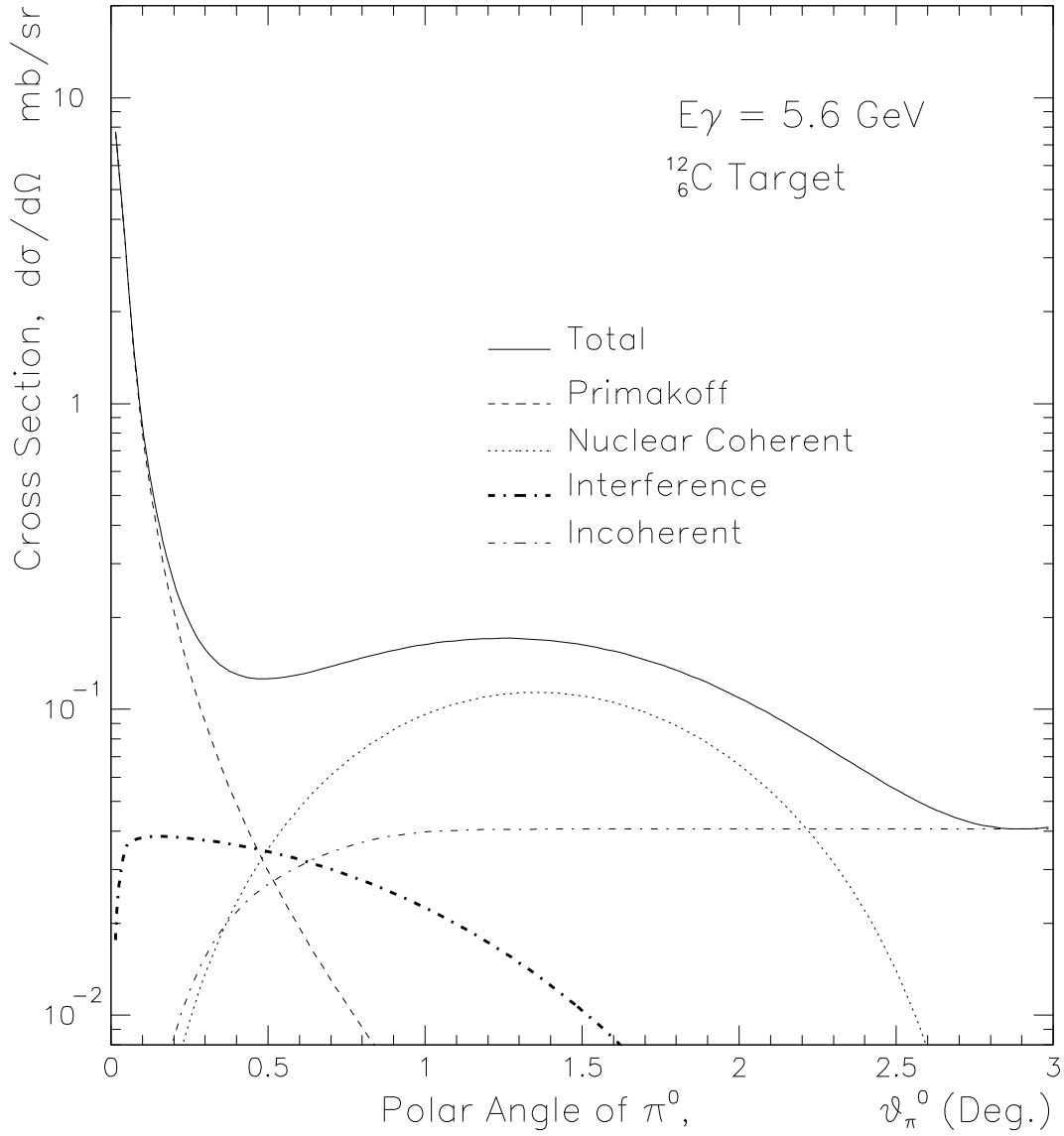


Figure 3: Angular behavior of the electromagnetic and nuclear π^0 photoproduction cross sections for ^{12}C in the 6.0 GeV energy range.

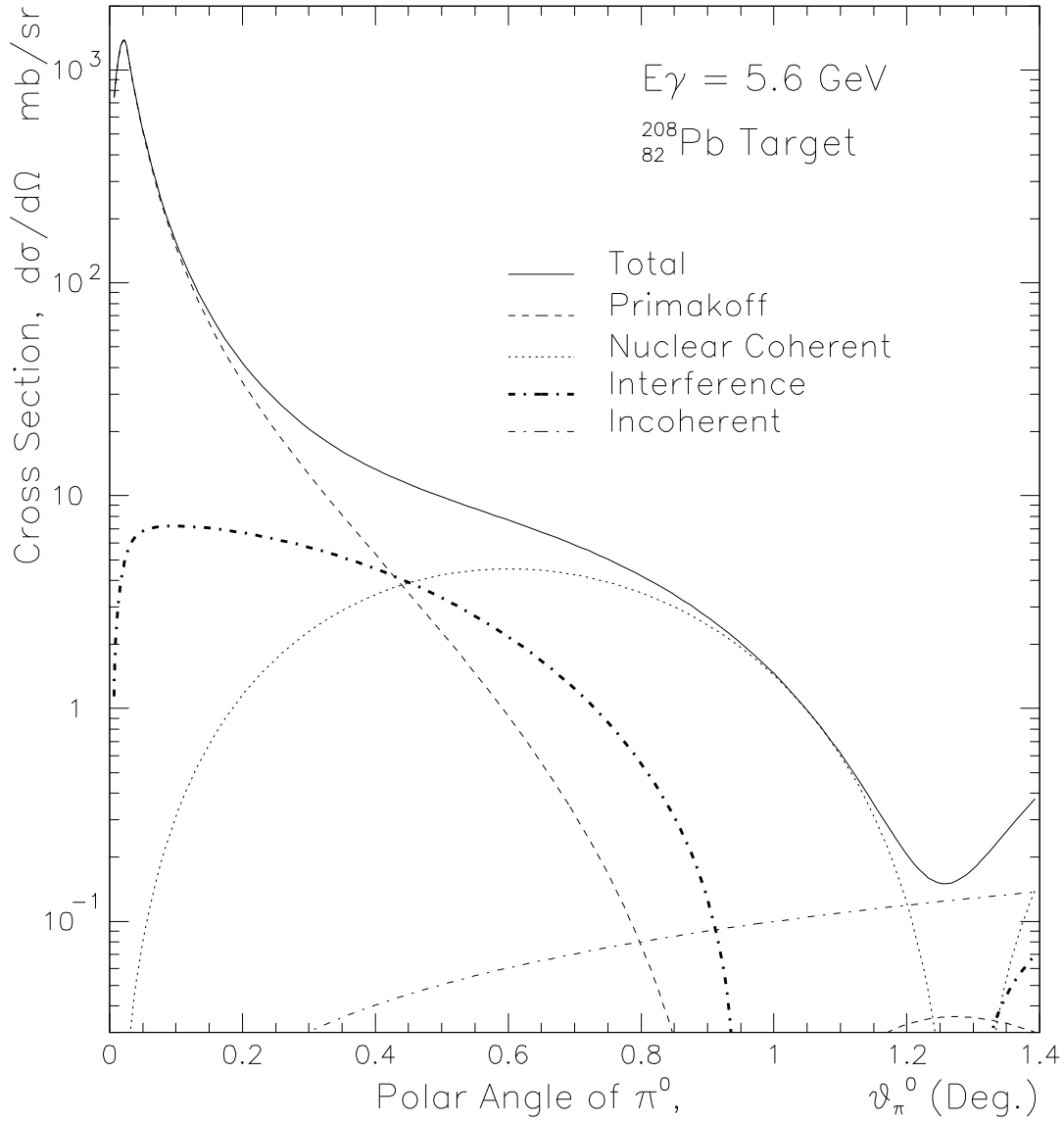


Figure 4: Angular behavior of the electromagnetic and nuclear π^0 photoproduction cross sections for ^{208}Pb in the 6.0 GeV energy range.

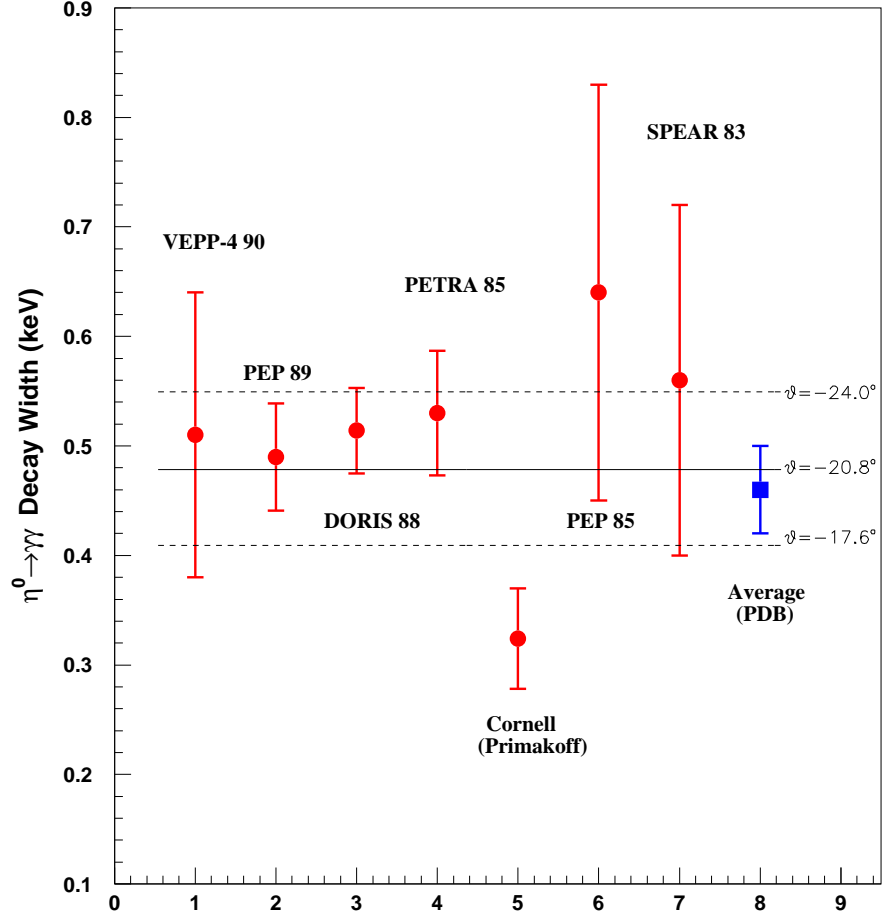


Figure 5: Two-photon decay width for the η meson. Points 1 through 4, as well as 6 and 7 are the results of e^+e^- collisions (for references, see[3]), point 5 is the result of a Primakoff experiment[15]. Point 8 is the Particle Data Book[3] average based on first five points. The plotted uncertainties combine the statistical and systematic errors in quadrature. The three lines are the widths for different η - η' mixing angles as indicated. See reference[19].

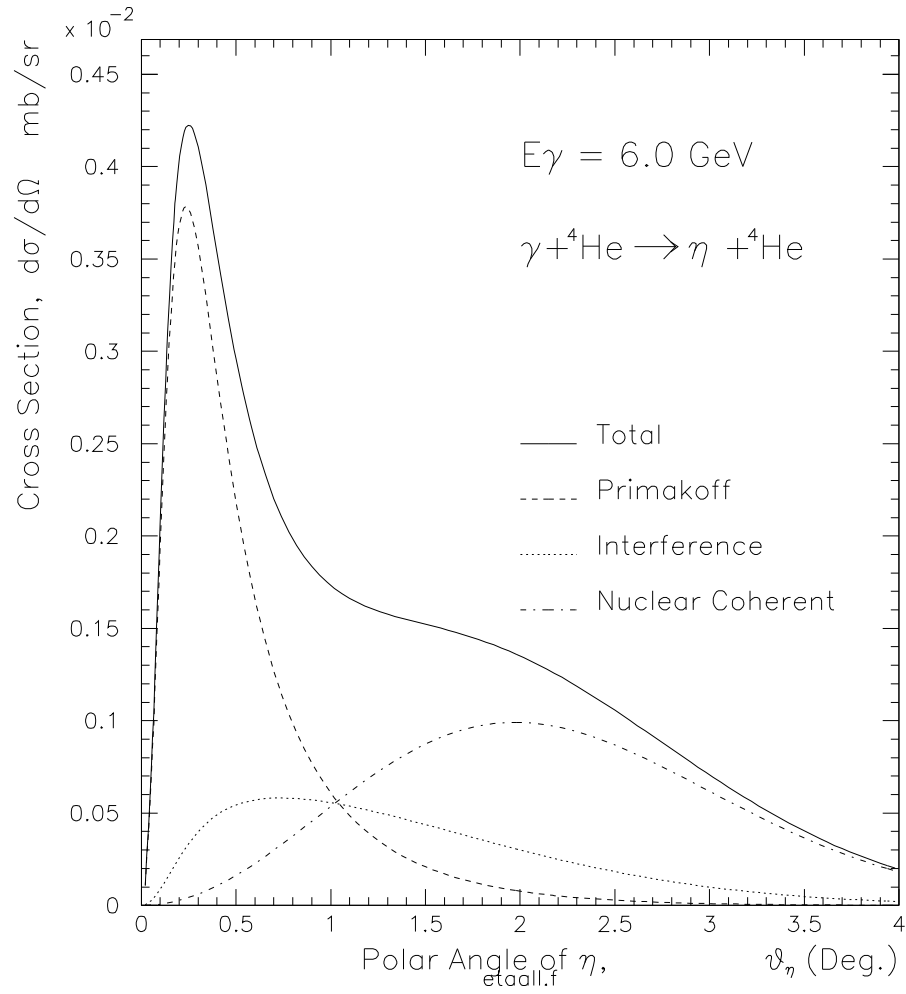


Figure 6: Angular behavior of the electromagnetic and nuclear η^0 photoproduction cross sections for ${}^4\text{He}$ at 6.0 GeV.

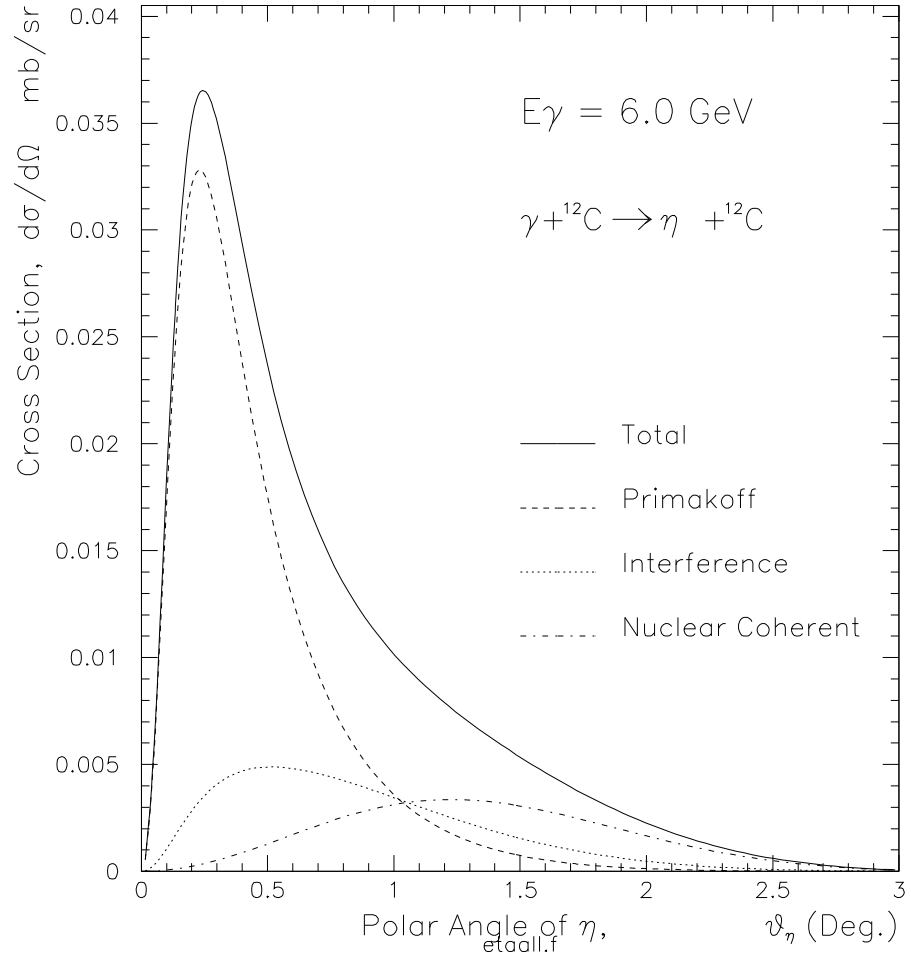


Figure 7: Angular behavior of the electromagnetic and nuclear η^0 photoproduction cross sections for ${}^{12}\text{C}$ at 6.0 GeV.

3 Experimental Instrumentation

3.1 Overview

The primary experimental equipment required in this experiment includes: (1) the Hall B photon tagger; (2) 5% radiation length solid π^0 production targets (^{12}C , ^{116}Sn , and ^{208}Pb); (3) a pair production luminosity monitor located just downstream of the π^0 production target; (4) a $1\text{m} \times 1\text{m}$ highly segmented lead glass photon detector for π^0 decay photons with a high resolution insertion in the central region near the beam, and a plastic scintillator charged particle veto. (See figure 8.)

3.2 The photon beam line

Photons produced in the bremsstrahlung radiator by a 6 GeV electron beam will pass through the 6 cm pole gap of the tagger magnet and then through a 7.5 cm diameter beam pipe. The collimator which is normally used in Hall B experiments will be moved out of position, so that there is no obstruction within 3.75 cm of the beam line until the photon beam hits the Primakoff target approximately 6.5 meters from the radiator. Thus, the photon beam is unobstructed out to an angle of about $70 m_e/E_e$. Electron beam scans at the position of the radiator are carried out routinely in Hall B experiments, and have shown no measurable halo. For this experiment, we will remove the two sweep magnets and the secondary collimator currently on the beam line. We also plan to install a new superharp scanner at the position of the target. A relatively thick wire will be moved through the photon beam, and secondary particles will be detected downstream using the pair spectrometer system which is described in more detail below. Figure 9 shows a GEANT simulation of the beam profile at the Primakoff target position for a 1.5×10^{-3} radiation length gold bremsstrahlung converter. Figure 9(a) shows the beam profile for the full bremsstrahlung beam, and figure 9(b) shows the profile for the high energy component of the beam, $E_\gamma > 5$ GeV, where it can be seen that the expected beam spot is about 1.4 mm. The simulation was checked against the beam profile measured at Bonn[40] using a 1.5×10^{-3} radiation length gold foil and a 1 GeV beam. Excellent agreement was obtained.

A photon beam is established in Hall B by centering the electron beam in the two BPM monitors upstream of the radiator, and then checking the position and width of the photon beam spot in the pair counter. The pair counter is located in the downstream “alcove” of Hall B, approximately 50 m downstream of the radiator. It consists of two pairs of counters oriented at plus or minus 45 degrees with respect to the horizontal axis. These two sets of pairs have a small overlap ($\sim 1\text{mm}$). By requiring a coincidence between the two counters one effectively has a 1mm scintillator. By moving the pair counter device through the beam (via a stepper motor), recording the motor position and the coincidence count rate, the photon beam profile in the U and V directions can be measured.

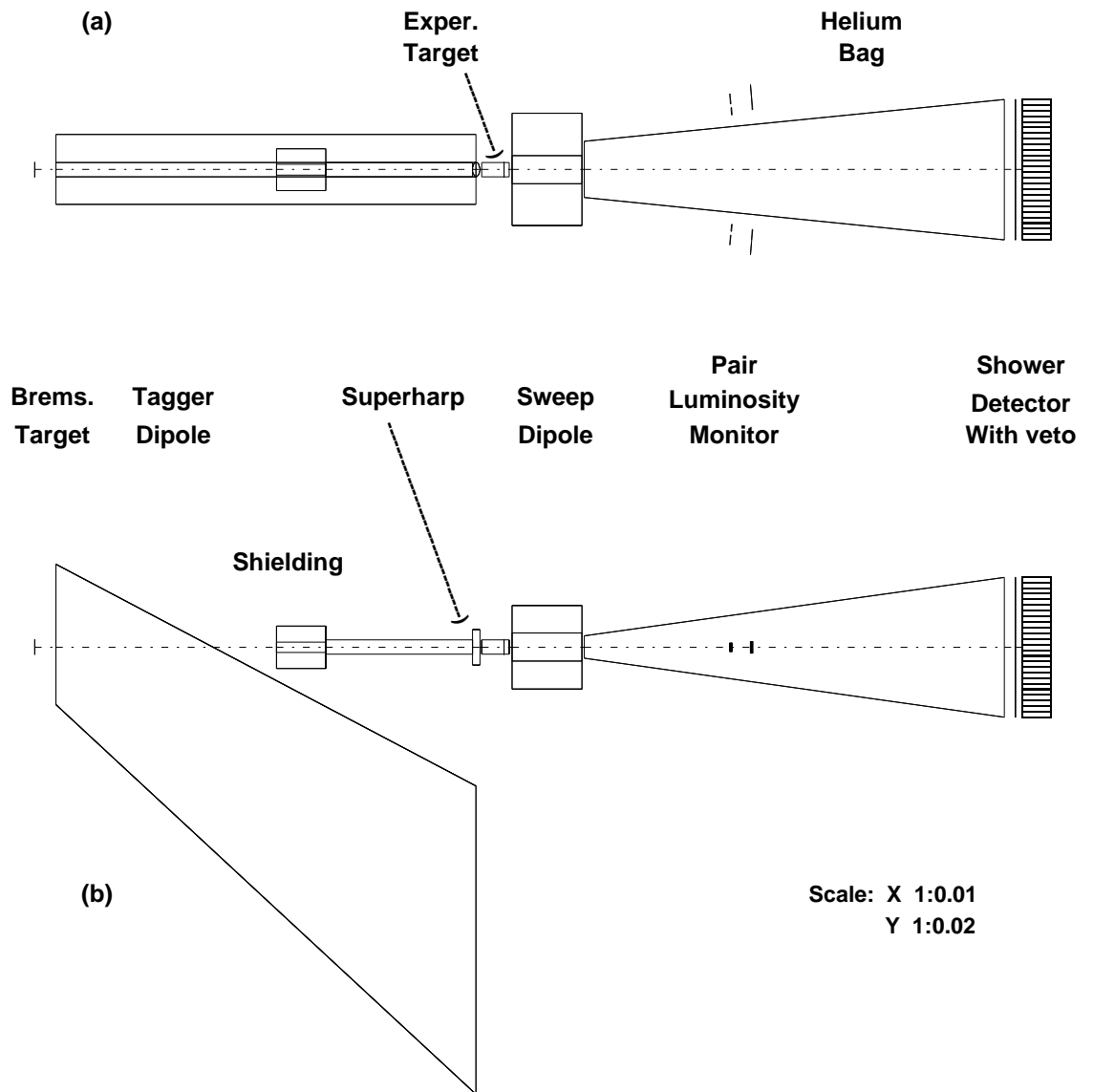


Figure 8: Layout of the experimental setup. (a) Top view. (b) Side view.

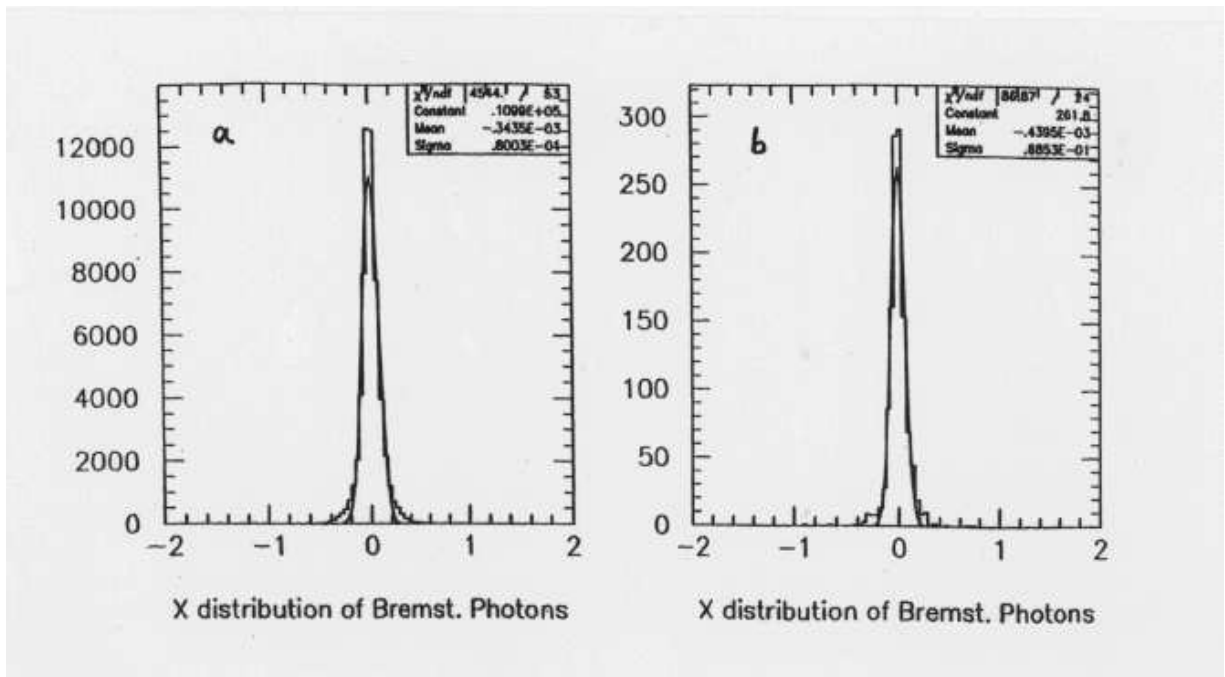


Figure 9: Simulated beam profile at the Primakoff target. (a), Full bremsstrahlung beam. (b), $E_\gamma > 5$ GeV. The x axis is in centimeters.

3.2.1 Beamline Instrumentation: Overview

The beamline for this experiment includes the Hall B electron beamline, the bremsstrahlung tagging system and the photon beamline. The following beam control instrumentation will be employed: two electron beam position and current monitors upstream of the tagger, a superharp scanner for photon beam position and profile control at the nuclear targets, a pair production luminosity monitor, and an on-line intensity/profile monitor.

In order to fulfill the systematic uncertainty requirements of the experiment, the following aspects of the beamline instrumentation will be considered:

- Electron beam energy, position, emittance, intensity and energy stability control.
- γ beam intensity, position and profile control.
- Luminosity control.
- Background control (including neutral background).
- Linearity and stability of monitors with beam intensity.

The beamline section upstream of and including the pair production luminosity monitor magnet will be in vacuum, and the section from the exit window of the luminosity monitor dipole to the calorimeter will have a helium bag.

The pair production luminosity monitor consists of a dipole magnet (which is at the same time a sweeping magnet) and a symmetric set of scintillator telescopes on both sides of the beamline to detect e^+e^- pairs produced in the nuclear target by photons over the full tagged photon energy range of the experiment. The scintillator telescopes will also be used in the beam profile measurement with the superharp.

3.2.2 Superharp

The superharp will be located in front of the Primakoff production target. The main components of the superharp are: a fork with three tungsten wires, a stepper motor with an accuracy of motion of about $10 \mu m$, an encoder and a particle detector consisting of the scintillator telescopes of the luminosity monitor as mentioned above in coincidence or singles mode. The fork is positioned at 45° with respect to the horizontal and moves in the plane perpendicular to the beamline. The distance between two arms of the fork is 1 inch. Three wires are positioned between arms in such a way that the first and the third wires are vertical and move in the horizontal direction across the beam, and the intermediate wire is horizontal and moves in the vertical direction when the fork advances at 45° . When the wire crosses the beam, beam particles scatter from the wire or produce e^+e^- pairs, which are analyzed in the magnetic field of the pair spectrometer dipole and detected in the scintillator telescopes. Using the information from the encoder, one can construct a scanning plot which represents the number of counts versus the wire position. This plot provides the vertical and horizontal beam profile distributions.

Below are some of characteristics of Hall C superharp system:

- spatial resolution: better than $10\mu\text{m}$;
- scan rate: ≥ 5 mm/sec;
- DAQ frequency: 60 Hz;
- wire thickness: $\sim 5\%$ rad. length ($\sim 175\mu\text{m}$ of tungsten).

The expected counting rates are shown below. We take the photon beam spot size equal to $800\mu\text{m}$ (standard deviation of normal distribution). If the wire is stationary in the middle of the beam spot, the rates will be:

- singles: 47 kHz;
- coincidences: 8 kHz.

During the scanning, at a DAQ rate of 60 Hz the mean integrated time of data acquisition per point is on the order of 16ms. The number of e^+ 's (or e^- 's) detected in one arm of the telescope in singles mode during this time is ~ 800 , the number of coincident e^+e^- 's is ~ 120 . The distance covered by the wire during this time is $\sim 83\mu\text{m}$. For the indicated size of the beam spot, we will have about 10 points with a total of ~ 8000 singles and ~ 1200 coincidences. This monitor is beam destructive and cannot be used for continuous measurements.

3.2.3 Intensity/Profile On-line Monitor

For on-line control of the relative intensity and profile of the photon beam, we will need a detector which can provide continuous real time information during the data acquisition period, as well as information in the data stream for off-line analysis.

The following requirements must be imposed on a such detector system.

- Low-sensitivity to background.
- Linearity within the intensity range $N_\gamma = (10^4 - 10^7)/s$.
- Fast ($\tau \approx 10$ ns).
- Spatial resolution: $\sim 100\mu\text{m}$.

The collaboration plans to construct a fission fragment detector based low pressure wire proportional chambers[73]. This monitor will be located downstream of the calorimeter and will detect fission fragments produced in the secondary target by beam photons. The detected fragments are efficiently separated from other particles created by the beam, making it insensitive to background. The detector has good timing, 130 ps (FWHM), and position, $100\mu\text{m}$, resolutions. It has high rate capabilities, up to $10^5/s/mm^2$ and high resistance to radiation damage. Since the fission production probability is proportional to the beam intensity, this device will serve as both a beam profile and a relative luminosity monitor.

item	number	PrimEx Request	JLab	Other
On-line profile monitor				
with electronics	1	\$15.0k		
Motor drivers	3		\$0.9k	
Power supply	1		\$0.5k	
Motor controller	1		\$2.0k	
Superharp	1		\$2.6k	
Target ladder	1		\$8.0k	
Dipole	1			\$27.4k (BNL)
Dipole power supply	1			\$55.6k (BNL)
Dipole and power supply shipping			\$5.0k	
Dipole and power supply refurbishing and installation			\$15.0k	
Dipole vacuum box	1		\$15.0k	
Helium bag	1	\$10.0k		
Total		\$25.0k	\$49.0k	83.0k

Table 1: Estimated budget for beamline equipment.

3.2.4 Estimated Budget

Table 1 shows the estimated budget for the PrimEx beamline instrumentation.

3.2.5 The Tagged Photon System

The primary advantages of the experiment being proposed here over the previous Primakoff experiments [11, 12, 13, 38] arise from the possibility of using the Jefferson Lab Hall B tagging facility to carefully control systematic errors and reduce backgrounds.

First, the tagging technique will enable a significantly more accurate knowledge of the photon flux. We estimate that it can be controlled to better than 1% by taking the steps described here. Second, due to the strong energy dependence of the Primakoff cross section (E^4), it is critical to have a good knowledge of the absolute photon beam energy. In the untagged case of reference [11], it was known to 0.5% and created a 3% uncertainty in the decay width. We anticipate a factor of five reduction in the energy uncertainty at Jefferson Lab as compared to reference [11].

We will use a 6 GeV electron beam incident on a thin (10^{-4} radiation length) bremsstrahlung converter foil. The post-bremsstrahlung electrons will be momentum analyzed in the Hall B photon tagger magnet [39], and photons will be tagged in the energy range from 4.6 to 5.7 GeV. (See figure 10). The Hall B bremsstrahlung photon tagging system is equipped with a system of detectors which spans the photon energy range of 20% to 95% of the incident electron energy. The detector system consists of two planes of counters: 384 overlapping scintillators which define 767 fine energy channels of width $0.001 E_e$ (the “E” counters), and 61 larger scintillators, each read out by two photomultiplier tubes and designed for good time resolution (the “T” counters). The sizes of the T-counters are designed to produce

approximately equal counting rates in two groups. When all 61 T-counters are used, the total tagging rate can be as high as 50 MHz for the whole focal plane. Counters T1-T19, which span the photon energy range from 77% to 95% of E_e , are proportionally smaller than the others, and will allow a tagging rate of up to 50 MHz in this region alone. This experiment will use only the “high-rate” counters T1-T19. The tagger trigger signal will be formed by taking the coincidence of the left and right PMT’s of the T-counters, while the tagger Master OR (MOR) will be produced by ORing the T-counter coincidence channels.

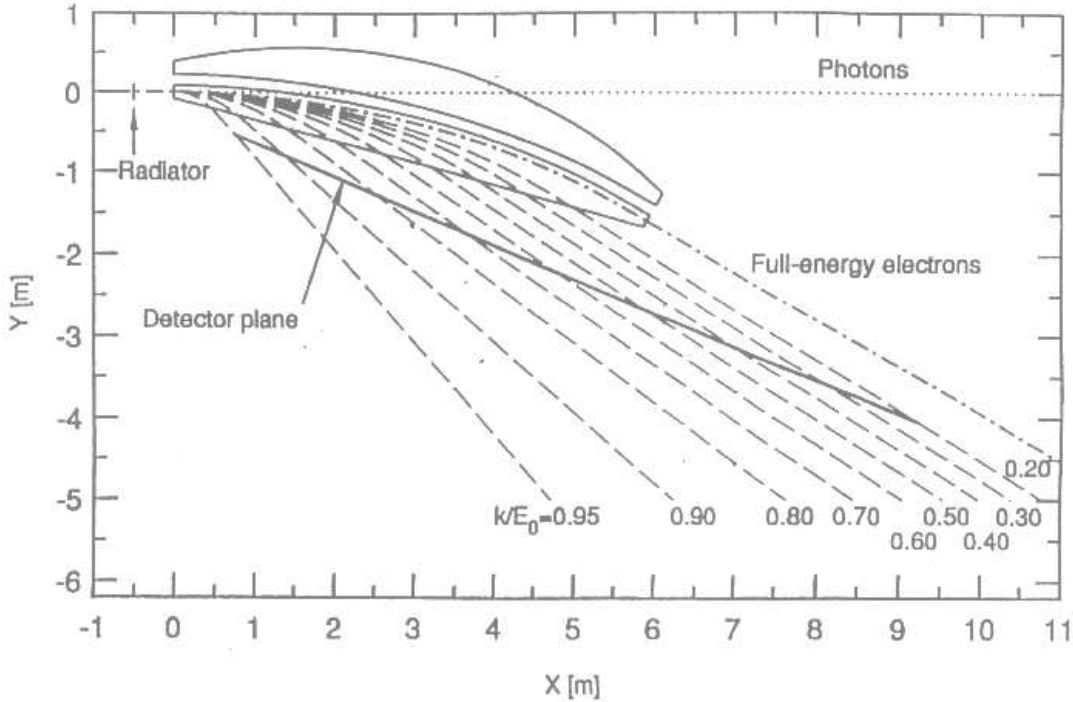


Figure 10: Side view of the Hall B photon tagging system. (Figure is from [39])

3.3 Luminosity Monitors

Control of the luminosity to about 1% is crucial in performing a precision measurement of the π^0 lifetime. The ideal luminosity monitor will:

- (1) Give absolute luminosity.
- (2) Work at the high photon intensities of the production data taking.
- (3) Monitor both photon flux and target thickness.

- (4) Be a non-destructive, on-line luminosity monitor in place during data taking.

Our approach will be to use several complementary techniques to tightly control the luminosity, the most important one being the use of a total absorption counter.

3.3.1 Photon Flux Calibration with a Total Absorption Counter

Since each π^0 decay event is measured in coincidence with a tagging counter signal, the normalization of the cross section to the incident photon flux depends on knowing the number of tagged photons on target in each energy bin during the run. The number of tagged photons on target is not necessarily equal to the number of events recorded by the tagging counters because of a number of effects:

- (1) events in which a bremsstrahlung photon is produced but is absorbed before reaching the target.
- (2) Møller scattering events in the bremsstrahlung radiator which produce an electron in the tagging counters without an accompanying photon.
- (3) Extra post bremsstrahlung electrons registered due to room background.

Events of the first type will be minimized by allowing the entire bremsstrahlung beam to travel in vacuum without collimation to the target. The second category of events is known to affect the tagging rate at the level of a few percent. The combination of these first two effects can be measured by performing a calibration run in which the Primakoff target is removed and a lead glass total absorption counter (TAC) is placed in the photon beam just after the vacuum window downstream of the Primakoff target position. The ratio of Tagger·TAC coincidences to tagger events, the so called tagging efficiency, is then recorded.

Such measurements were made during the photofission experiment performed in Hall B in April 1998. Typically, these measurements are made with a 2×10^{-5} radiation length radiator and 0.1 nA beam current. The trigger was the tagger Master OR. Figure 11 shows this tagging efficiency ratio at a beam energy of 4.0 GeV. The measured ratio is above 98% except near the endpoint, where the Møller scattering effect is most significant.

Knowing this ratio, one can determine the photon flux in the data taking run by counting the number of post bremsstrahlung electrons in a given tagging counter:

$$N_{\gamma}^{tagged}(experiment) = N_e(experiment) \times \frac{N_{\gamma}^{tagged}(calibration)}{N_e(calibration)} \quad (9)$$

One can then determine the cross section from the tagged yield of π^0 's:

$$\text{TaggedYield} = \frac{d\sigma}{d\Omega} \times t \times \Delta\Omega \times N_e(experiment) \times \frac{N_{\gamma}^{tagged}(calibration)}{N_e(calibration)}, \quad (10)$$

where t is the target thickness, and $\Delta\Omega$ is the solid angle of the pion detector. In the calibration run, the total absorption counter rate is limited, and, therefore, the tagging

Tagger Efficiency at 4.0 GeV - No Collimation (April 1998)

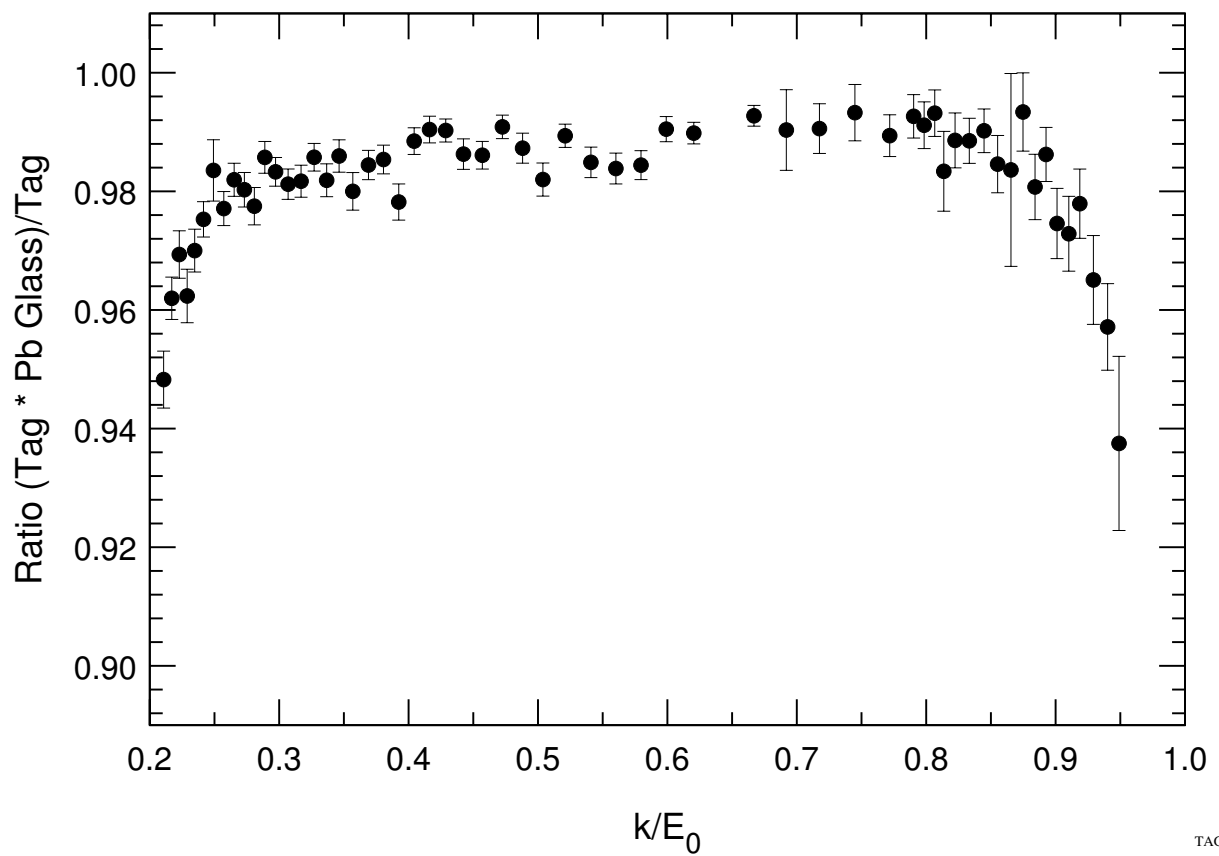


Figure 11: Tagging efficiency across the focal plane of the Hall B tagger as measured in April 1998. The beam energy is 4.0 GeV.

TAGEFFK.PLT
11-10-98

efficiency must be measured at a rate which is reduced by a factor of about one hundred as compared to the data taking run. As such, any rate dependence in the tagging efficiency must be considered. Note that in equation 10, both the tagged yield (coincidence of π^0 and tagging electron) and $N_e(\text{experiment})$ (number of tagging electrons) are both affected by the deadtime associated with the tagging counters in a similar fashion.

Extra electrons in the tagging counter due to room background can arise from:

- (1) Natural background radiation and any activation in and around the tagging focal plane.
- (2) Radiation associated with the transport to the beam dump of that part of the electron beam which did not produce bremsstrahlung photons.
- (3) Room background from the photon beam as it interacts in the physics target and the Hall.

The counting rate due to natural background radiation and activation is expected to be relatively constant in time, and can be measured at intervals with the beam off. This is especially important when calibration runs are performed, as the rates in the tagging counters will be low then. Backgrounds directly associated with the beam will be measured in a series of tests in which the bremsstrahlung converter foil thickness and electron beam current are each varied by an order of magnitude such that their product is constant. This will keep the photon flux in the room constant but vary the current of the beam going to the beam dump enabling effect (2) to be separated from (3).

3.3.2 On-line Luminosity Monitoring – Pair Production

The use of the total absorption counter to calibrate the number of photons per tagging electron will provide an absolute calibration of the photon flux incident on the π^0 production target. However, these measurements will be performed at intervals throughout the data taking, and will by necessity be performed at an electron beam current which is two orders of magnitude less than the production data taking runs. Consequently, we plan to construct a pair production luminosity monitor which will measure the relative tagged photon flux over a range of intensities, and will operate continuously throughout the data taking runs. This monitor will be used in addition to the previously mentioned photofission based system.

The pair spectrometer will use the physics target as a converter, and will make use of a 15 kgauss-meter dipole magnet placed just downstream of it. The electrons and positrons will be detected on either side of the beam in a series of eight plastic scintillator telescopes. The requirements of the pair spectrometer are that it must operate over the entire range of intensities (of both the flux calibration and data taking runs) and have a smooth, relatively flat acceptance in E_γ covering the entire tagging range. A layout of the proposed pair spectrometer with one simulated pair production event is shown in figure 12. Each arm will consist of eight telescopes with overlapping momentum acceptances constructed from 0.5cm thick plastic scintillators placed symmetrically on either side of the beamline. The solid angle defining aperture is 3.5m downstream of the Primakoff target and is twenty-eight centimeters in size in the dispersive direction.

Figure 13 shows the expected efficiency of the device as a function of photon energy. Figure 14 shows the energy distribution of electrons when an e^+e^- coincidence condition is imposed. The expected singles rates are 100kHz per telescope, and the total coincidence rate is expected to be 140kHz. A schematic of the pair spectrometer data acquisition electronics logic is shown in figure 15. In addition to counting (T counter) - (pair spectrometer) coincidences, we will also measure T-counter-pair spectrometer delayed coincidences for accidental subtraction.

A number of measurements will be performed to ensure proper control of luminosity:

- (1) With the physics target (5% radiation length) in place, the ratio of the number of tagged e^+e^- pairs to the number of postbremsstrahlung electrons, $N_{e^+e^-}^{tagged}/N_e$, will be measured as a function of rate for each tagging counter. This is to check for linearity of the pair spectrometer - tagging counter system.
- (2) $N_{e^+e^-}^{tagged}/N_e$ will also be measured for each tagging counter with a very thin target to reduce the pair spectrometer rates. This will check deadtime effects in the pair spectrometer.
- (3) Measure the tagging efficiency with the total absorption counter as described above to calibrate the absolute scale of the pair production monitor.

In addition to these steps, the collaboration is also investigating the possibility of using electron Compton scattering in the Primakoff target as an absolute measurement of the luminosity. This will make use of the kinematical correlation of the photon energy and angle of the scattered photon, which will be detected in the HYCAL calorimeter described below.

3.3.3 Pair production luminosity monitor dipole

An 18D36 (MKII) dipole has been obtained on loan from Brookhaven National Laboratory to be used in the pair production luminosity monitor. Both the dipole and its associated power supply are currently on-site at Jefferson Lab. This dipole normally has a six inch gap which can be expanded by adding two iron spacers. The magnet on loan from BNL has spacers such that its gap is 8.125 inches which is adequate for this experiment. Figure 16 shows a TOSCA calculation of the magnetic field in the median plane of the magnet. A vacuum box will be inserted into the gap of the dipole. This will be part of the common vacuum including the Primakoff target and the bremsstrahlung converter. On the downstream side of the magnet will be an aluminum vacuum window composed of *5mil* 2024 aircraft aluminum (0.14% radiation lengths). Particles will exit the magnet via this window, and will pass through a helium bag on their way to either the Hybrid Calorimeter pion detector or to the pair production luminosity monitor detectors.

3.3.4 Estimated Budget

An estimated budget for the pair production luminosity monitor is shown in table 2. The University of Kentucky will provide manpower and shop facilities at no charge to the project

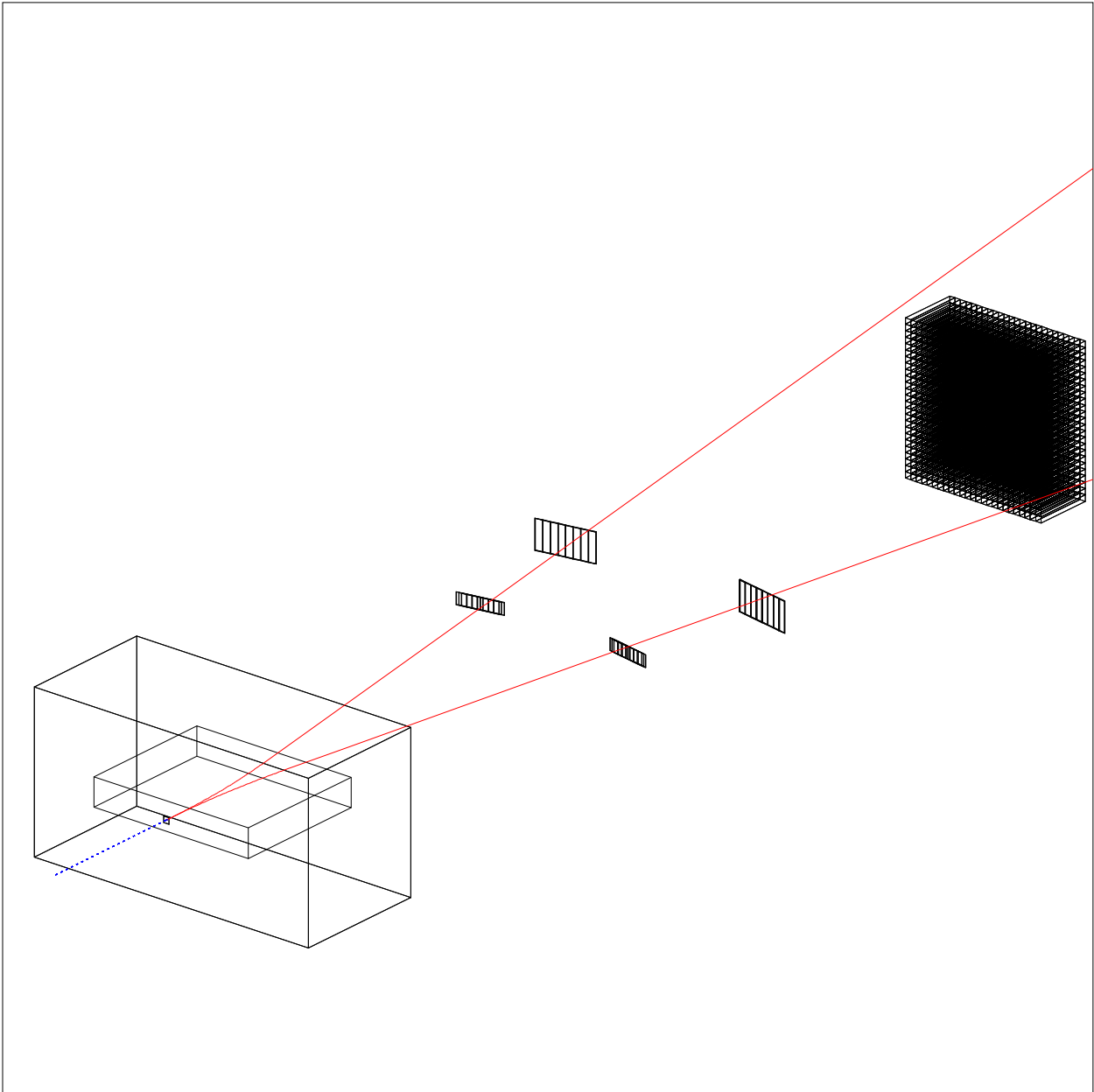


Figure 12: Layout of the proposed luminosity monitor and one pair production event. Each detector arm is segmented into eight contiguous plastic scintillator telescopes.

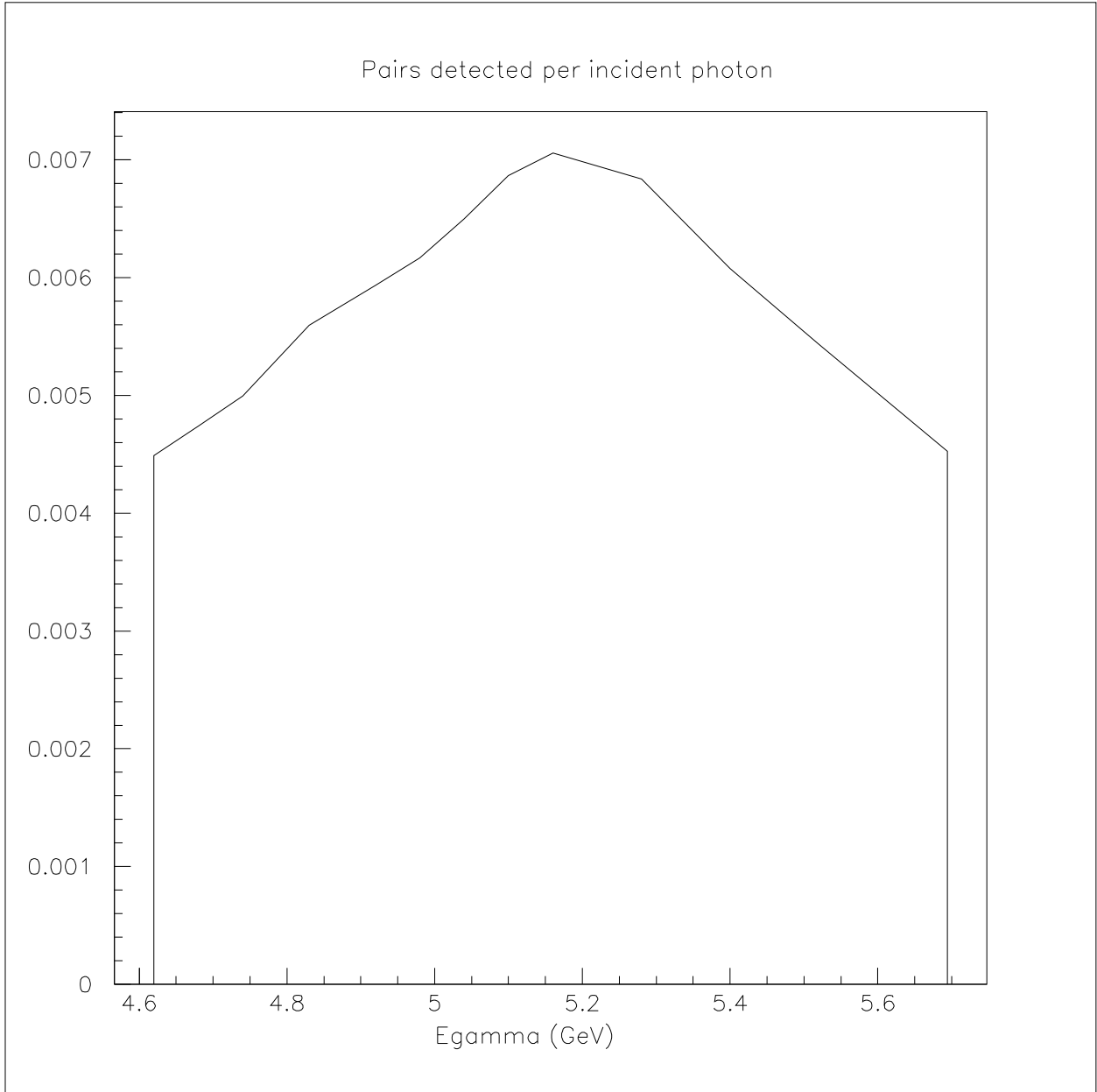


Figure 13: Efficiency of the pair production luminosity monitor *versus* E_γ .

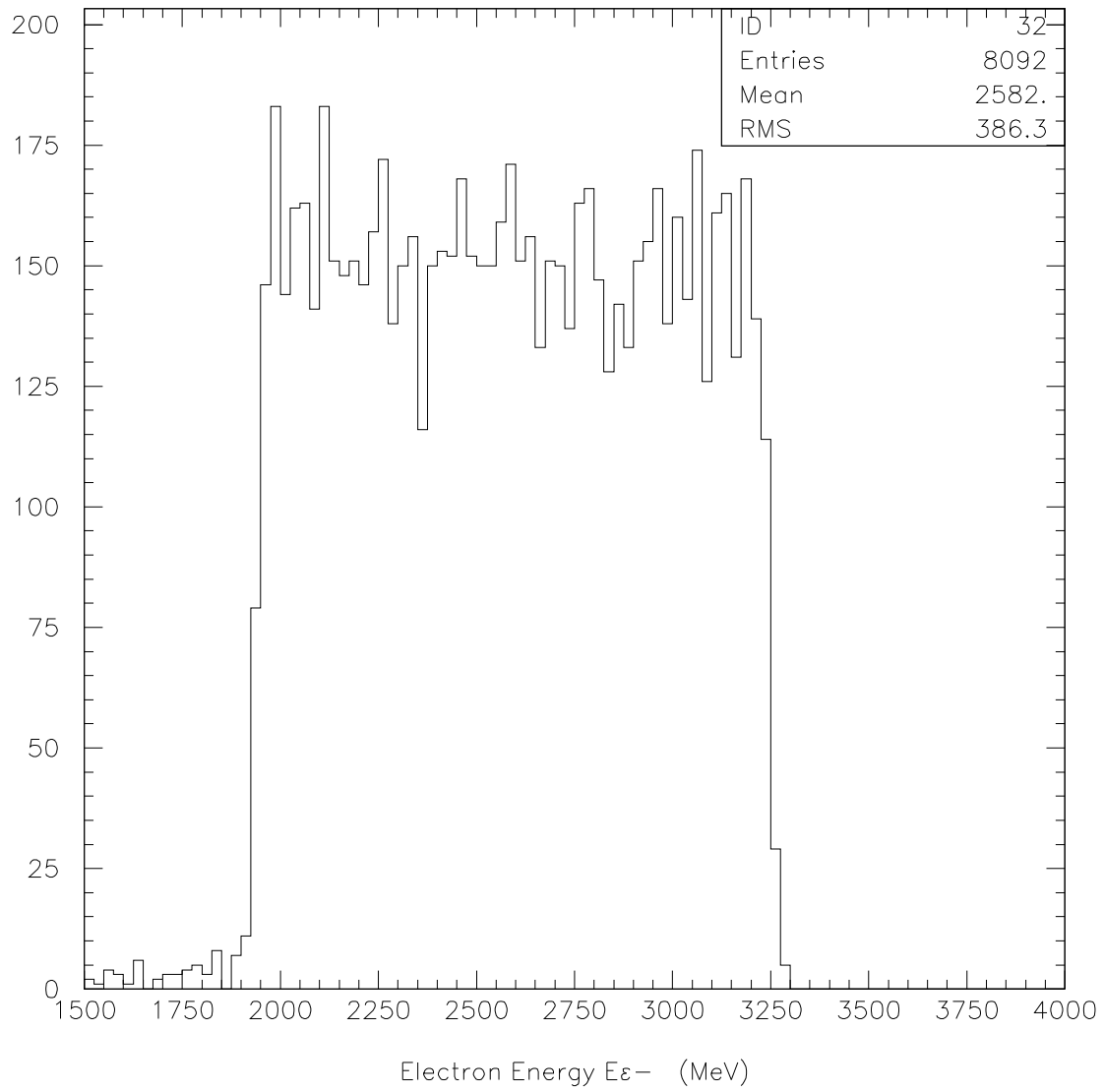


Figure 14: Energy distribution of electrons in eight contiguous plastic scintillator telescopes.

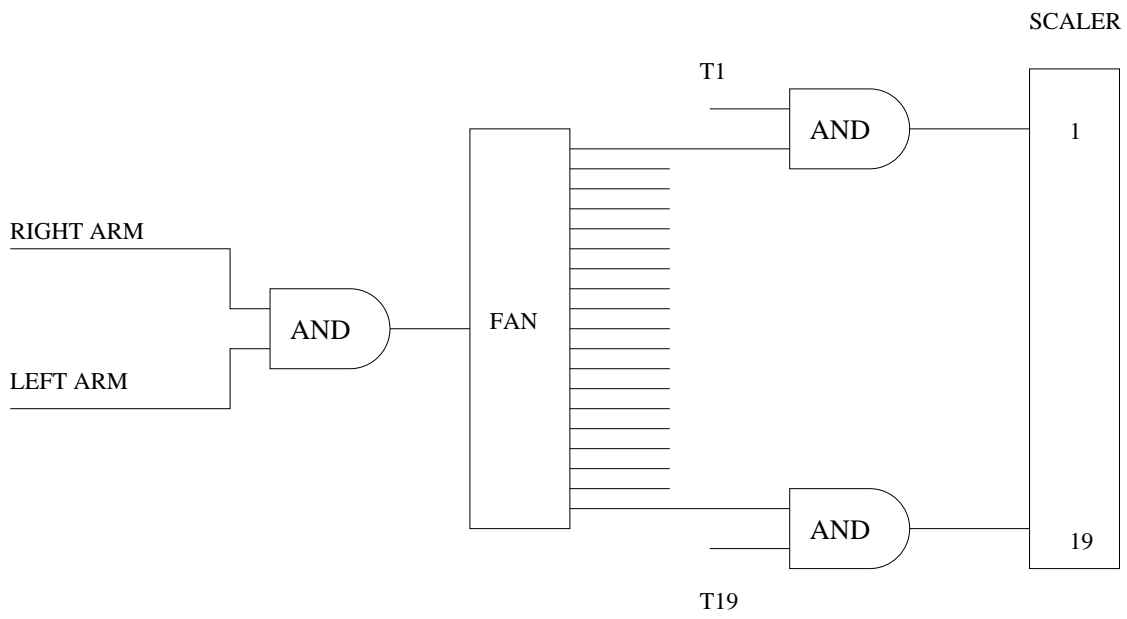
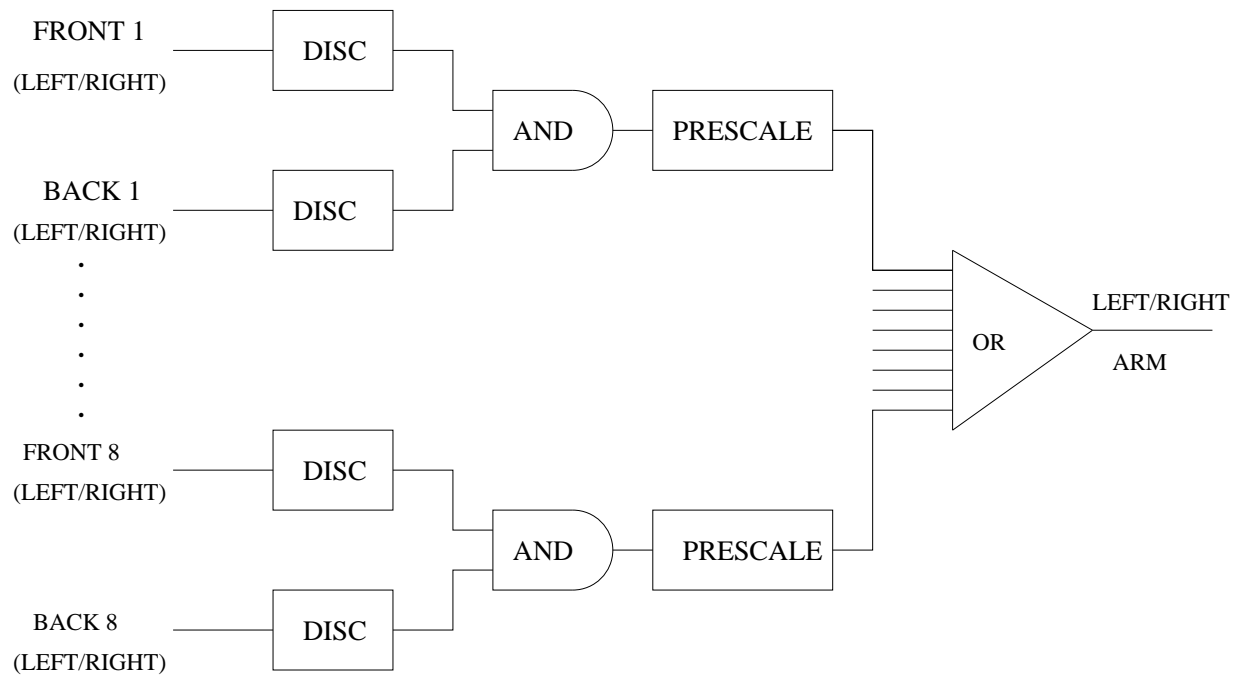


Figure 15: Schematic of the electronics for the proposed pair production luminosity monitor.

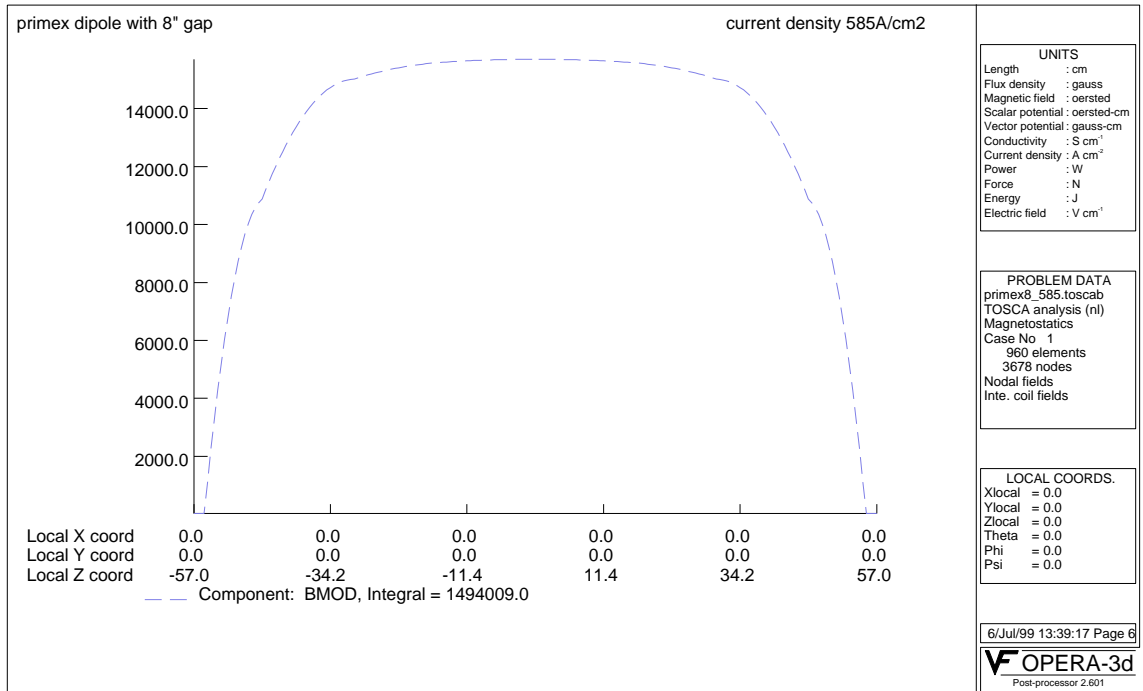


Figure 16: TOSCA calculation of the magnetic field for the BNL 18D36 dipole magnet with an 8.125 inch gap.

Item	Quantity	Unit Price	PrimEx Request	JLab	Collaboration
LeCroy 429 Logic Fan In/Fan Out	4	1085	\$4.34k		
LeCroy 622 Quad 2 Fold Logic Unit	15	1680	\$25.2k		
LeCroy 623 Octal Discriminator	5	2000	\$2.0k	\$8.0	
LeCroy 4434 32 Channel Scaler	3	3990	\$8.0k	\$4.0k	
LeCroy 4614 NIM-ECL Translator	5	1465	\$1.5k		\$5.9k
FermiLab PD-22 Prescaler	7	2000	\$8.0k	\$6.0k	
BC-420 scintillator	36	40			\$1.44k
Philips XP2282B PMT's and bases	36	500	\$10.0k	\$8.0k	
Materials (epoxy, grease, tape)					\$2.0k
detector support structure	1			\$10.0k	
Total			\$59.0k	\$36.0k	\$9.34k

Table 2: Budget for luminosity monitor

Target	Thickness (mil)	ρt (mg/cm ²)	Isotopic purity (%)
¹² C	370	2100	98.9
¹¹⁶ Sn	24	440	95.7
²⁰⁸ Pb	11	330	99.9

Table 3: Thickness and purity of Primakoff targets.

to fabricate the vacuum box and support structure for the pair production luminosity monitor detectors. Detector fabrication facilities for making the plastic scintillator detectors are also available at Kentucky. The dipole magnet will be mapped at Jefferson Lab with manpower from the University of Kentucky and North Carolina A & T State University. Brookhaven National Laboratory has provided a dipole magnet and power supply for this project, priced at \$27.3k and \$55.5k, respectively. These have been shipped to Jefferson Laboratory, with the \$5k shipping costs being borne by Jefferson Lab.

3.4 Energy Calibration

The collaboration is investigating a number of methods to determine the absolute energy calibration of the tagged photons. First, the energy of the electron beam will be determined to an accuracy of 2×10^{-4} using the Hall A arc section. To calibrate the tagger, we plan to employ a technique utilizing the pair production luminosity monitor. The magnetic field of the sweep dipole will be adjusted to the maximum value at which there is some acceptance for e^+e^- coincidences. The sweep dipole field will then be lowered, and the field at which e^+e^- pairs just begin to come in coincidence with a given tagging counter (corresponding to symmetric energy sharing in pair production) will be noted. Under the assumption that the $\int B \cdot dl$ of the pair spectrometer dipole varies linearly with the central field of the dipole as measured by an NMR probe, one can determine the energy of a given tagging counter with respect to the endpoint energy. To this end, the field of the pair spectrometer dipole will be carefully mapped.

Electron Compton scattering can also be used to measure the tagged photon beam energy. Figure 17 shows a GEANT simulation of the distribution of electron-photon opening angles where both particles are detected in the proposed hybrid calorimeter described in section 3.6. The minimum opening angle, as determined from a fit to this distribution which takes into account the two body Compton scattering kinematics and the detector resolutions, gives the tagged photon beam energy. We are presently exploring the sensitivity of this technique in providing an independent, absolute energy calibration.

3.5 Primakoff Targets

The experimental targets are ¹²C, ¹¹⁶Sn, and ²⁰⁸Pb, each with a thickness of 5% radiation length. Details of the targets are given in table 3. These isotopes were chosen because they are even-even nuclei ($J^\pi = 0^+$ ground state), and the ground state charge densities have been determined from model-independent-analyses of electron scattering data. Accurate

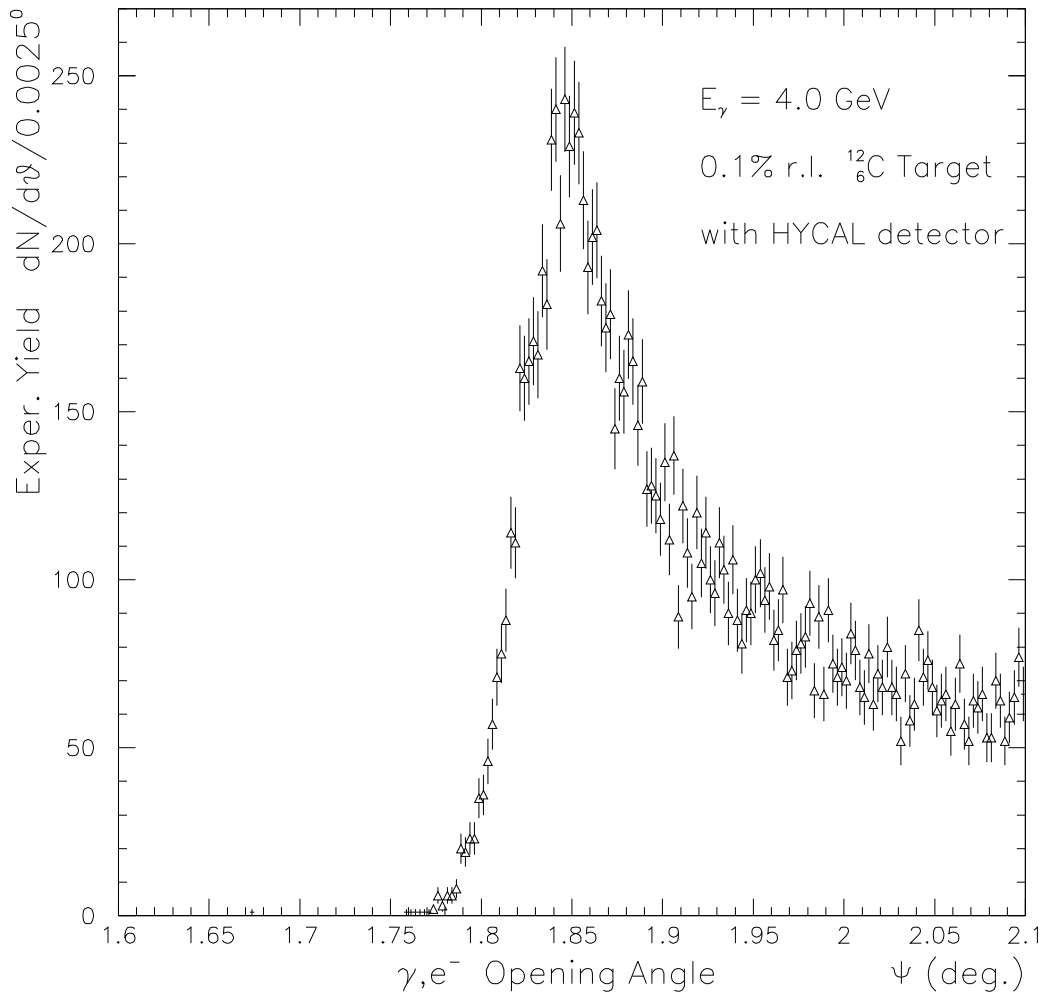


Figure 17: Simulated electron-photon opening angle distribution where both particles are detected in the proposed hybrid calorimeter.

Target	Thickness (mil)	Percentage uncertainty if measured to $\pm 0.05\text{mil}$	Density (g/cm^3)
^{12}C	370	0.014%	1.9-2.3
^{116}Sn	24	0.21%	7.31
^{208}Pb	11	0.46%	11.35

Table 4: Uncertainty in the thickness of Primakoff targets.

Target	ρt (mg/cm^2)	λ @ 14 keV (mg/cm^2)	λ @ 60 keV (mg/cm^2)
^{12}C	2100	1240	-
^{116}Sn	440	-	152
^{208}Pb	330	-	199

Table 5: X-Ray absorption lengths for Primakoff targets.

knowledge of the charge density minimizes the uncertainty in the Primakoff vertex due to the charge form factor.

3.5.1 Measuring the target thickness

We need to have uncertainties in ρt at the level of $\pm 0.7\%$ or better. Oak Ridge estimates the uniformity in thickness of the rolled metal targets is at the level of $\pm 1\%$ to $\pm 2\%$, except near target edges where the thickness drops off. We plan to use oversized targets (2.5 cm by 2.5 cm) and map the target thickness as a function of position on the target. Since the photon beam spot at the target is approximately 2mm in diameter, the targets can be positioned such that the photon beam strikes a region with known, uniform thickness.

X-ray attenuation will be used to measure ρt . In this technique a line source of X-rays is collimated down to a spot size a few mm in diameter and detected in a NaI detector. The experimental targets are placed as absorbers between the source and the detector. By measuring the ratio of X-ray flux in the NaI detector for target-in to target-out, the ratio $\rho t/\lambda$ can be determined where λ is the X-ray absorption length. Since the X-ray absorption lengths are only known to the level of a few percent, the measurement is calibrated by taking X-ray absorption data on a calibration plate of the same material with known thickness.

Best precision is obtained using an X-ray with energy such that the X-ray absorption length λ is approximately $\rho t/2$. For the C target this energy is approximately 60 keV. Therefore, a good choice for the C target is the 14 keV line from ^{57}Co , and for the Sn and Pb targets the 60 keV X-ray line from ^{241}Am .

The calibration plates should be thick enough to limit thickness uncertainties from micrometer accuracy, robust enough to be handled with a micrometer, and with thickness variation less than 2μ . Therefore, we plan to use calibration plates of natural isotopic abundance materials that are approximately twice the thickness of the experimental targets, 50 mil for Sn and 20 mil for Pb.

Let R_0 , R_T and R_C equal the ^{241}Am 60 keV X-ray rates in the NaI without absorber, with the target absorber, and with the calibration plate absorber, respectively. The target

thickness T is given by

$$T = C \frac{\ln(R_0/R_T)}{\ln(R_0/R_C)} \quad (11)$$

where C is the calibration plate thickness in units of g/cm^2 . The error in the target thickness measurement is given by

$$\left(\frac{\sigma_T}{T}\right)^2 = \left(\frac{\sigma_C}{C}\right)^2 + \left[\frac{1}{\ln(R_0/R_T)}\right]^2 \left(\frac{\sigma_{R_T}}{R_T}\right)^2 + \left[\frac{1}{\ln(R_0/R_C)}\right]^2 \left(\frac{\sigma_{R_C}}{R_C}\right)^2 + \left[\frac{1}{\ln(R_0/R_T)} - \frac{1}{\ln(R_0/R_C)}\right]^2 \left(\frac{\sigma_{R_0}}{R_0}\right)^2 \quad (12)$$

Evaluating the above expression for 60 keV X-rays on Sn, and assuming a measurement tolerance of ± 0.05 mil gives

$$\frac{\sigma_T}{T}|_{Sn} = \sqrt{10^{-6} + \frac{0.119}{N_T} + \frac{0.0298}{N_C} + \frac{0.0298}{N_0}} \quad (13)$$

where N_T , N_C and N_0 are the total counts for target absorber, calibration absorber, and no absorber. The same assumptions for the Pb target gives

$$\frac{\sigma_T}{T}|_{Pb} = \sqrt{6.25 \times 10^{-6} + \frac{0.364}{N_T} + \frac{0.0909}{N_C} + \frac{0.0909}{N_0}} \quad (14)$$

Assuming that errors from N_C and N_0 are negligible, then approximately 2,500 counts are required for Sn and 8,500 counts for Pb to measure ρt at the level of 0.7%. For a source intensity of $R_0 = 1$ Hz, the required count time is 12.5 hours for both Sn and Pb.

A somewhat different measurement strategy must be used for the ^{12}C target because of possible variations in graphite density. In brief, the concept is to accurately measure the thickness $t(x,y)$ and average density ρ_0 of the target using a micrometer and mass scale. X-ray attenuation with a ^{57}Co source would then be used to measure departures from the mean value of $\rho_0 t(x,y)$. We would expect to test the graphite in this manner and choose target material with small variation in density.

3.5.2 Estimated Budget

The University of Massachusetts is responsible for the targets and the target measurements. the X-ray scanning device with ^{241}Am source will be constructed by the UMass group with grant funds and departmental resources. Table 6 shows the target and additional source costs.

3.6 The Hybrid Calorimeter (HYCAL)

The two photons from the π^0 decay will be detected in the highly segmented array of Hybrid Shower Calorimeter (HYCAL). It will be about $119.0 \times 119.0 \text{ cm}^2$ in the dimension transverse

Item	PrimEx request
^{12}Sn target	\$7.8k (Lease option)
^{208}Pb target	\$6.5k (Purchase)
$100\mu\text{Ci}^{57}\text{Co}$ source	\$1.1k
Precision micrometer	\$0.4k
Total	\$15.8k

Table 6: Budget for Primakoff targets

to the beam and will be located at 7.5 meters downstream of the π^0 production target. The calorimeter is designed to measure both the position and the energy of electromagnetic showers using a two dimensional matrix of radiators (lead glass and crystals). That will be accomplished by choosing the cross section of the individual counters small enough so that the energy leakage into adjacent counters can be used to determine the position of the shower axis. The calorimeter will consist of two types of detectors. The outer part of the calorimeter will be made from a 28×28 matrix of 663 modules of lead glass Cherenkov detectors with the size of the radiators $4.25 \times 4.25 \times 34 \text{ cm}^3$. For enhanced position and energy resolution to measure the mass and angle of the π^0 , the central region of the HYCAL will be constructed from 480 modules of lead tungstate (PbWO_4) crystals of size $2.125 \times 2.125 \times 21.2 \text{ cm}^3$. These high resolution detectors will cover a $46.75 \times 46.75 \text{ cm}^2$ region around the beam where at least one photon from the $\pi^0 \rightarrow \gamma\gamma$ decay will hit the calorimeter. In addition, this crystal insertion will significantly improve the radiation hardness of the detector near the beam line where radiation doses can be high. The central $4.25 \times 4.25 \text{ cm}^2$ hole will be left open to enable the photon beam to pass through. The modules contiguous with this region on the beam axis as well as the two outermost layers of modules in the lead glass wall will be excluded from the fiducial volume of the detector to control coordinate resolution and detection efficiency near the boundaries of the detector. The total number of counters of the detector is 1143. To monitor and correct possible gain changes due to temperature and aging, a light monitoring system will be used which is described separately in the section 3.8. During data taking, the calorimeter will be calibrated with electrons and tagged photon beams to determine the gains for the counters. For this purpose the calorimeter will be installed on a transporter allowing to expose every counter of the detector to the beam. Additional calibration will be done with photons from π^0 decays using the known value of the π^0 mass.

3.6.1 Lead Glass Detectors

We will use Cherenkov counters composed of TF-1 type lead glass radiator of dimensions $4.25 \times 4.25 \times 34 \text{ cm}^3$ (see figure 19). Their physical properties are listed in the table 7. The lead glass block dimensions are optimized to measure photon energies in the region from a few hundred MeV to a few GeV where light collection and photon statistics are defining the energy resolution, and energy leakage is relatively unimportant. Also, the lead glass radiators provide a good compromise between the requirements for precision of position and energy measurements and the complexity and price of the entire calorimeter. Cherenkov light

<i>PbO</i> content (wt perc)	50.8
density (g/cm^3)	3.85
Radiation length	2.7
Critical energy (MeV)	17.5
Refractive index	1.65
Nucl. collis. length (cm)	21.8
Coefficient of thermal expansion ($\times 10^{-7}$ cm/cm/C)	88

Table 7: Physical properties of the Russian made TF1 lead glass modules.

produced in the lead glass radiator(1) from the electromagnetic shower will be detected by a photomultiplier tube (PMT)(5) of the FEU-84 type made in Russia. The individual blocks will be wrapped in aluminized mylar foil (2) ($25 \mu m$) as a light reflector and thick ($50 \mu m$) black paper (3) for optical isolation between the blocks. Electromagnetic calorimeters based on this type of lead glass and PMT's are widely used in many high and medium energy experiments[31][45]. The excellent optical transparency and optimized transverse size of the lead glass radiator provide good energy and position resolutions:

$$\frac{\sigma_E}{E}(\%) = \frac{4.}{\sqrt{E}} + 2.5, \sigma_x = \frac{5mm}{\sqrt{E}}, \quad (15)$$

where E is in GeV.

The ITEP group providing this lead glass system has a lot of experience in building and running these devices for experiments at ITEP (Moscow), IHEP (Serpuukhov), and Fermilab (Batavia).

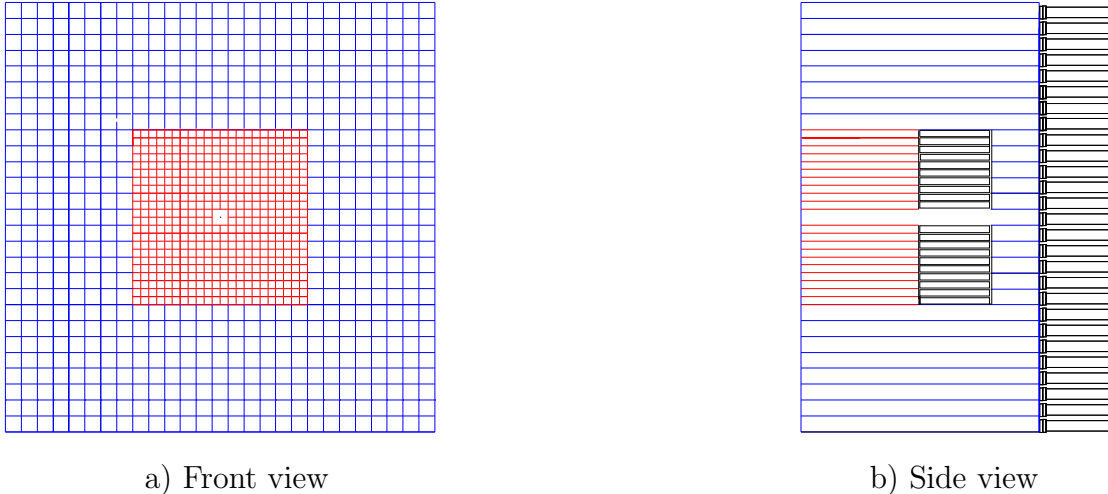


Figure 18: The schematic structure of the HYCAL calorimeter.

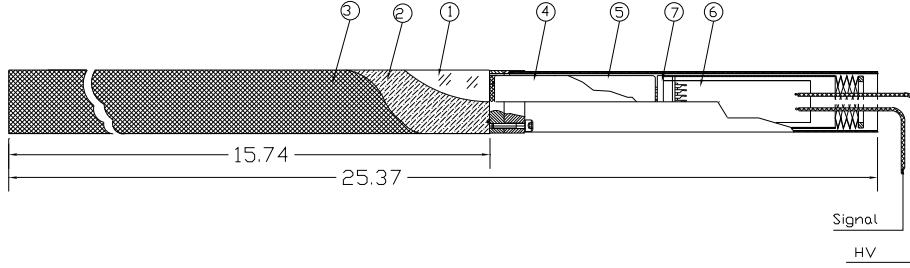


Figure 19: Single module of the HYCAL lead glass detector.

3.6.2 Lead Tungstate Detectors

At these energies, the Primakoff cross section peaks at extremely small angles: $\theta = 0.02^\circ$ at $E_\gamma = 5\text{GeV}$. In order to identify and extract the Primakoff amplitude, the experimental setup must have sufficient resolution for the pion production angle. This resolution depends strongly on the decay photon energy and position accuracy of the calorimeter (see section 3.6.5). The high resolution insertion to the HYCAL detector will improve the pion angular resolution by 50% (see Figure 23). We plan to use 480 modules of finely granulated lead tungstate ($PbWO_4$) scintillating crystals in the central part of the calorimeter. Their properties are shown in table 6. The transverse size of the crystals will be $2.125 \times 2.125 \text{cm}^2$, and the length will be selected between 16-20 cm (18-22 X_o) after performing beam tests of the prototype detectors. Each crystal will be wrapped in thin aluminum foil and viewed with a Phillips XP1911 PMT coupled to the crystal with optical compound. The light yield of the crystal is highly temperature dependent ($\sim 2\%/^\circ C$). Therefore, the temperature of the calorimeter has to be well stabilized ($\pm 0.1^\circ C$). For that purpose all four sides of the calorimeter will be surrounded by water cooled copper plates and thermal isolation. The temperature will be continuously monitored by sensors coupled to the front of the crystals.

The Mainz group recently reported excellent energy resolution with similar crystals operated at a stabilized temperature of $8^\circ C$. They found

$$\frac{\sigma_E}{E}(\%) = \frac{1.54}{\sqrt{E}} + 0.3, \quad (16)$$

where E is given in GeV[46].

3.6.3 The Calorimeter Frame

All individual modules will be assembled in a rectangular box inside of the calorimeter frame (see figure 20). The frame has to be movable in both horizontal and vertical directions in order to provide energy calibration of each channel. A transporter will be designed and

Radiation length (cm)	0.89
density (g/cm^3)	8.28
Moliere radius (cm)	2.0
Peak wavelength (nm)	450-500
Index of refraction	2.2
Temp. dep. of light yield (%/°C)	-1.9

Table 8: Physical properties of the lead tungstate crystals.

built to provide movement of the entire array of detectors, its support frame, the thermo-stabilization system, the delay cables and electronics. During calorimeter calibration each block will be positioned in the beam of photons (or electrons) of known energy within an accuracy of $\pm 0.3mm$. The transporter system will also provide positioning of the entire calorimeter in the maintenance and storage location a few meters away from the beam center. As indicated in figure 20, the bottom portion of the transporter will be constructed in two parts. When not in use, the HYCAL will be moved to the side out of the beam, and the half of the transporter support which lies under the beam pipe will be removed to minimize interference with other operations in Hall B.

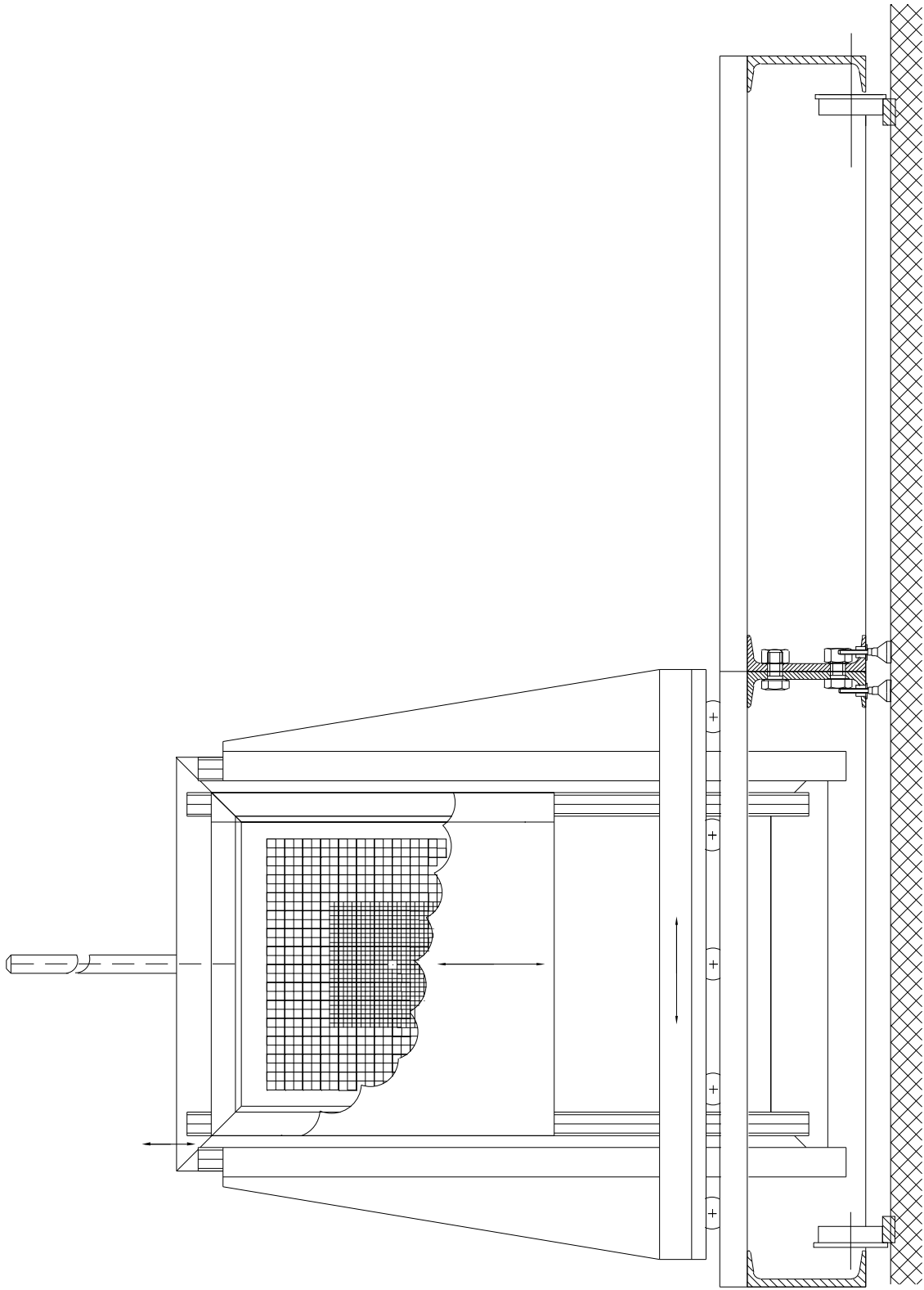


Figure 20: Schematic view of the HYCAL electromagnetic calorimeter with the transporter.

3.6.4 Estimated Budget

The Hampton University is responsible for the design development and construction of the π^0 hybrid calorimeter (HYCAL). A breakdown of estimated budget for this project is shown in the table below. Miscellaneous items include glue, wrapping materials, tape, *etc.*

Description	number	unit price	PrimEx Request	JLab	Collaboration
PbWO ₄ crystals	590	\$400	\$236.0k		
Prototype PbWO ₄ detector					\$40.0k (HU)
PMT's	510	\$200	\$102.0k		
High voltage divider	510	\$70	\$35.7k		
Temperature control system	1	\$9550	\$9.55k		
mu-metal shields	510	\$25	\$12.75k		
Lead glass modules and PMT's	900 900			\$180.0k (MOU)	\$550.0k (ITEP Moscow)
Frame (engineering, construction, remote control)	1	\$100.0k		\$100.0k	
Misc.		\$20.0k	\$20.0k		
total			\$416.0k	\$280.0k	\$590.0k

3.6.5 Resolutions

Particle identification of the two photon events will be accomplished by calculating the invariant mass of coincident photon pairs from the experimentally measured quantities E_{γ_1} , E_{γ_2} , and $\psi_{\gamma_1\gamma_2}$, the opening angle between the two photons. The square of the invariant mass is given by:

$$m_{\gamma\gamma}^2 = 2E_{\gamma_1}E_{\gamma_2}(1 - \cos\psi_{\gamma_1\gamma_2}). \quad (17)$$

Good invariant mass resolution is needed to minimize uncertainties associated with background subtractions. Figure 21 shows the expected invariant mass resolution of our setup for coherent pion production on lead for $E_\gamma = 5.7 \text{ GeV} \pm 0.3\%$ and $\theta_{\pi^0} = 0.1^\circ$, where it can be seen that we expect an experimental resolution of about 3.5 MeV. A number of techniques for determining the pion energy with the proposed hybrid detector have been examined[42]. The first and crudest method involves simply summing the experimentally measured energies of the two photons. The results of this method are shown in figure 22(a). For the online data analysis, this method will be implemented in the first energy cut on the raw data.

A second method involves the use of the energy sharing between the two photons and

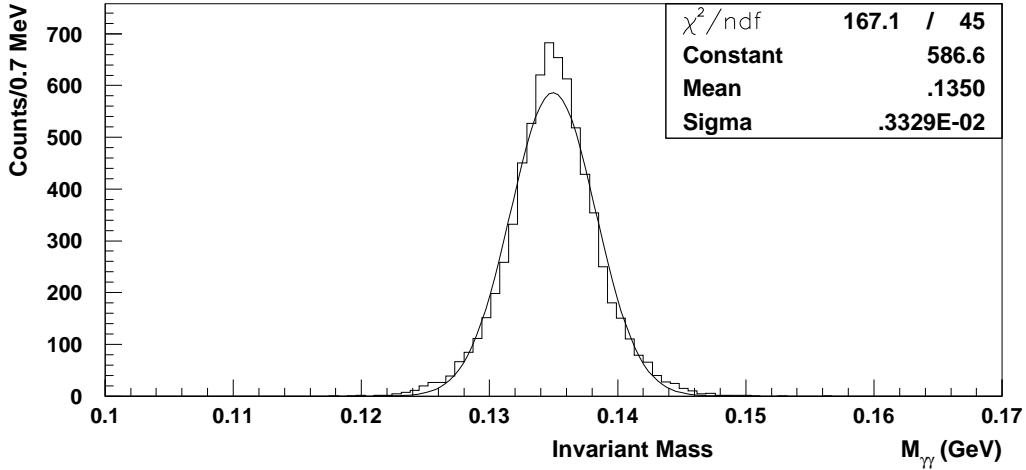


Figure 21: The $M_{\gamma\gamma}$ invariant mass distribution.

the opening angle provided by the experimentally measured coordinate information:

$$E_{\pi^0} = \sqrt{\frac{2m_{\pi^0}^2}{(1-X^2)(1-\cos\psi_{\gamma_1\gamma_2})}}, \quad (18)$$

where

$$X = (E_{\gamma_1} - E_{\gamma_2}) / (E_{\gamma_1} + E_{\gamma_2}). \quad (19)$$

The results of this method for our detector with the high resolution insertion are shown in figure 22(b), where it can be seen that only marginal improvement is obtained. In general, this method is best suited for photon detectors of poor energy resolution and good angular resolution.

The energy can also be reconstructed using the measured energy of one of the photons and the opening angle:

$$E_{\pi^0} = E_{\gamma_i} + \frac{m_{\pi^0}^2}{2E_{\gamma_i}(1-\cos\phi_{\gamma_1\gamma_2})}. \quad (20)$$

The results of this third method are shown in figure 22(c). As is seen from the figure, the resolution is considerably improved. This is a result of the fact that in most cases the higher energy photon is registered in the high resolution insertion of the detector where coordinate and energy resolution are each a factor of two better than in lead glass. By comparison, if one were to measure the pion energy by the same method but without the high resolution insertion, one obtains a significantly degraded resolution as evidenced in figure 22(d).

Resolution in θ_{π^0} is of particular importance in the identification of the forward peaked π^0 's photoproduced by the Primakoff mechanism ($\theta_{\pi^0} \sim 0.02^\circ$) from pions produced at larger

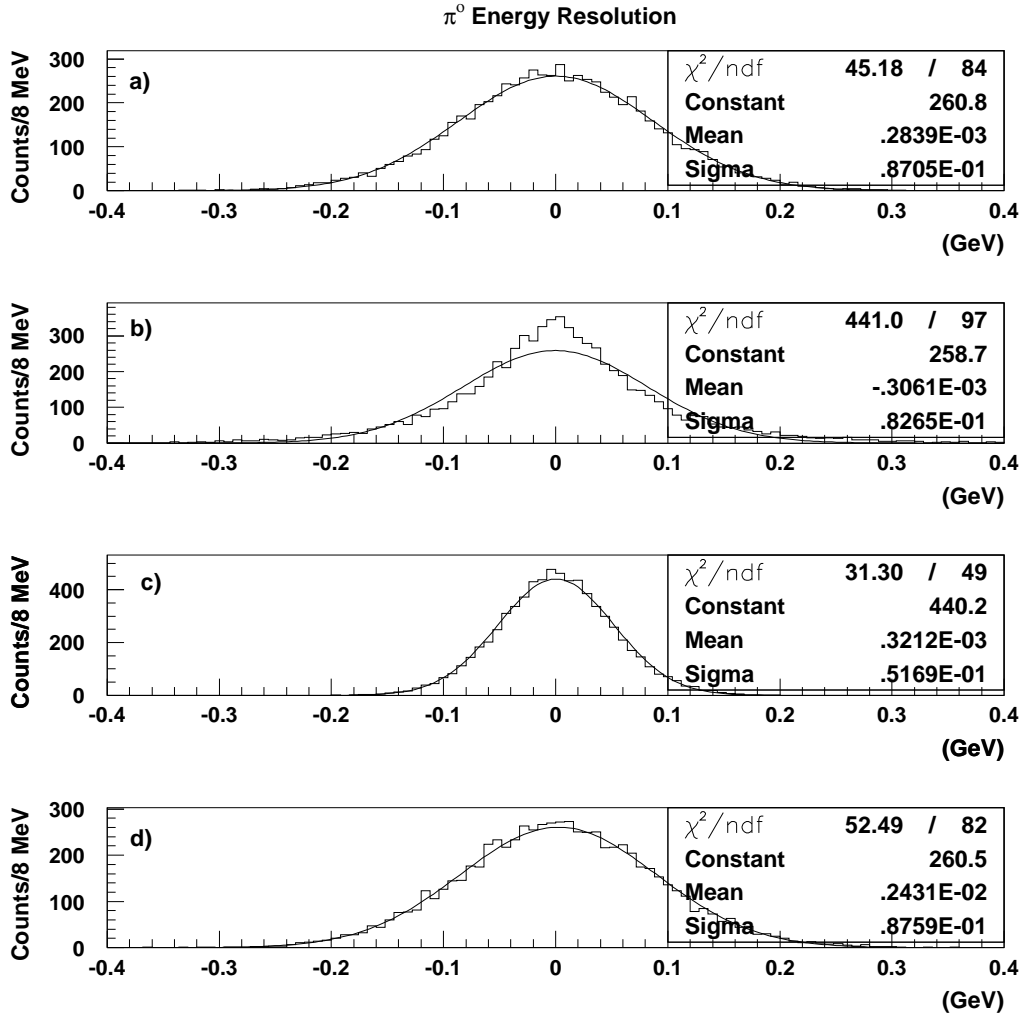


Figure 22: π^0 energy resolution for different methods of determining the pion energy. Distribution of events vs. $(E_{\pi^0}^{sampled} - E_{\pi^0}^{reconstructed})$ for a) sum of energies; b) energy sharing technique; c) using energy and opening angle; d) same as method (c), but without the high resolution detector insertion.

angles via the nuclear field (see figures 3 and 4). The pion angle can be determined from the measured photon energies and angles by:

$$\cos\theta_{\pi^0} = \frac{E_{\gamma 1}\cos\theta_{\gamma 1} + E_{\gamma 2}\cos\theta_{\gamma 2}}{\sqrt{E_{\gamma 1}^2 + E_{\gamma 2}^2 + 2E_{\gamma 1}E_{\gamma 2}\cos\psi_{\gamma 1\gamma 2}}}. \quad (21)$$

Figure 23(a) shows the expected angular resolution for coherently produced pions for $E_{\gamma} = 5.7\text{GeV} \pm 0.3\%$ and $\theta_{\pi^0} = 0.1^\circ$ for a detector consisting of lead glass blocks only. Figure 23(b) shows the improved resolution by implementing the high resolution detector insertion.

The angular resolution under the Primakoff peak can be further improved by means of a kinematical fit, the results of which are shown in figure 23(c). If the incident photon energy is known, and the residual nucleus is left in its ground state as is the case with coherently photoproduced pions, a correlation between the opening angle and the two photon energies results. This correlation is shown in figure 24(a), and the projection onto the $\psi_{\gamma\gamma}$ axis, figure 24(b), gives the opening angle distribution. This additional kinematical constraint results in the improved angular resolution shown in figure 24(c).

The design of the proposed π^0 detector has been motivated by the fact that the best angular resolution is obtained with the kinematical fit. This technique requires good knowledge of the high energy photon. We have investigated the angular resolution of alternate detector designs using a calorimeter plus a wire chamber to obtain improved position resolution in conjunction with a preshower counter a few radiation lengths thick to convert the photons[43]. Because of the necessity of the preshower counter, the energy resolution of the photons and the resulting angular resolution of the pions in such a detector is significantly degraded in comparison to the hybrid lead glass/PbWO₄ detector. As such, we conclude that the calorimeter alone is preferable. (It is worth mentioning, however, that a detector composed entirely of PbWO₄ blocks would be the best option yet, though more costly.)

A further consideration in θ_{π^0} resolution involves the accuracy with which the interaction vertex is known. Figure 25(a) shows the calculated angular resolution for a pointlike photon beam spot size on the target. Figures 25 (b) and 25(c) show, respectively, the progressive degradation in resolution for four and ten millimeter spot sizes. Such considerations argue for a placement of the target as close to the bremsstrahlung converter as is practical, while still providing space for sweeping magnets. We propose placing the π^0 production target 6.5 meters downstream of the converter. In order to get good acceptance for pions, this requires that the π^0 detector be placed upstream of the CLAS, 14 meters from the bremsstrahlung converter.

3.7 The Charged Particle Veto

The veto counter is an array of scintillator paddles that sits in front of the calorimeter. The purpose of the detector is to veto charged particles that are produced by charged particles hitting the vacuum box in the sweeping dipole. We propose to build an array of ten scintillators with PMT readout on both ends to cover the calorimeter. To minimize photon conversion in the veto counter, only a single layer of scintillator material 5 mm thick

π^0 Angular Resolution

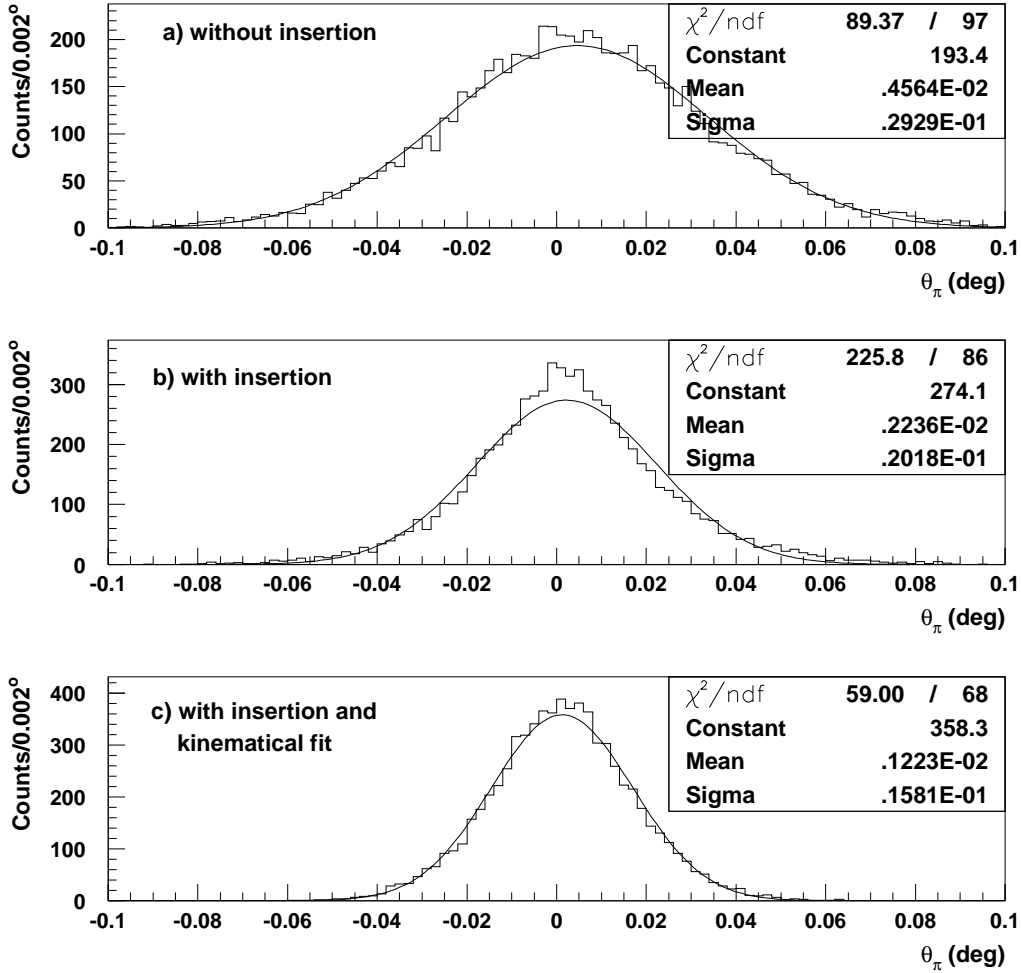


Figure 23: π^0 angular resolution. Distribution of events vs. $(\theta_{\pi^0}^{sampled} - \theta_{\pi^0}^{reconstructed})$ a) without high resolution insertion; b) with high resolution detector insertion; c) with high resolution detector insertion and kinematical fit.

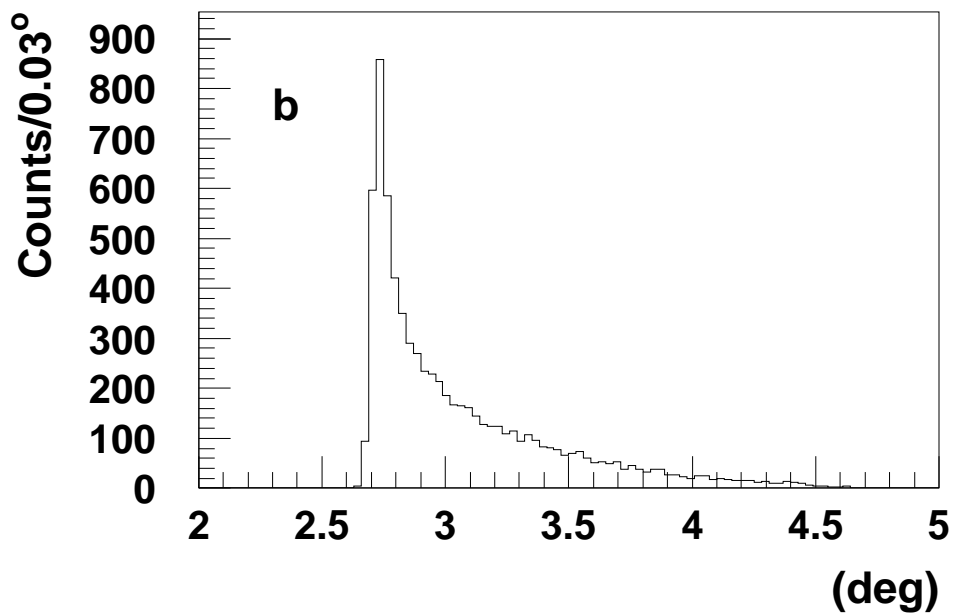
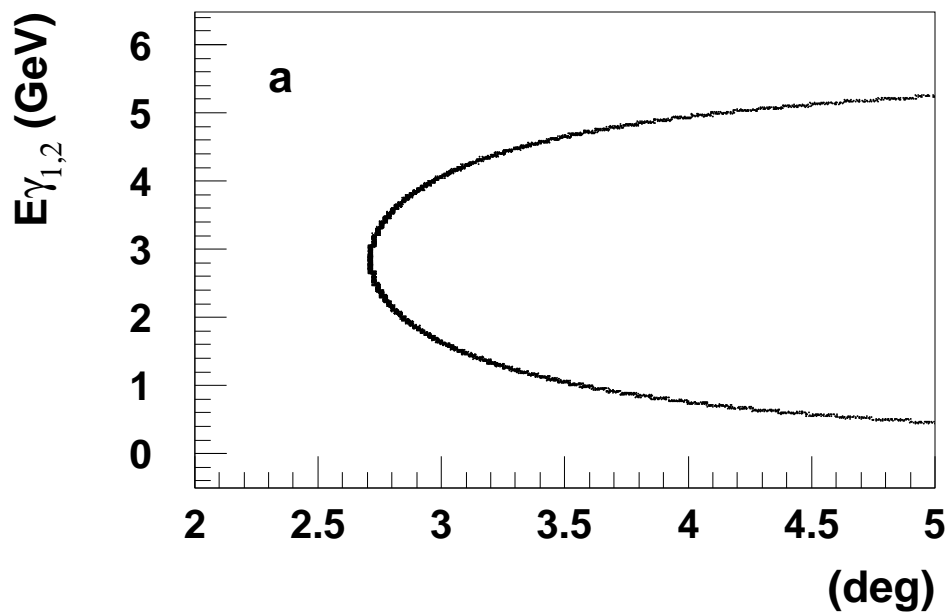


Figure 24: a) Correlation between photon opening angle and two photon energies; b) Opening angle distribution.

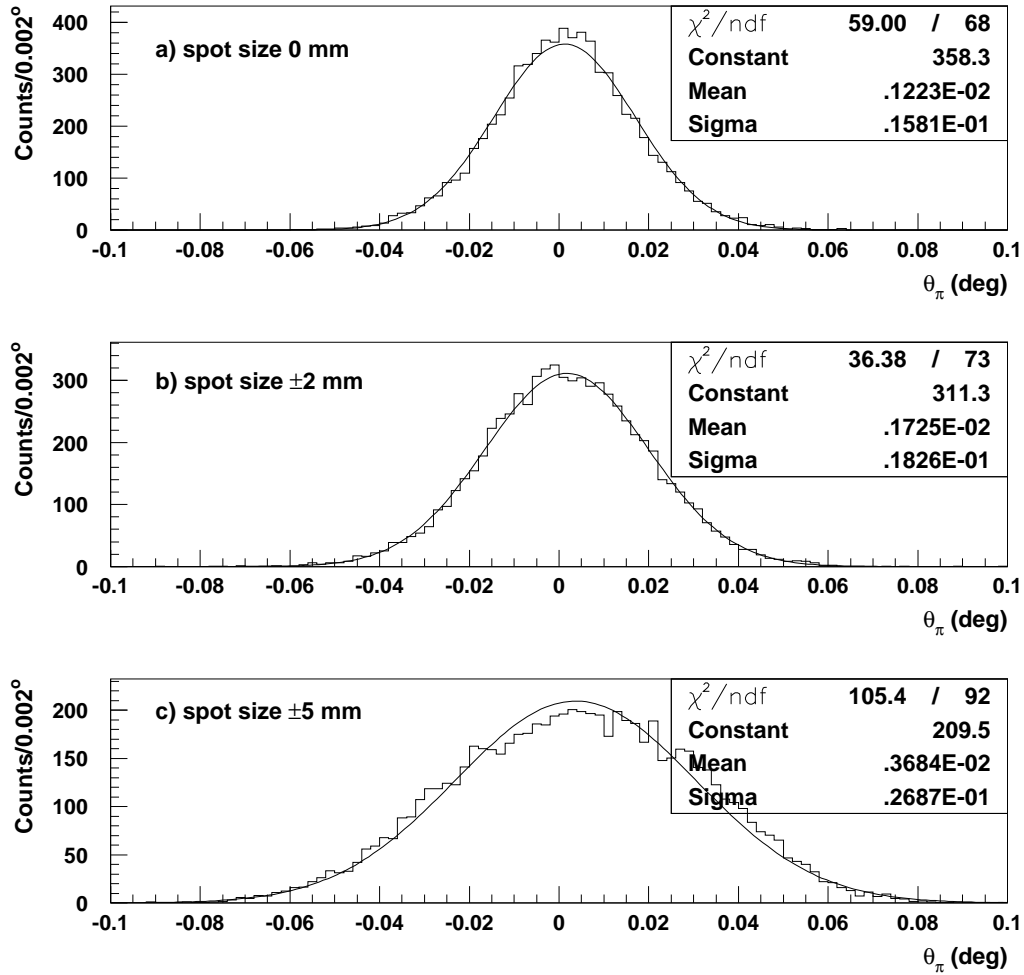


Figure 25: π^0 angular resolution for different photon beam spot sizes on the target. Distribution of events vs. $(\theta_{\pi^0}^{\text{sampled}} - \theta_{\pi^0}^{\text{reconstructed}})$ for a) point spot; b) ± 2 mm spot size; c) ± 5 mm spot size.

Item	Unit Price	PrimEx Request
Bicron BC-408 scintillator		\$4.0k
Bicron BC-800 UVT light guide material		\$0.5k
Twenty 1-1/2" PMT's and bases	\$446	\$9.8k
Hamamatsu R580-15 or equivalent		
Materials (epoxy, grease, tape, mylar		\$2.5k
Two LRS612A PMT linear amplifiers	\$1910	\$3.8k
Three LRS623B octal discriminators	\$1750	\$5.3k
Total		\$25.9k

Table 9: Budget for the charged particle veto detector.

(1.2% radiation length) is used. Timing information from the two ends of the scintillator is used to obtain the longitudinal position of the hit in the counter.

The diagram (see figure 26) shows the proposed layout and size of the scintillators. The dimensions are in centimeters. The circular two cm radius notch on the two central scintillators is to allow the photon beam to pass through the counter.

For the scintillator material, we use 5 mm thick Bicron BC-408. This material has a long attenuation length, 210 cm, making it ideal for long, thin scintillators with readout on both ends. It also has a short rise time, 0.9 ns. For the light guides we use Bicron UVT acrylic BC-800, and cut and bend our own adiabatic light guides from 1/4" thick stock. For phototubes and bases we use the 1-1/2" Hamamatsu R580-15, or equivalent, PMT. This tube has a gain of approximately 1×10^6 and a rise time of 2.7 ns.

3.7.1 Estimated Budget

The proposed budget for the veto counter can be seen in table 9. Because of photon conversion in the veto counter, it cannot be used as a hardware veto at the trigger level of the experiment. Rather, timing and pulse height information from the veto counter are recorded for each trigger, and then off-line analysis determines if extraneous hits in the calorimeter are caused by charged particle backgrounds. In the proposed budget we have included money for a linear preamp (the LRS612A), which is needed to amplify small signals from minimum ionizing particles passing through 5 mm of scintillator as far as 1 meter from a PMT of modest gain. The preamp also provides fanout capability. We have not budgeted for the 20 channels of TDC and ADC in the cost estimate. The University of Massachusetts will provide manpower for machining and shaping the lightguide material, and for assembly of the detectors.

3.8 Gain Monitoring System

The main purposes of the gain monitoring system are 1), on-line and off-line control of the stability of all photomultipliers in the experiment, including the shower calorimeter, veto counters, and luminosity monitors and 2), time control of the absolute gain (ADC

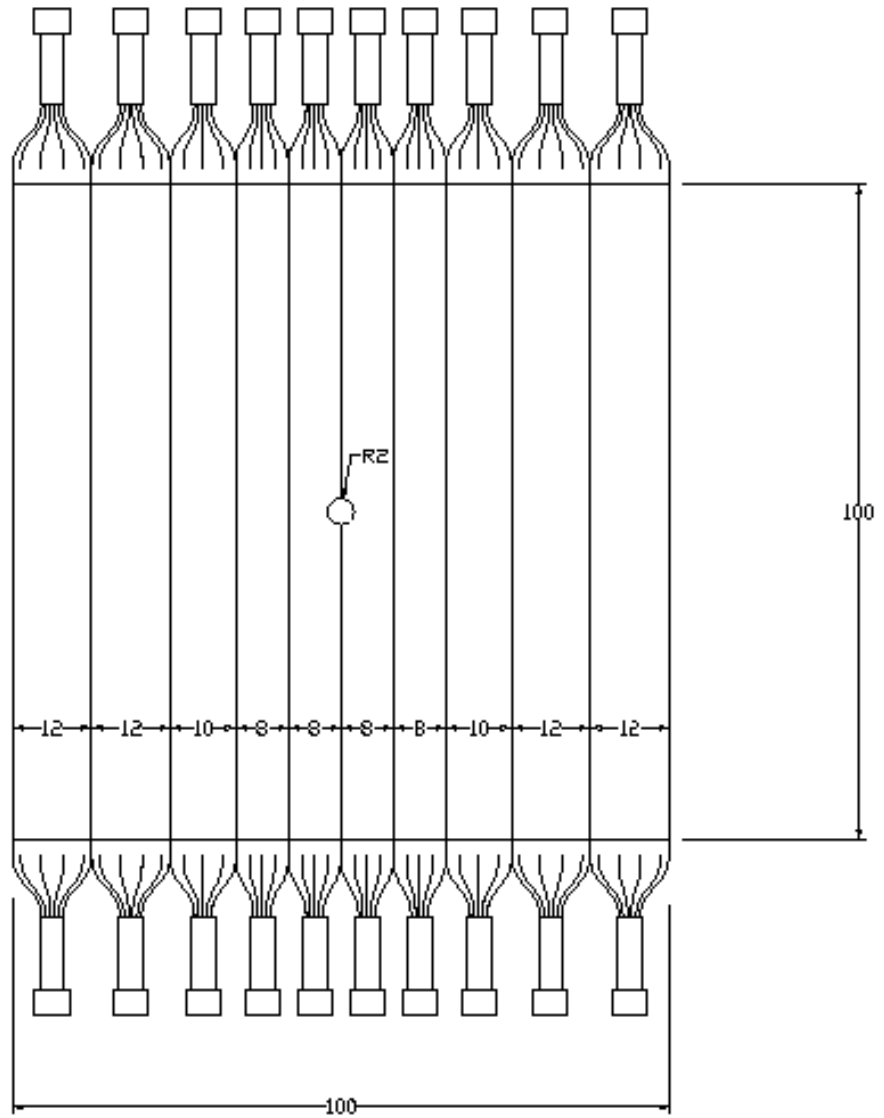


Figure 26: Layout of the veto scintillator array.

channel/MeV) of each module of the calorimeter.

The system will be based on a pulsed nitrogen laser which provides short pulses (600 ps wide) in the UV range (337 nm). The repetition rate will be 50 Hz or less and the instantaneous power will be 100 μ J per burst. There will be a set of filters for intensity variation, a wavelength shifter from 337 nm to \sim 425 nm which corresponds to the spectral range of sensitivity of the PMTs, a light mixer, and a set of \sim 1200 optical fibers which will deliver light to the individual PMTs (see figure 27).

The light pulses emitted by the nitrogen laser will pass through the filter system. In a semi-transparent mirror, part of the light will be reflected to the face of PIN photodiodes. The good linearity and gain stability of the diodes will provide light monitoring of the laser. The optics in the path of the laser light will be used to expand and collimate the light to about 1 mm in diameter. The expanded light will illuminate one end of a \sim 10 m length and 1 mm diameter cable which delivers the laser light to the light distribution system. The light distribution system will be mounted on the frame of the shower calorimeter.

The distribution system consists of a wavelength shifter (a container with liquid scintillator or a piece of plastic scintillator), a light mixer (a rectangular piece of Lucite or an empty chamber with walls covered from the inside with high quality diffuser) and \sim 1200 optic fibers which will deliver light from the mixer to the individual modules. Some of fibers will deliver the light to reference PMTs equipped with radioactive sources for stability control after the distribution system.

The fiber which transmits the light from the laser optics to the light distributor will have a silica core of diameter 1 mm and cladding transparent to UV light. All other fibers after the mixer (200 μ m in diameter) will be made of plastic polymer. The fibers will be connected to the open end of the lead glass modules with ST couplers.

3.8.1 Laser performance requirements

The amount of light equivalent to \sim 1 GeV energy deposited in one module of lead glass equals \sim 10³ photons/module in the spectral range of sensitivity of the PMT. Taking into account the efficiency of the photocathode, the total amount of light for all modules which must be distributed in the final stage is \sim (10⁶ – 10⁷) photons.

The gain correction factor, calculated on the basis of laser calibration data from each of the modules and reference PMTs, is as follows:

$$g_i(t) = \frac{Q_i^L \times Q_{RC}^\alpha}{Q_{RC}^L}, \quad (22)$$

where Q_i^L is the average pulse height of the i-th module from the laser light, Q_{RC}^L is the average pulse height of the reference PMT from the laser light, and Q_{RC}^α is the average pulse height of the reference PMT from the ²⁴¹Am source+scintillator light. In order to correct for gain fluctuations during the run period, one needs to multiply the calibration factors by the ratio $g_i(t)/g_i(t_o)$, where $g_i(t_o)$ is the correction factor obtained at the time of calibration and $g_i(t)$ at the current time. Transmission losses at different stages of the gain monitoring system are given in table 10. As can be seen from the table, the number of

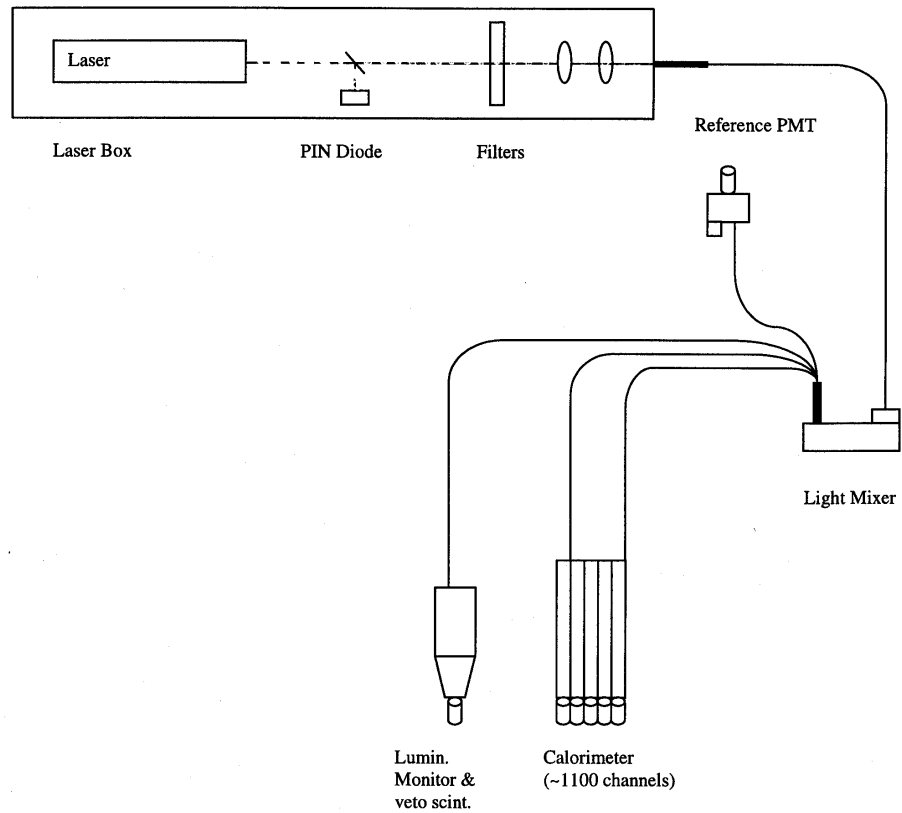


Figure 27: Schematic view of laser based gain monitoring system.

Item	Transmission:	
	Typical	Use
PIN photodiode	50%	0.5
Beam formation optics	$(90\%)^2$	0.81
10 m fiber entrance	1 dB x 50%	0.44
Attenuation in 10 m fiber	0.08 dB/m	0.91
Fiber-scintillator jump	2 dB	0.79
Scintillator loss	1 dB x 50%	0.45
Mixer entrance	1 dB	0.89
Mixer-fiber jump	2 dB x $1.e-6$	0.8×10^{-6}
Attenuation in 2 m fiber	0.08 dB/m	0.99
Fiber exit at detector	1 dB	0.89
Total Transmission		3.6×10^{-8}
Photons from laser Ln203C		1.7×10^{14}
Photons into a module		6.1×10^6

Table 10: Photon transmission for the gain monitoring system.

photons must be reduced using optical filters. In order to ensure uniformity in the amount of light reaching each individual PMT, all fiber-optic channels must be carefully prepared and visually inspected, and the response signals from the PMTs must be equalized.

In order to eliminate long-term variations due to temperature or voltage drifts and aging effects, a stability feedback system based on an electro-optical converter/stabilizer will be incorporated into the laser system. In the existing gain monitoring system of the COMPASS experiment at CERN, the authors claim 0.2 - 0.3% pulse stability[31] using a similar feedback system. The system is based on an electro-optical crystal (DKDP) sitting between two polarizers. Part of the laser light is directed to the very stable PIN diode + amplifier system, the signal of which is compared to the reference level. In case of discrepancy, the HV applied to the DKDP crystal (which defines its optical transparency) is modified. The system is completely independent of the laser itself and is capable of correcting the slow amplitude variations to about the 0.1% level. Fast pulse-to-pulse jumps remain unchanged.

3.8.2 Comparison of light sources

A laser source with a wavelength shifter provides short pulses of blue light. The number of photons into each lead glass module is $\sim 6.1 \times 10^6$ per pulse and must be attenuated. A major concern is pulse to pulse as well as long term instability. This can be controlled using two different types of monitors, a PIN diode for the primary light, and a reference PMT for stability control after the light distribution system. A stability feedback system may be employed for long term stabilization.

Light emitting ultra bright diodes have been developed during the last decade. There are commercially available ultra bright LEDs of different color. In reference[26], a yellow LED of luminosity up to 15 Cd manufactured by Hewlett Packard company [29] was discussed. The peak emission wavelength is 590 nm. There are also available blue and green LEDs with peak emission wavelengths of 472 and 526 nm (HLMP-CB and HLMP-CM, [30]), respectively.

Xenon flashers provide high intensity light with wave lengths and pulse shapes similar to scintillation light. However, they have two disadvantages—relatively long signals (about 300 ns), and intensity instability. An important problem is also maintenance. For the purpose discussed in this Conceptual Design Report, the most advantageous solution seems to be a laser source, which can provide uniform light of sufficient intensity to ~ 1200 channels.

3.8.3 Estimated Budget

The estimated cost of the monitoring system is presented in table 11. The estimation is based on quotations received from vendors. Miscellaneous items include those related to the fabrication of a system for fiber transparency measurements, as well as photometers, PIN diodes, epoxy, fiber cutting and polishing tools, *etc.*

3.9 Data Acquisition Electronics

The fast trigger electronics to be used in this experiment must provide a quick and accurate evaluation of potential π^0 events. Since the rate of π^0 production is somewhat small, it

Item	Unit Price	Quantity	PrimEx Request
Laser LN 203, 100 μ J/pulse	\$7,500.00	1	\$7.5k
Laser Container	\$3,000.00	1	\$3.0k
LGW-3900 Safety Goggles	\$35.00	4	\$0.1k
PIN Photodiode		5	\$0.1k
Filter Wheel	\$3,000.00	1	\$3.0k
Optics (lenses, stands, semi-transparent mirror)			\$4.0k
10 m fiber cable (d=1mm)		1	\$2.0k
2.0 m fiber cables (d=0.2mm)		1200	\$8.4k
3.0 m fiber cables (d=0.2mm)	\$61.80	30	\$1.9k
6.0 m fiber cables (d=0.2mm)	\$72.60	30	\$2.2k
ST Coupler	\$10.00	1200	\$12.0k
ST Mounts	\$6.00	1200	\$7.2k
Americium/Scintillator Light source	\$1,000.00	2	\$2.0k
Electronics and stability feedback system			\$5.0k
Miscellaneous (see text)			\$5.0k
Total			\$63.4k

Table 11: Budget for the gain monitoring system.

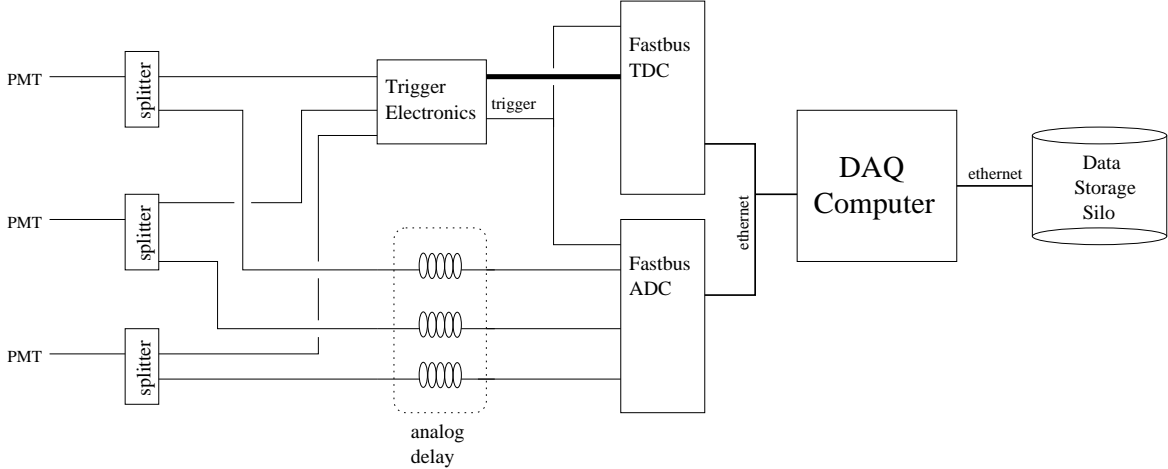


Figure 28: Simplified trigger schematic

is important to have a trigger design which has $\sim 100\%$ acceptance efficiency. At the same time, background events must be suppressed sufficiently enough to prevent a large background data rate. The rejection efficiency becomes important in the sense that a large background rate would reduce the live time of the data acquisition system (DAQ) and thus, miss real Primakoff events.

With the proposed beam intensity of 7.2×10^7 equivalent photons, we can expect a π^0 rate of approximately 1 Hz in our detector using the ^{12}C target.

Basic Design A simplified diagram of the DAQ system can be seen in figure 28. The signal from the photo-multiplier tube (PMT) is split with one half to be used for the trigger and the other half delayed and eventually digitized. The basic components are described in detail below. Descriptions of components specific to the trigger design are given in a later section.

Splitters The PMT signals may need to be split, depending on the specific triggering scheme used (see below for details on the trigger schemes studied). We are currently considering using the dynode signal from the PMT for the trigger so that the anode signal can go completely to the digitization electronics and, therefore, give us the best possible energy resolution. We will test the quality and stability of the dynode signal to determine whether or not it can be used. If we find the dynode signal is unsuitable, we will split the anode signal and use it for both the trigger and digitization as indicated in the diagram. We will use passive splitters which will be constructed by the collaboration. The splitters will provide 50% of the signal to the digitization electronics and split the remaining 50% in as many ways as are necessary for the specific triggering scheme used. Thus, all splitting of the PMT signals will be done simultaneously in a single splitter saving on cost. Assuming each channel will need to be split three ways, we will require two LEMO style connectors (outputs) and two BNC style connectors (one input, one output) for each channel. With 4

connectors per channel with an average cost of \$3 per connector, and an additional \$2 per channel for resistors and wire etc., the splitters can be built for approximately \$14/channel using labor within the collaboration. The experimental setup requires 1088 channels, but we will build 1100 so as to have spares, bringing the total cost for all splitters to \$15.4k.

Analog delay lines It will be necessary to delay the part of the analog signal which is to be digitized until the trigger logic has decided whether or not to record the event. This will be accomplished using long coaxial cables (such as RG58). Cable of reasonably good quality with non-contaminating jackets which are flame resistant can be purchased for \$135 per 1000 ft. The calorimeter has 1088 channels. Add to that the 32 channels from the luminosity monitor, 20 veto detector signals, and 12 spares and we will need to delay 1152 channels. The trigger electronics (described in section 1.2) will require a delay of 200 ns (167 ns estimated plus a wide error margin). These cables can be purchased pre-made at 200 ns lengths with BNC connectors on both ends for \$26.15 each. The total cost for all the necessary delay cables will be \$30.1k. Special consideration must be given to the logistics of handling the 20+ miles of delay cable. Some type of support structures will be needed to aid in organization and support of these cables. We feel the cost of constructing these support structures will be small enough that they can be provided by the collaboration.

An alternative to the delay cables is the analog delay chip such as the 2211 made by Digital Delay Devices Inc. A single chip can provide one channel of the full 200 ns delay required. These can be purchased for less than \$10 a piece in quantity and could, thus, significantly reduce the cost of signal delays from \$26 per channel to \$15 per channel. The collaboration is exploring the possibility of using these devices and testing them to see if they would satisfy the needs of the experiment.

Readout electronics We will use Fastbus data acquisition electronics for digitization of the detector signals. We plan to use LRS1880 series ADC and TDC modules or equivalent. Most models of these modules have 64 channels a piece. A total of $1200/64 \Rightarrow 19$ ADC modules would then be required. Every discriminator used in the trigger electronics will also be recorded by a TDC module. Since a relatively small number of discriminators are called for by the trigger design, only one TDC module will be required. Only one Fastbus crate will be required if 64 channel modules are used. These modules and the Fastbus crate, power supply, and bus master will all be supplied by the collaboration.

Data Acquisition Software For the data acquisition software, we will use the CODA system already in place in Hall B. The system has been used very successfully with the acquisition of data from the CLAS detector. Additionally, there are several experts on-site in the on-line DAQ group at Jefferson Lab who can help. The CODA system implemented in Hall B for CLAS is based on small microprocessor based modules which reside in the Fastbus crate and have a high speed connection to a dedicated ethernet. We plan to follow the CLAS model closely so that we may use certain CLAS resources which will be otherwise unutilized since CLAS can not take data with our detector in place.

Data storage For long term data storage, we will use the Jefferson Lab tape silo. The silo is already well integrated with the Hall B DAQ used by CLAS and has more than enough capacity to serve our needs.

Specific Trigger Designs A study has been made of four possible designs for the trigger logic to be used in this experiment. Simulations were done to test each of the four, and the results are summarized in sec. 2. Each of the four trigger designs is described here.

Trig1 The first trigger linearly fans-in groups of detectors approximately 4 units high that span the width of the detector (see fig. 33). There are 7 such strips and another 7 made from identical groupings, rotated 90 degrees w.r.t. the first group. Each strip is discriminated at a level of 1/2 of the minimum energy π^0 decay photon we wish to detect. This level is set to 0.5 GeV since we wish to accept all events with photon energies 1 GeV or higher. The 7 strips of each direction are taken to form a 14 bit word which is then used to access an address of a Memory Mapping unit (MMU). Patterns in which 1.) two non-adjacent strips fire in one direction or 2.) two adjacent strips fire in both directions will create a trigger.

Trig2 The second trigger is based on the same idea as the first, only it defines 15 strips in each direction. This will create a 30 bit word. The finer strips allow it to require only that two non-adjacent strips fire and ignore the "two adjacent strips in both direction" events allowed with trig1.

Trig3 The third trigger defines overlapping groups of detectors. Each group is discriminated at the minimum π^0 photon energy level (1 GeV). The groups are made of up to 36 elements each since the UVa120 linear fan-in modules we plan to use can have up to 36 inputs. Since the two photons from a π^0 decay can hit two adjacent groups, a coincidence which requires the two photons be separated by a certain distance is not possible without losing some real events. The trigger was therefore true if any two or more groups fired. Since this method has a larger number of discriminated signals (~ 60), the MMU would be replaced with a 64-channel majority logic unit.

Trig4 The fourth trigger uses a single discriminator threshold on the sum of all the detectors. This would not be feasible to implement in the actual experiment as was done in the simulation since the insertion detectors will have a different pulse width and size than the outer blocks and, therefore, cannot be linearly fanned-in together. However, simulating its performance is useful as a comparison to the other trigger designs.

3.9.1 Simulations and results

Simulation software Simulation of the experimental apparatus was done using GEANT. The simulation incorporated several pieces of the experimental apparatus as seen in fig. 29, but excluded things such as the as-of-yet-undisigned support structure for the calorimeter.

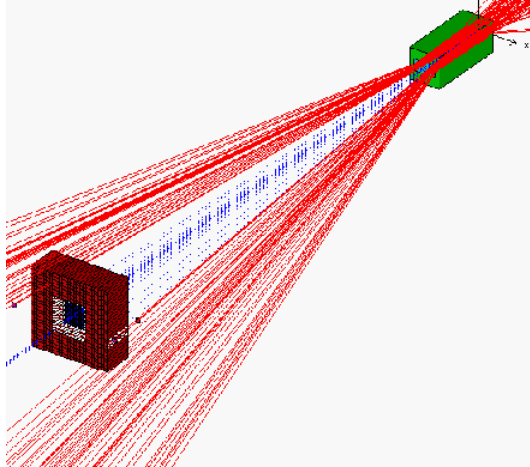


Figure 29: GEANT geometry

This, along with things such as electronics racks and the metal grating that makes up the floor are possible sources of backgrounds due to scattered particles. Backgrounds from these external objects should be small.

Geometry Elements included in the simulation are:

Target: Made of a $1 \times 1 \text{ cm}^2$ piece of lead that was 5% of a radiation length (0.028 cm) thick.

Sweeping Magnet: a $40 \times 40 \times 100 \text{ cm}^3$ piece of iron with a $30 \times 15 \text{ cm}^2$ opening. The magnet was given a field strength of 15 kG.

Calorimeter: Made of 608 lead-glass blocks ($4 \times 4 \times 40 \text{ cm}^3$) and 480 PbWO_4 crystals ($2 \times 2 \times 20 \text{ cm}^3$). Each individual detector has a 50 micron Al wrapping with a 50 micron air-gap between the wrapping and the detector. The front face of the calorimeter was positioned 7.5 m downstream from the center of the target.

Pair counters: Small plastic scintillators were placed symmetrically on either side of the calorimeter. These will not be used in the trigger.

Virtual absorber wall: A thick $54 \times 54 \times 50 \text{ cm}^3$ wall of PbWO_4 was defined directly behind the calorimeter. This was added after it was noticed that for some events, a significant portion of energy incident on the calorimeter was unaccounted for. The word "virtual" was given since this will only exist in the simulation and not in the actual experiment.

Event Generators Simulations were done using two types of generated events. These were done separately. The first type of event produced a π^0 which was given an energy sampled from a $1/E$ bremsstrahlung distribution between 1 and 6 GeV. GEANT was allowed to

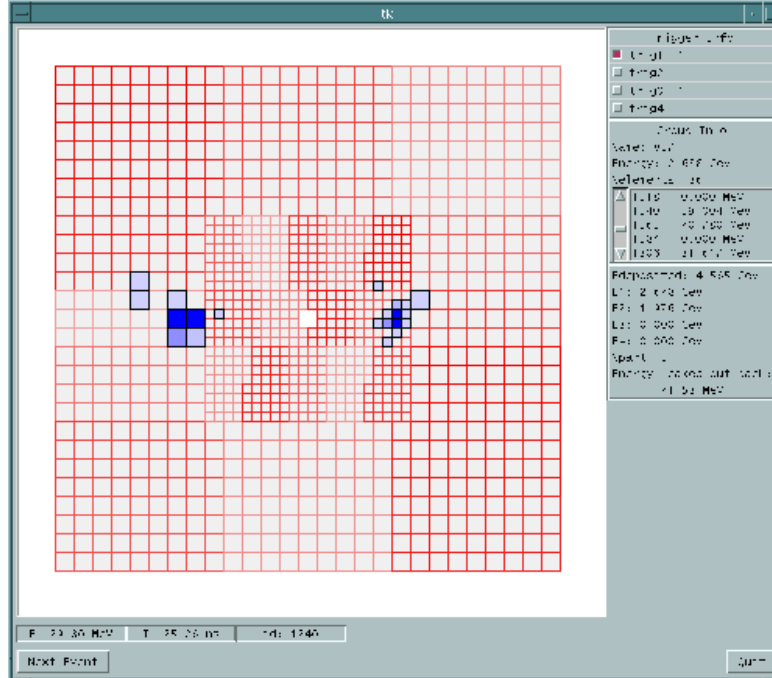


Figure 30: Single event viewer

decay the π^0 into two photons. The second type of event simulated photons sampled from a $1/E$ bremsstrahlung distribution between 0.1 and 6 GeV incident on a lead target. Physical mechanisms including pair production, Compton scattering, and delta ray production (among others) were simulated.

Due to the small target thickness, most of these passed right through, and the event was discarded. The first event type (π^0) was used to measure the acceptance efficiencies of the various trigger designs while the second event type (background) was used to measure the rejection efficiencies. For this study, 3.5 π^0 events and 326M background events were generated.

Replay and visualization software The simulation program could output results of the simulation into a compressed binary file which recorded what was seen by every detector for every event. This saved time by allowing fine tuning of the trigger definitions without having to re-run the simulation. Additionally, software utilities were developed for examining individual events in detail (see fig 30). This gave much insight into specific reasons for failures of the various trigger designs as well as giving software that should easily be adapted to online and eventually, offline data analysis.

Acceptance efficiencies Acceptance efficiencies were calculated for each of the four trigger designs from the π^0 generated events. Acceptance efficiencies were calculated from events which passed a "good" test. The good test was defined by the following conditions:

- at least two particles hit the calorimeter

trig1	$99.94 \pm 0.24 \%$
trig2	$99.34 \pm 0.24 \%$
trig3	$96.82 \pm 0.24 \%$
trig4	$99.84 \pm 0.24 \%$

Table 12: Acceptance efficiencies

- both particles have an energy of 1 GeV or more
- the two particles are separated by at least 10 cm at the face of the calorimeter.

The "good" test was defined since trig3 and trig4 could fire on single particles in the calorimeter while trig1 and trig2 required a coincidence. This test effectively excluded events for which say, only one of the π^0 photons hit the calorimeter. These types of events would be of no use in the real experiment since critical information about the missing photon would be lost. The "good" test effectively removes the differing geometrical acceptances of the four triggers from the acceptance efficiency calculations.

The acceptance efficiency of a trigger was defined as the fraction of "good" events for which the trigger would have fired. The acceptance efficiencies for each of the four designs are listed here in table 12

The failures for trig1, trig2, and trig4 are due to energy loss through the back of the detector. The additional failures for trig3 are due to particles near 1 GeV hitting a border region and spreading the shower across three or more detectors such that no single group sees the full 1 GeV of energy.

Rejection efficiencies Rejection efficiencies were calculated for each of the four trigger designs from the beam-related background events. Since all events of this type should be rejected, no "good" test was applied as for the acceptance efficiency. The simulation was done using a single photon incident upon the Pb target for each event. In the actual experiment, several photons may combine in the calorimeter causing false coincidences. To take this possibility into account, the results of several background events were combined into single events and then tested with each trigger. A plot of the positive trigger event fractions vs. number of photons combined can be seen in fig. 31. This figure must be scaled, however, by the probability of having several photons randomly distributed in time occur within 50 ns of one another. This significantly suppresses the rates for combinations of 3 photons or more as shown in figure 32.

The integrals of the curves in fig. 32 give the total rates due to beam-related backgrounds for each trigger design which can be seen in table 13.

Conclusions from the simulation Of the four designs studied, trig1 appears to be the best choice. The large background rates from trig3 and trig4 make them unacceptable for this experiment. The thinner strips defined in trig2 made it possible for showers which spanned several modules to be missed by the trigger.

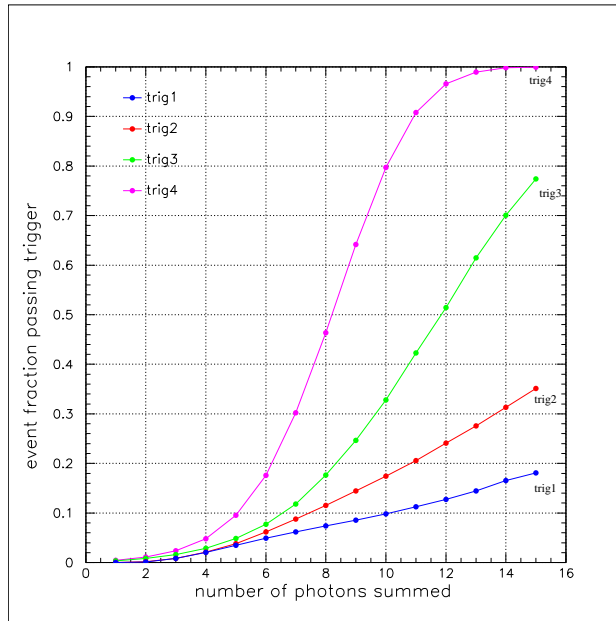


Figure 31: Event fraction vs. num photons

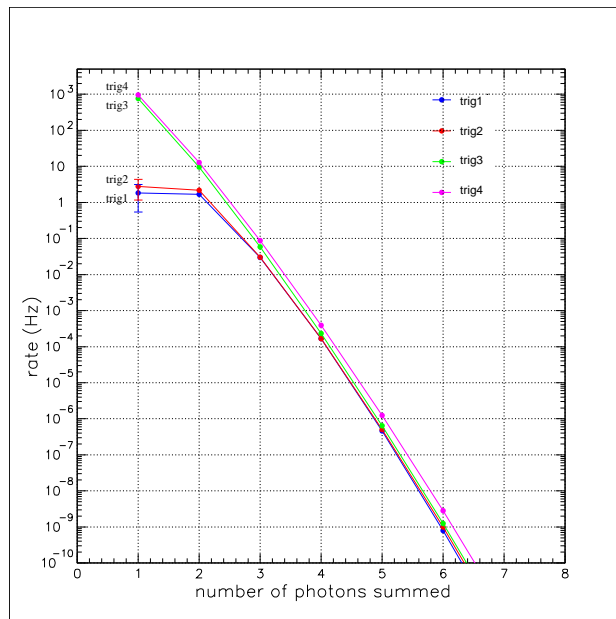


Figure 32: Event rate vs. num. of photons

trig1	3.5 ± 1.4 Hz
trig2	5.0 ± 1.7 Hz
trig3	771 ± 27 Hz
trig4	973 ± 30 Hz

Table 13: Background trigger rates

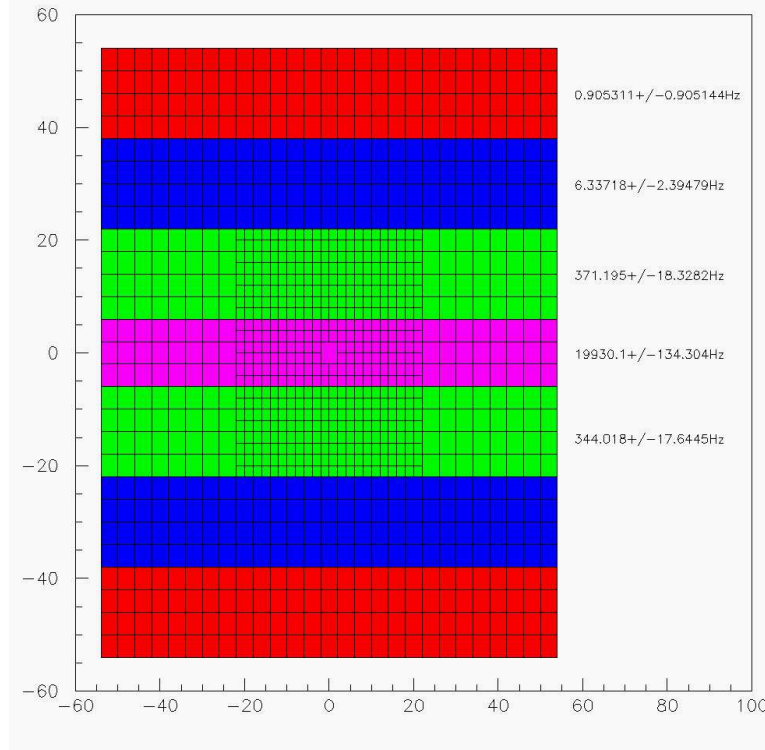


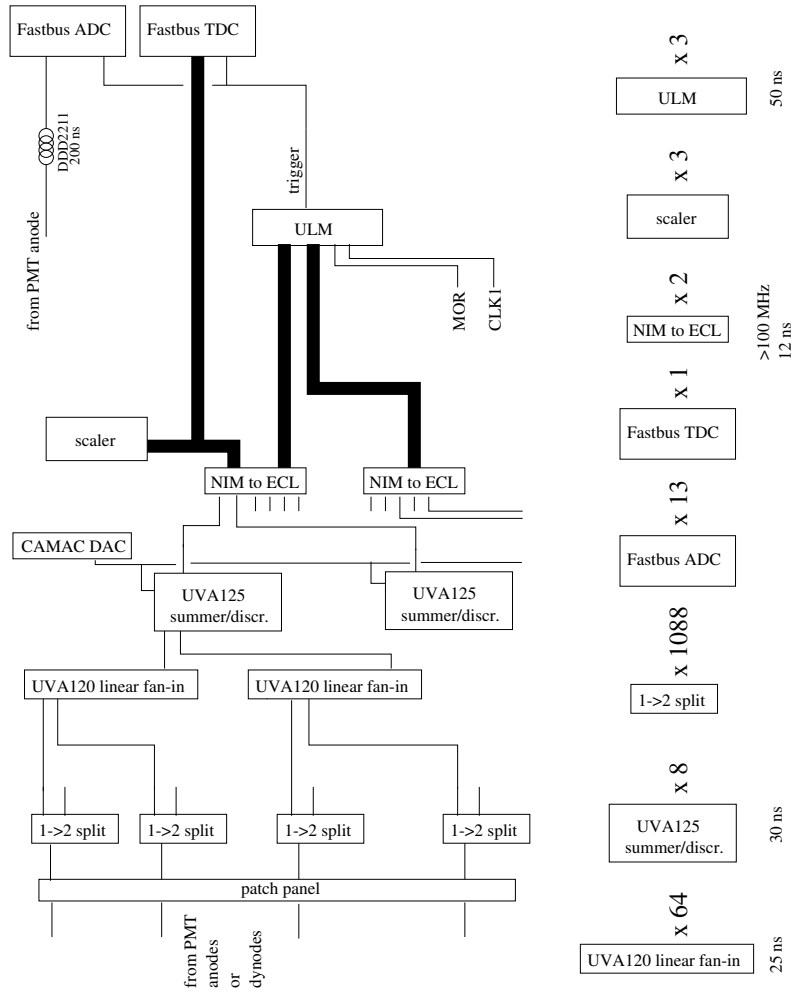
Figure 33: Rates in trig1 strips

Another result obtained from the simulation are estimates of the rates at which individual strips defined for trig1 fired. The central strip will have the highest rate at approximately 20 kHz as seen in fig. 33.

3.9.2 Estimated Budget

This section will provide an estimate for the cost of assembling the necessary hardware for implementing the trig1 design described in section 1. A schematic of the trig1 design can be seen in fig. 34.

UVA120 linear fan-in These modules designed and built by the University of Virginia are currently in use by the electromagnetic calorimeter in Hall-B at Jefferson Lab. They are 36 input linear fan-in NIM modules. These modules are highly desirable for the following reasons: 1.) Linear fan-ins with this many inputs are not commercially available. 2.) The



Total delay: $25 + 30 + 12 + 50 + 50 = 167$ ns (cables) = **167 ns total delay**

Figure 34: Trig1/Trig2 schematic

UVA120 has been shown to work reliably in Hall-B. 3.) The total cost of the UVA120's is significantly lower than implementing a similar design with the commercial modules which are available (less than 50%).

UVa will supply the labor and expertise to build these modules. The estimated cost for parts is \$500 per module. The trig1 design requires 64 of these modules. Adding 2 spares would bring this to 66 having a total cost of \$33k.

UVA125 linear fan-in/discriminator The UVA125 linear fan-in/discriminator has 4 separate sections each with a 9-input linear fan-in and two built in discriminators. This module has been used successfully in previous experiments. The benefits of using these modules are, again, the cost (\sim \$1k per module) and the simpler, more compact design. Alternatively, one would have to use separate linear fan-in and discriminator modules. Additionally, the timing of both discriminators is determined by that of the one with the lower threshold, making the timing properties better than single leading edge discriminators. The trig1 design groups detectors into 7 strips in the x-direction and another 7 in the y-direction. Trig1 would therefore require $(7 + 7)/4 \Rightarrow 4$ UVA125 modules.

The number of modules required to implement the trig1 design plus 1 spare would be 5 having a total cost of \$5k.

CAMAC digital to analog converter (DAC) The UVA125 modules can have the discriminator thresholds set via externally supplied voltages. These voltages will be supplied via a CAMAC DAC module so that the thresholds may be adjusted remotely without making an access to the experimental hall. A module of this type is estimated at a cost of \$2k.

NIM crates A minimum of 7 NIM crates will be required to hold all of the modules needed for the trig1 design. There are sufficient resources within the collaboration to supply all the NIM crates required.

Fastbus ADC and TDC modules See section 1.1.3 for a description of the Readout Electronics.

Logic Module The two particle coincidence will likely be determined by CAMAC modules. The current design can be accommodated by either the LRS2373 Memory Lookup Unit (MLU) or the LRS2367 Universal Logic Module (ULM). The LRS2373 is basically a RAM chip with 16 inputs and 16 outputs. The trig1 design can be done using only one of these modules since it requires $2 \times 7 = 14$ inputs. Additionally, the LRS2373 is known to have poor timing properties. The LRS2367 would perhaps be the better choice. The LRS2367 is based on a Xilinx 4013E FPGA chip. It has 59 programmable input output lines so one module would be sufficient. At \$3.7k, the price per module of the LRS2367 is comparable to the \$3.4k price of a LRS2373. Additionally, the LRS2367 has much more flexibility should the logic algorithm need modification.

Scalers The rate of every discriminator channel used in the experiment will be counted via a CAMAC scaler module. The model 7132H 32-channel scaler by Phillips Scientific will be used. While these scaler values may not be needed in the final data analysis, they could provide invaluable diagnostic information while online as well as some consistency checks. Only two such modules will be required at a cost of \$3.1k per module.

High Voltage The calorimeter will require 1088 negative high voltage channels for its PMTs. Several additional HV channels will be required for the PMTs used by the luminosity monitors, and the charged particle veto detector. A total of approximately 1140 HV channels will be required. Experiment E-97-108, to be performed in Hall-A at Jefferson Lab, is constructing a calorimeter similar to the one for this experiment. The collaborators for the Hall-A experiment have already appropriated the HV channels needed for their calorimeter and have agreed to loan us 768 channels contingent that our beam-time schedules do not overlap. The remaining 372 channels will need to be purchased. The E-97-108 collaboration has purchased LRS1458 mainframes with 1461N HV modules. Two additional mainframes with 16 cards each for a total of 384 HV channels may be purchased for \$40k each (\$80k total). The HV supplies will need cables which are about 25 ft long. A vendor has estimated the price per unit at \$28.25 per 25 ft. cable. The total cost of the HV cables thus comes to \$32.5k.

The total cost of HV cables and supplies is \$112.5k.

CAMAC crate A single CAMAC crate and crate controller will be required. These will be supplied by the collaboration.

PC for CAMAC A small computer will be required for communicating with the CAMAC controller in the hall. This PC will not need to be very powerful since CAMAC will only be used for setting the trigger logic and reading out the scalers. It will, however, need an ethernet card in order to communicate with the counting house and the rest of the DAQ. This computer will be supplied by the collaboration.

Signal cables A large number of signal cables will be required for this experiment. These are the cables which will connect the outputs of the PMT's to the inputs of the trigger logic. These cables will have LEMO style connectors and will be purchased ready made to ensure the highest quality and consistency. These cables will be of varying sizes, all 32 ns or less in length. Pre-made cables of this size have a price which is basically independent of length. A vendor has estimated the cost per unit to be at \$18.45 per cable for 16 ns cables. The signal cables from the PMT's will be connected to a patch panel. Additional cables will be used to connect the patch panel to the input of the analog splitters. These cables will be made of varying lengths so that the signals may be aligned in time. This is where account will be made for any differences in timing due to PMT drift times etc. Approximately 1100 cables will be required to connect the patch panel and splitters. Another $2 \times 1100 = 2200$ cables will be required to connect the output of splitters to the input of UVA120 modules. The output of UVA120s will require another set of cables to connect them to the input of

Item	Quantity	Unit Price	PrimEx Request	JLab	Collab.	Other
Patch panel	2×1200	\$6/chan	\$14.4k			
Passive splitters	1200	\$17.40/chan	\$20.9k			
UVA120 linear fan-in	64+2 spares	\$500	\$33.0k			
UVA125 linear fan-in/discr.	4+1 spare	\$1k	\$5.0k			
CAMAC DAC	1	\$2.3k	\$2.3k			
NIM crate	8	\$2k	\$16.0k			
NIM to ECL module	2	\$2k	\$4.0k			
Fastbus Crate w/ controller	1	\$22k		\$22.0k		
Fastbus ADC modules	24	\$7k				\$168.0k
Fastbus TDC modules	1	\$8.1k			\$8.1k	
LRS2367 Univ. Logic module	2	\$3.4k	\$6.8k			
P7132H CAMAC scaler	2	\$3.1k	\$6.2k			
HV mainframes (LRS 1458)	2	\$12k	\$24.0k			
HV modules (LRS 1461N)	32	\$2.3k	\$73.6k			
High Voltage cables	1152	\$30	\$36.0k			
Analog delay lines	1152	\$26.15	\$30.1k			
CAMAC crate w/ controller	1	\$9.0k			\$9.0k	
Small (~ 16ns) signal cables (LEMO type)	4500	\$18.45	\$83.0k			
Electronics racks	5	\$3.0k		\$15.0k		
PC for communicating with CAMAC	1	\$2.0k			\$2.0k	
Total			\$355.3k	\$37.0k	\$19.1k	\$168.0k

Table 14: Budget for data acquisition electronics

UVA125s. This set will require 64 more cables for trig1. Additional cables will be needed for the luminosity detectors and charged particle veto. A best estimate for the total number of cables of this type required is 3500 for a total cost of \$64.6k.

Racks for Electronics Five Racks suitable for mounting the NIM bins, CAMAC crate, and Fastbus crates will be required. At least two full racks will be needed for the patch panel and splitters. Electronic racks of this kind can be purchased for approximately \$3k a piece.

DAQ Budget The University of Massachusetts is responsible for the implementation and assembly of the trigger electronics and the DAQ system. A summary of the DAQ budget can be seen in table 14.

4 Experimental Considerations

4.1 Count rate estimates and beamtime

A Monte Carlo generation of π^0 events in the proposed experimental setup has been done for several nuclear targets. In these simulations all amplitudes contributing to this process were used normalized to the available experimental data for $E_\gamma=6.6$ GeV [11]. The expected experimental yields in six day runs for 5% r.l. ^{12}C and ^{208}Pb targets are shown in figures 35 and 36, respectively. The errors shown are for $\Delta\theta_\pi = 0.01^\circ$ bins and are statistical only. A tagged 8×10^6 γ/sec intensity photon beam was assumed for the accepted energy interval $E_\gamma = (0.85 - 0.95)E_\sigma$.

The expected rate for each channel will be about 1 MHz, which is two times less than the maximum design count rate [47]. The total π^0 rate for lead integrated for the $\theta_\pi = 0^\circ - 2^\circ$ angular interval, and for the parameters listed above is expected to be:

$$Rate = N_\gamma \times N_{nuclei} \times \Delta\sigma \times E_{eff} \approx \quad (23)$$

$$\approx 8 \cdot 10^6 \times 9.2 \cdot 10^{20} \times 2.16 \cdot 10^{-2} \cdot 10^{-27} \times 0.7 = 9600 \text{events/day}. \quad (24)$$

The generated angular distributions were fitted with the following procedure: for each $\Delta\theta_\pi$ bin the number of expected events $n_i(\theta_\pi)$ was calculated for each component of the cross section by folding in the bremsstrahlung spectrum and the detector angular resolution and acceptance. The solid lines on the figures show the result of the fit with the extracted values for all four free parameters. From these data, a 0.9% statistical error for the $\pi^0 \rightarrow \gamma\gamma$ decay width will be achieved. In this energy range the magnitude of the nuclear amplitude is small (≤ 2 %, see figure 3 and 4. To test that it has been properly taken into account, we will extract the Primakoff cross section independently for each of the three targets, and check that it is proportional to Z^2 .

We are requesting a total of 19 days for production data taking, 7 for ^{12}C , and 6 each for ^{116}Sn and ^{208}Pb . In addition, we estimate three days of beam time will be necessary for the empty target runs and for the calibration of the multichannel lead glass/ PbWO_4 detector. Therefore, we estimate a total of 22 days of beam time for the determination of the $\pi^0 \rightarrow \gamma\gamma$ decay width with a statistical error less than 1%.

4.2 Background rates

For high photon energies, the dominant photoabsorption mechanism involves the production of the vector mesons ρ , ω , and ϕ . In this experiment, only the ρ and ω decays are expected to produce measurable π^0 rates on the detector. The proposed experiment will greatly reduce the uncertainty due to contamination of the Primakoff signal from the other channels for two reasons. First, the proposed hybrid π^0 detector consisting of a wall of lead glass detectors and a high resolution insertion will significantly increase pion angular and energy resolutions, thereby enabling tighter cuts on the Primakoff events. Second, the tagging technique provides a powerful kinematical constraint which was not present in previous experiments employing bremsstrahlung beams. The production cross sections for the ω and

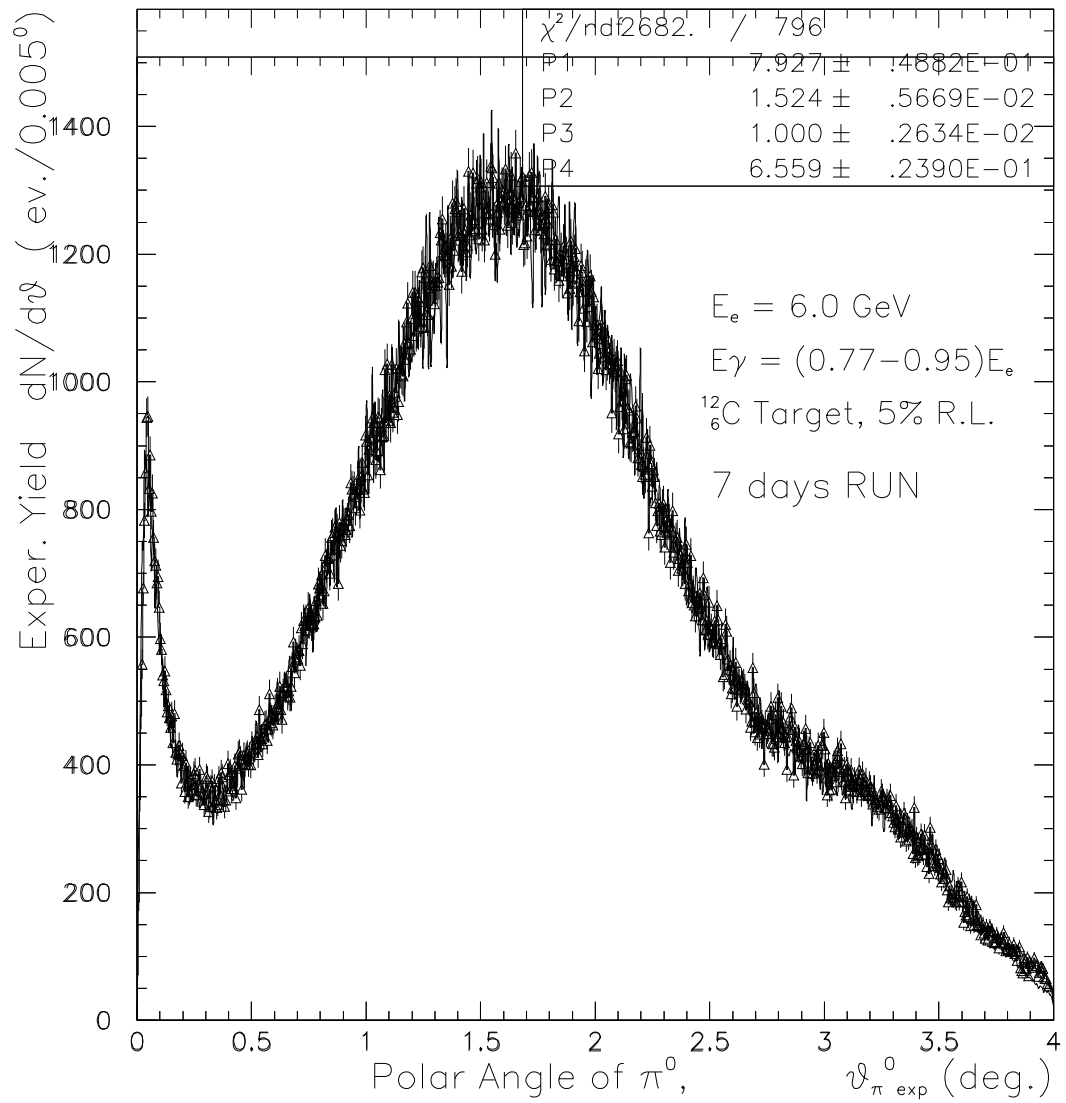


Figure 35: Expected experimental yield vs. θ_{π^0} for 6 days of running on carbon.

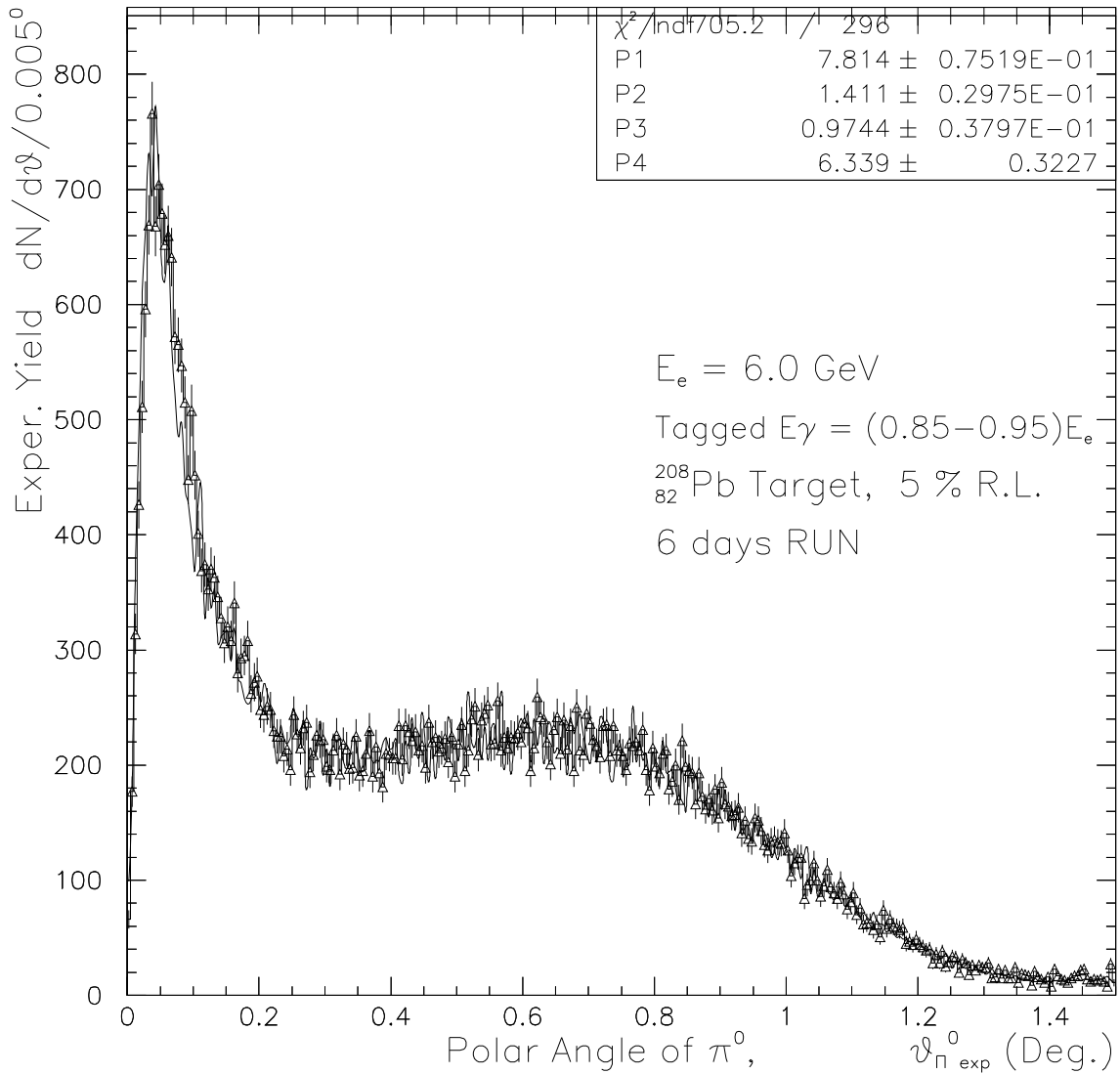


Figure 36: Expected experimental yield vs. θ_{π^0} for 6 days of running on lead.

ρ have been calculated, and their subsequent decays via $\omega \rightarrow \pi^0\gamma$, $\omega \rightarrow \pi^0\pi^-\pi^+$, $\rho \rightarrow \pi^0\gamma$, and $\rho \rightarrow \pi^+\pi^-\pi^0$ have been simulated in GEANT.

The cross section for ω production on complex nuclei is given by:

$$\frac{d\sigma}{dt} = \frac{d\sigma_{A,coh}}{dt} + \frac{d\sigma_{A,incoh}}{dt} \quad (25)$$

The coherent part is given by[48]:

$$\frac{d\sigma_{A,coh}}{dt} = \frac{d\sigma_{Pom}}{dt}(t=0) \cdot e^{Bt} \cdot |A_{eff}^{coh}|^2 \cdot |F(t)|^2 \quad (26)$$

where t is the Mandelstam variable, $\frac{d\sigma_{Pom}}{dt}(t=0)$ is the Pomeron exchange cross section[49], B is taken to be 7 GeV^{-2} [49][50][51], $F(t)$ is the nuclear form factor, and $A_{eff}^{coh} = \sigma_T(\gamma A)/\sigma_T(\gamma N)$ is taken from [52].

The incoherent cross section is given by[48][53]:

$$\frac{d\sigma_{A,incoh}}{dt} = \left[\frac{d\sigma_{Pom}}{dt} + \frac{d\sigma_{OPE}}{dt} \right] \cdot A_{eff}^{incoh} \cdot G(t) \quad (27)$$

where A_{eff}^{incoh} is the effective number of nucleons contributing to incoherent vector meson production[52], and $G(t)$ takes into account suppression at small t due to nuclear correlations.

The two body decay $\omega \rightarrow \pi^0\gamma$ (B.R. 8.5×10^{-2}) was sampled in GEANT, with an angular distribution proportional to $(1 + \cos^2\theta_{c.m.})$ [54]. The three body $\omega \rightarrow \pi^0\pi^-\pi^+$ decay (B.R. 8.9×10^{-1}) was sampled according to three body phase space. Figure 37(a) shows the missing energy spectrum ($E_\gamma - E_{\pi^0}$) obtained from the simulation of ω photoproduction and subsequent decay for six days of beam time with a lead target. Since the coherent pion photoproduction will appear as a peak near $E_{miss} = 0 \text{ GeV}$, figure 37(a) illustrates how knowledge of the incident photon energy provided by the tagging technique enables one to greatly minimize contamination of the π^0 spectrum. A further reduction is given by the stringent cut on θ_{π^0} enabled by the high resolution detector insertion. Figure 37(b) shows the angular distribution of π^0 's both with and without the four sigma missing energy cut indicated in figure 37(a). As the experimental θ_{π^0} distribution arising from photoproduction via the Primakoff mechanism will be confined to $\theta_{\pi^0} < 0.2^\circ$, a further substantial reduction of the ω background is obtained.

The ρ photoproduction cross section was taken to be ten times the ω cross section[53][55], and the resulting pion detection acceptance from the decays $\rho \rightarrow \pi^0\gamma$ (B.R. 7.9×10^{-4}) and $\rho \rightarrow \pi^0\pi^+\pi^-$ (B.R. $< 1.2 \times 10^{-4}$) were simulated. Figures 38(a) and 38(b) show the resulting missing energy and θ_{π^0} spectra for six days of running on lead, where in figure 38(b) the rates with and without the four sigma missing energy cut are also indicated.

Figure 39 shows the expected total π^0 angular distribution for ρ and ω photoproduction, along with the expected yield from the Primakoff mechanism, where missing energy cuts have been imposed.

4.2.1 Accidentals

Figure 40(a-c) shows the spectrum of single γ events from (a) $\omega \rightarrow \pi^0\gamma$, (b) $\omega \rightarrow \pi^0\pi^+\pi^-$, and (c) the total singles rate from the omega. The singles rates for the ρ were calculated to be

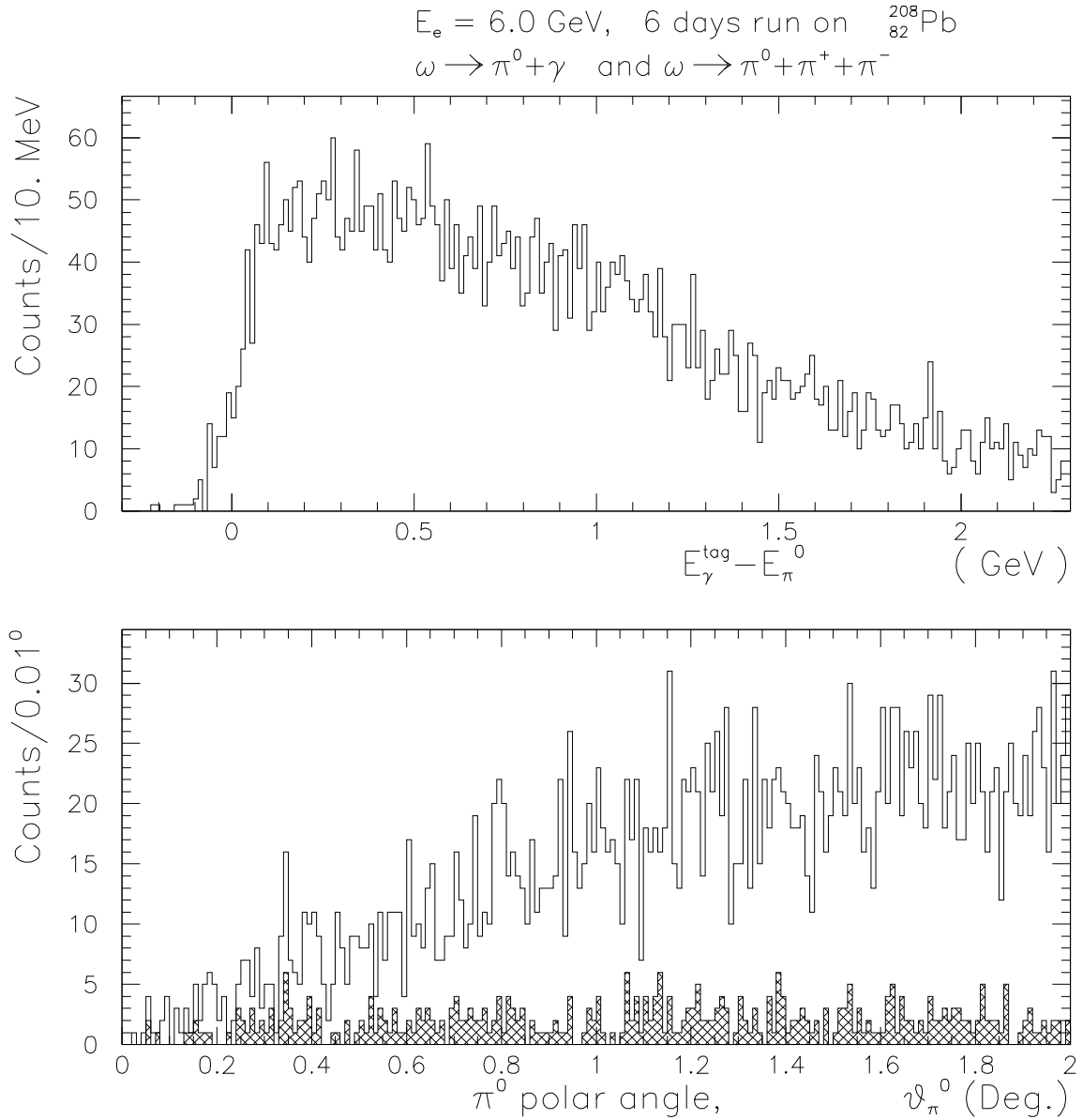


Figure 37: (a) Missing energy spectrum and (b) polar angle spectrum of π^0 's from omega decay. Open histograms represent total rates. Cross hatched histogram in (b) represents rates which pass a 4σ missing energy cut in (a).

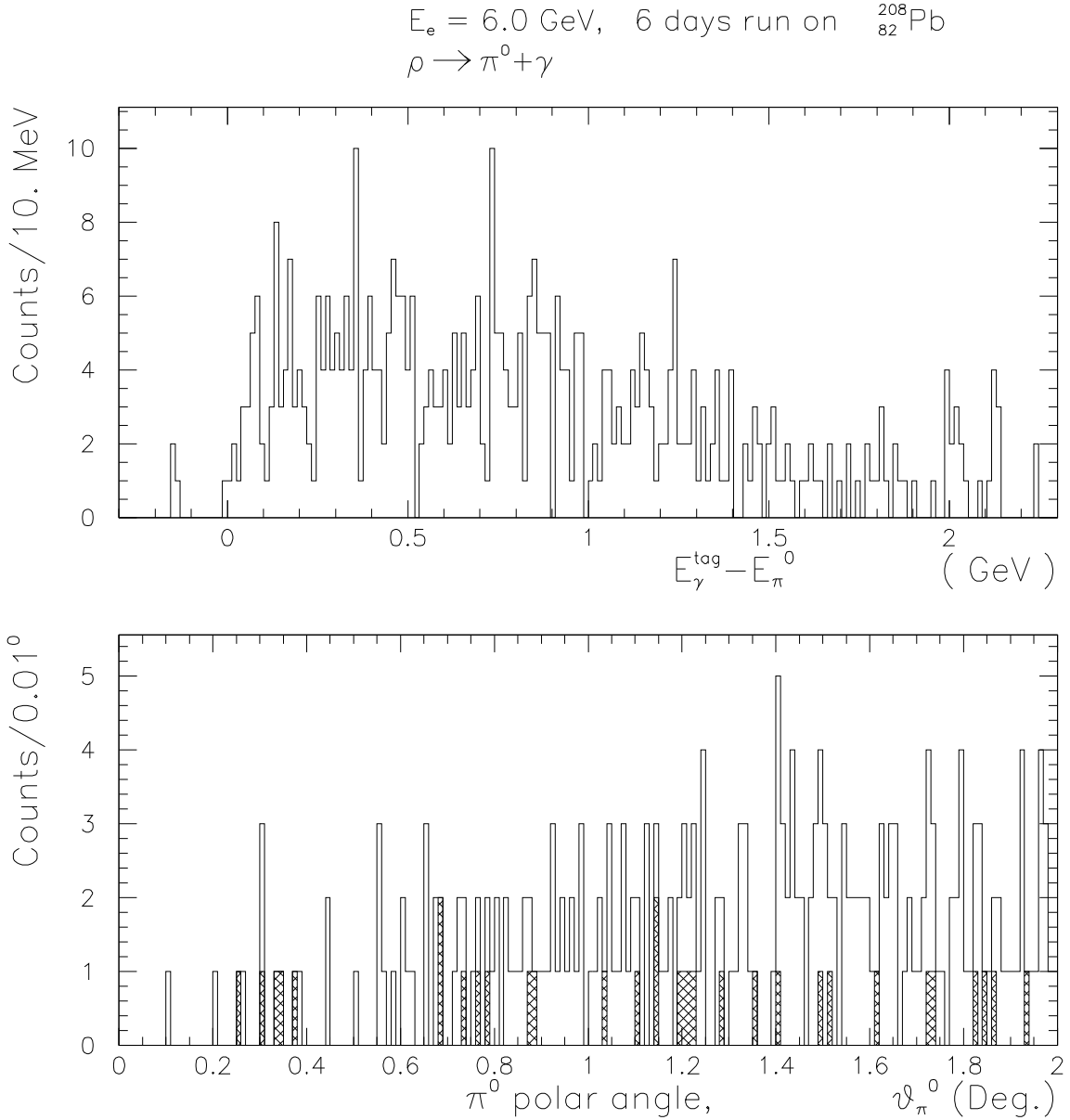


Figure 38: (a) Missing energy spectrum and (b) polar angle spectrum of π^0 's from rho decay. Open histograms represent total rates. Cross hatched histogram in (b) represents rates which pass a 4σ missing energy cut in (a).

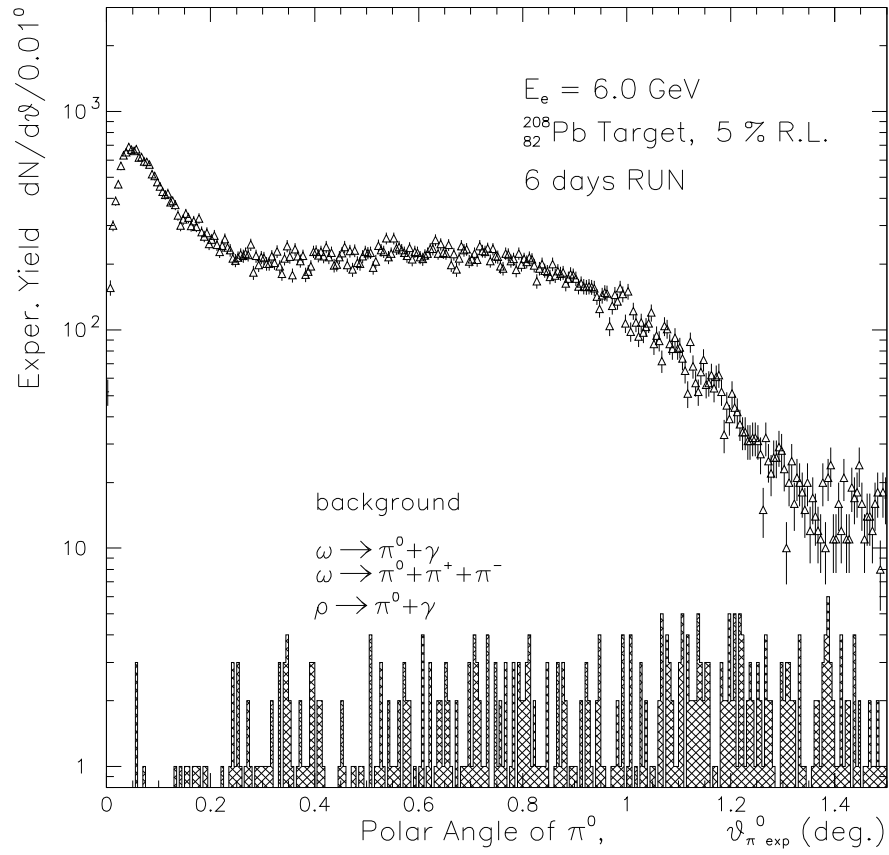


Figure 39: Cross hatched histogram: total π^0 background events vs. θ_{π^0} . Triangles: Photo-produced π^0 's.

1.4% that of the omega. Therefore, we expect about 0.8Hz single photon rate from physical background processes which will contribute negligible accidental background rates in the experiment. A summary of the expected singles rates of beam backgrounds determined by the GEANT simulation is shown below¹:

total singles (GEANT)	3.3 kHz
total accidental rate (GEANT)	4.0×10^{-2} Hz
π^0 signal rate (on <i>Pb</i> target)	0.11 Hz
raw trues/accidentals	2.8

When invariant mass, missing energy, and opening angle cuts are applied, the accidentals are expected to be negligible. The rates from GEANT are derived from a simulation including the Primakoff target, the pair production luminosity monitor, and the π^0 detector. The singles and accidentals rates are shown as a function of single particle threshold in figures 41(a) and 41(b), respectively. These rates include charged particles, as we do not plan to incorporate the charged particle veto which will be in front of the detector into the hardware trigger.

4.2.2 Correlated $\gamma\gamma$ backgrounds

The decays $\omega \rightarrow \pi^0\gamma$ and $\rho \rightarrow \pi^0\gamma$ result in three photon states which are correlated in time. Figures 42(a-d) and 43(a-d) show the correlated two photon rates as a function of (a) invariant mass, (b) missing energy, (c) $\psi_{\gamma_1\gamma_2}$, and (d) θ_{π^0} . No cuts are applied in the figures. In figure 42(a), the position and resolution of the π^0 invariant mass peak is shown, where the indicated peak height is reduced by a factor of 25 compared to that expected from Primakoff π^0 photoproduction. When π^0 invariant mass, missing energy, minimum $\gamma_1\gamma_2$ opening angle, and θ_{π^0} cuts are imposed, these correlated background rates are found to be negligible.

A GEANT simulation which takes into account secondary interactions in the Primakoff target and sweeping magnet indicates correlated two particle rates of around 10 Hz. While these will be present in the raw trigger, the majority of these are due to charged particles which will be vetoed offline.

4.2.3 π^0 backgrounds from the photon beamline

In addition to the Primakoff production target, other sources of π^0 's include the bremsstrahlung converter, the pole faces of the tagger magnet (6 cm gap), the 7.5 cm aperture of the iron shielding at the exit of the photon tagger, and the exit window between the pair production luminosity monitor and the π^0 detector.

The rate of π^0 's produced in the bremsstrahlung converter foil as a function of energy is shown in figure 44. These rates include π^0 's produced up to ten degrees due to Primakoff, nuclear coherent, and nuclear incoherent processes. Figure 45 illustrates the acceptance of the π^0 detector to these pions under the conservative assumption that all of these pions are

¹A discriminator threshold of 1 GeV was assumed.

$E_e = 6.0$ GeV, 4 days run on $^{208}_{82}\text{Pb}$

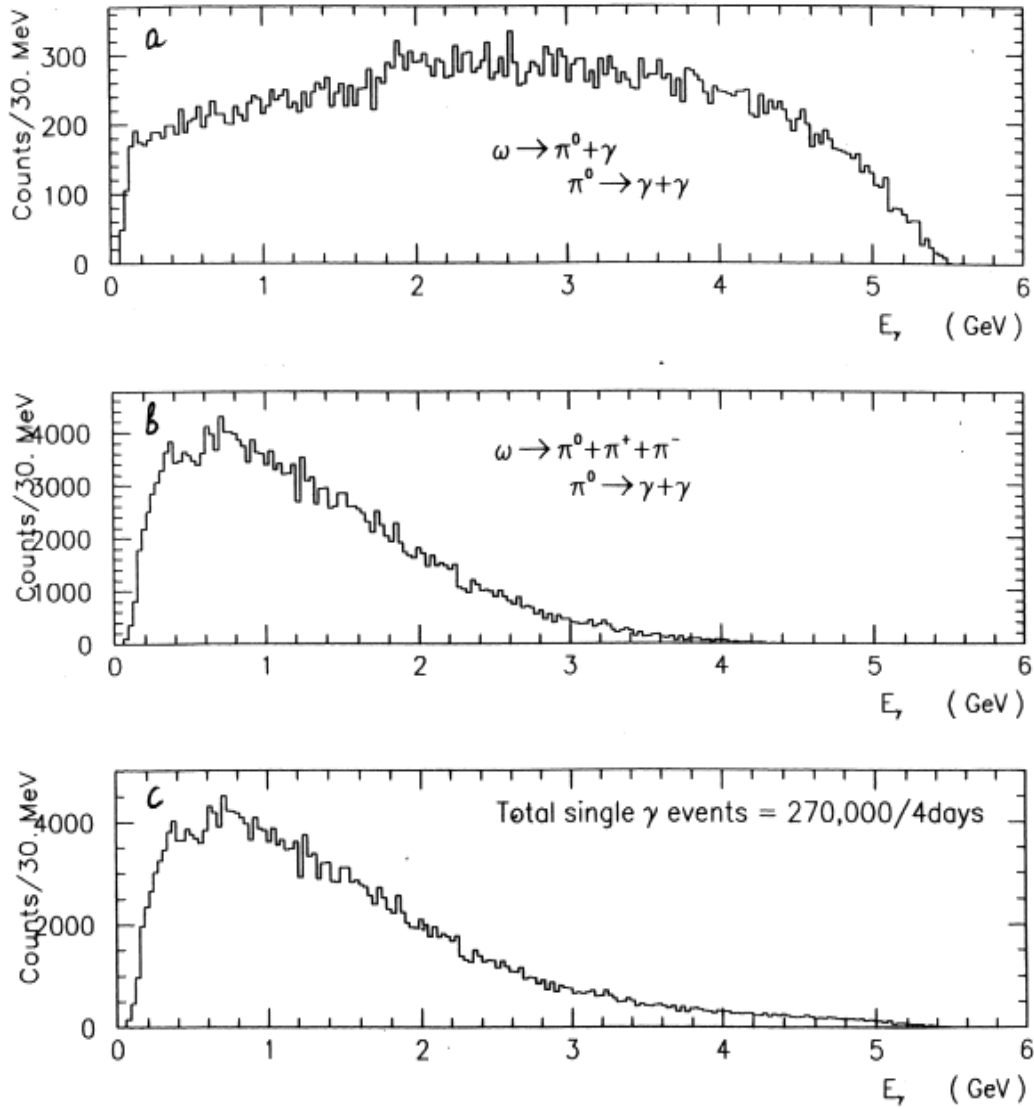


Figure 40: Single photon rate expected from four days of running on lead. (a) $\omega \rightarrow \pi^0 \gamma$, (b) $\omega \rightarrow \pi^0 \pi^+ \pi^-$, (c) Total singles from the omega meson.

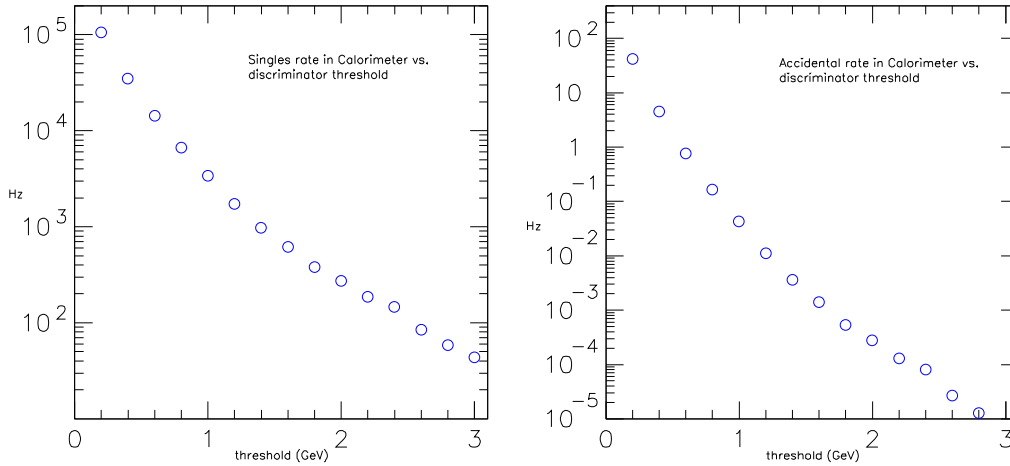


Figure 41: (a)Singles and (b), accidental rates in the π^0 detector as a function of single particle threshold.

emitted at zero degrees. Figure 45(a) shows the sampled spectrum of the pions produced in the bremsstrahlung foil, and figure 45(b) shows the energy distribution of the single photon events which reach the detector. This rate is calculated to be 0.3 Hz. As shown in figure 45(c), the two photon acceptance of pions produced in the converter foil is negligible.

Pions produced in the pole faces and the iron shielding near the exit of the tagger and those produced at the vacuum window between the pair production luminosity monitor and the π^0 detector can be distinguished on the basis of their reconstructed invariant mass spectra if one assumes that the π^0 's are produced in the Primakoff production target. When this assumption is correct, *i.e.* the pions are actually produced in the Primakoff target, one obtains the invariant mass distribution indicated in figure 46(a). Those which are produced in the vacuum window or in the iron shielding near the exit of the tagger, however, will give the reconstructed invariant mass spectra indicated in figures 46(b) and 46(c), respectively. While the π^0 backgrounds from along the photon beamline are expected to be small, and one can distinguish them on the basis of reconstructed invariant mass, we also plan to directly measure these rates in empty target runs in which the Primakoff production target is removed.

4.3 Pion final state interactions

The amplitude for coherent photoproduction of pions on nuclei consists of Coulomb and strong components. Each of these are factorized into the amplitude of photoproduction off a nucleon multiplied by a corresponding form factor. The Coulomb form factor which modifies the Primakoff cross section (see equation 3) and the strong form factor which modifies the

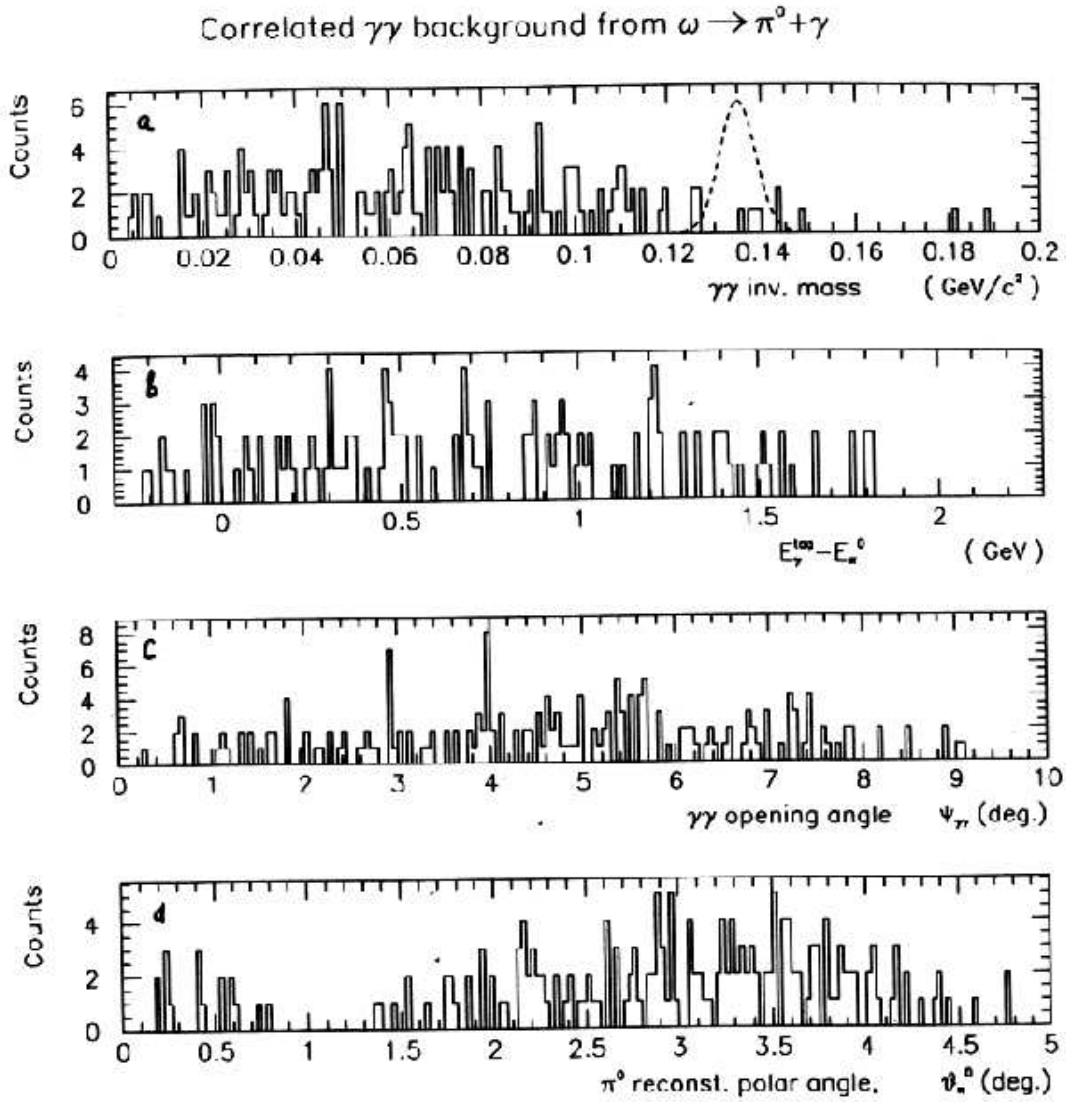


Figure 42: Correlated two photon rates from the omega as a function of (a) invariant mass, (b) missing energy, (c) $\psi_{\gamma_1\gamma_2}$, and (d) θ_{π^0} . No cuts are applied in the figures. In figure (a), the position and resolution of the π^0 invariant mass peak is shown, where the indicated peak height is reduced by a factor of 25 compared to that expected from Primakoff π^0 photoproduction.

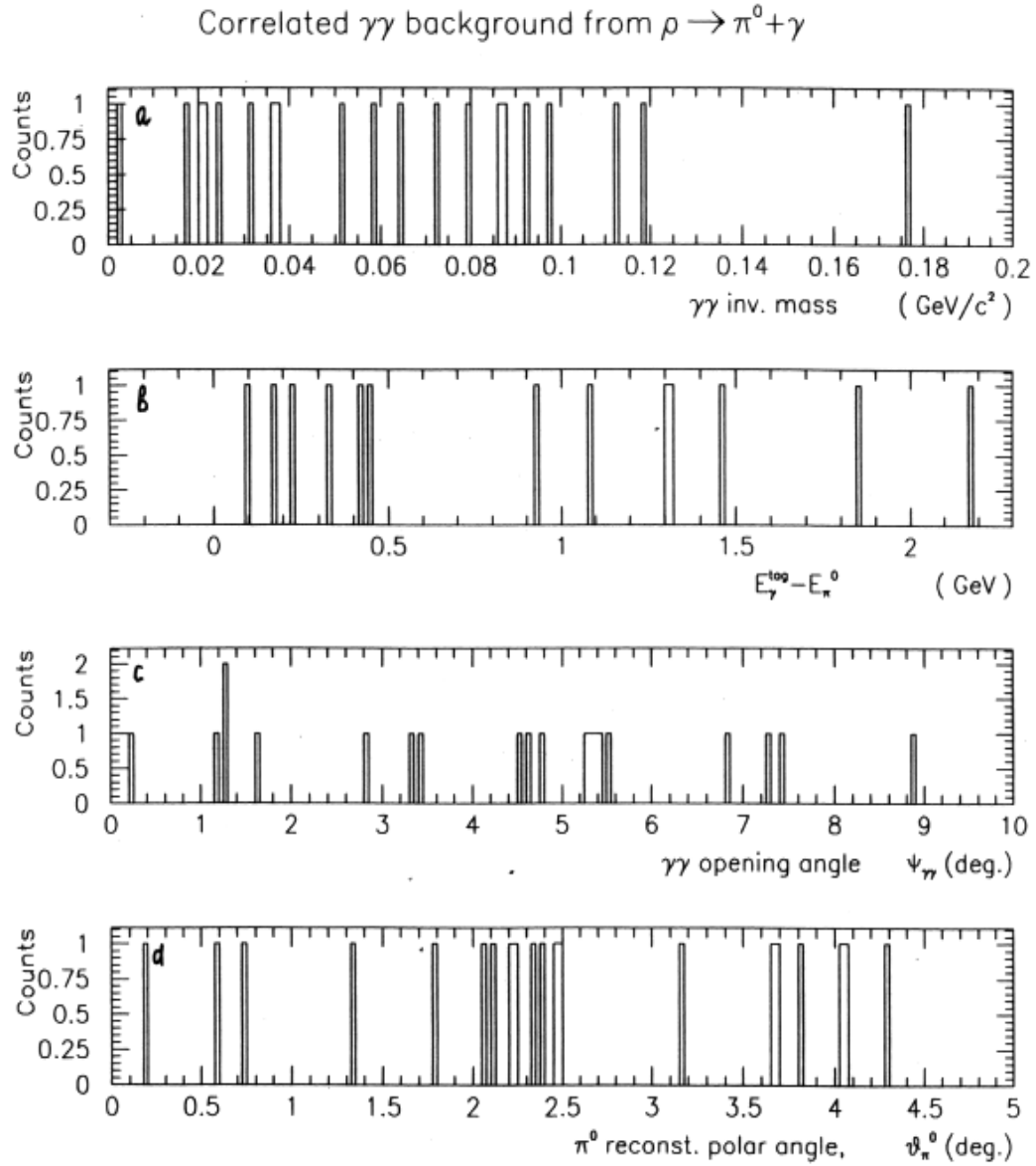


Figure 43: Correlated two photon rates from the rho as a function of (a) invariant mass, (b) missing energy, (c) $\psi_{\gamma_1\gamma_2}$, and (d) θ_{π^0} . No cuts are applied in the figures.

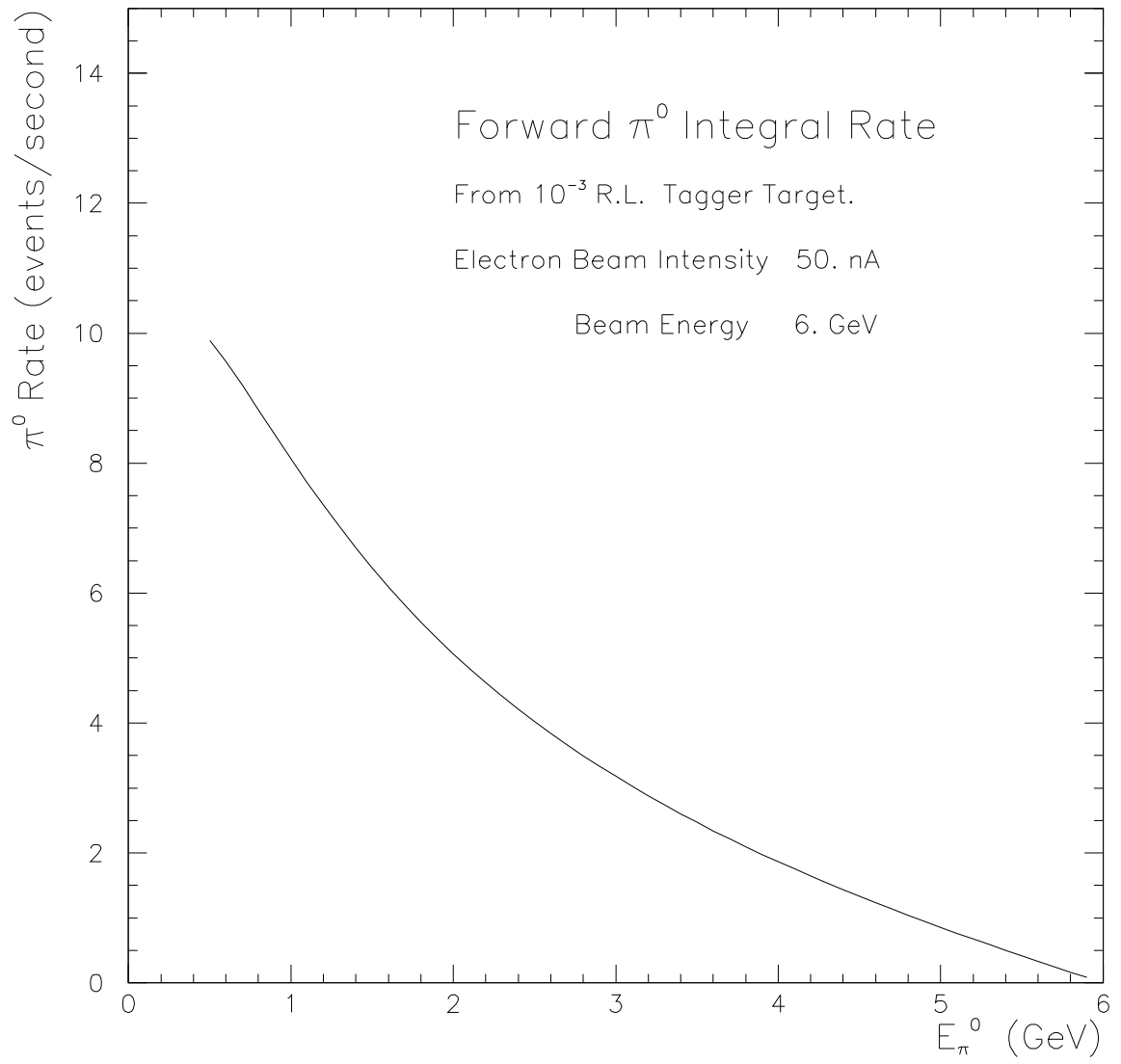


Figure 44: Rate of π^0 's produced in the bremsstrahlung converter foil as a function of energy.

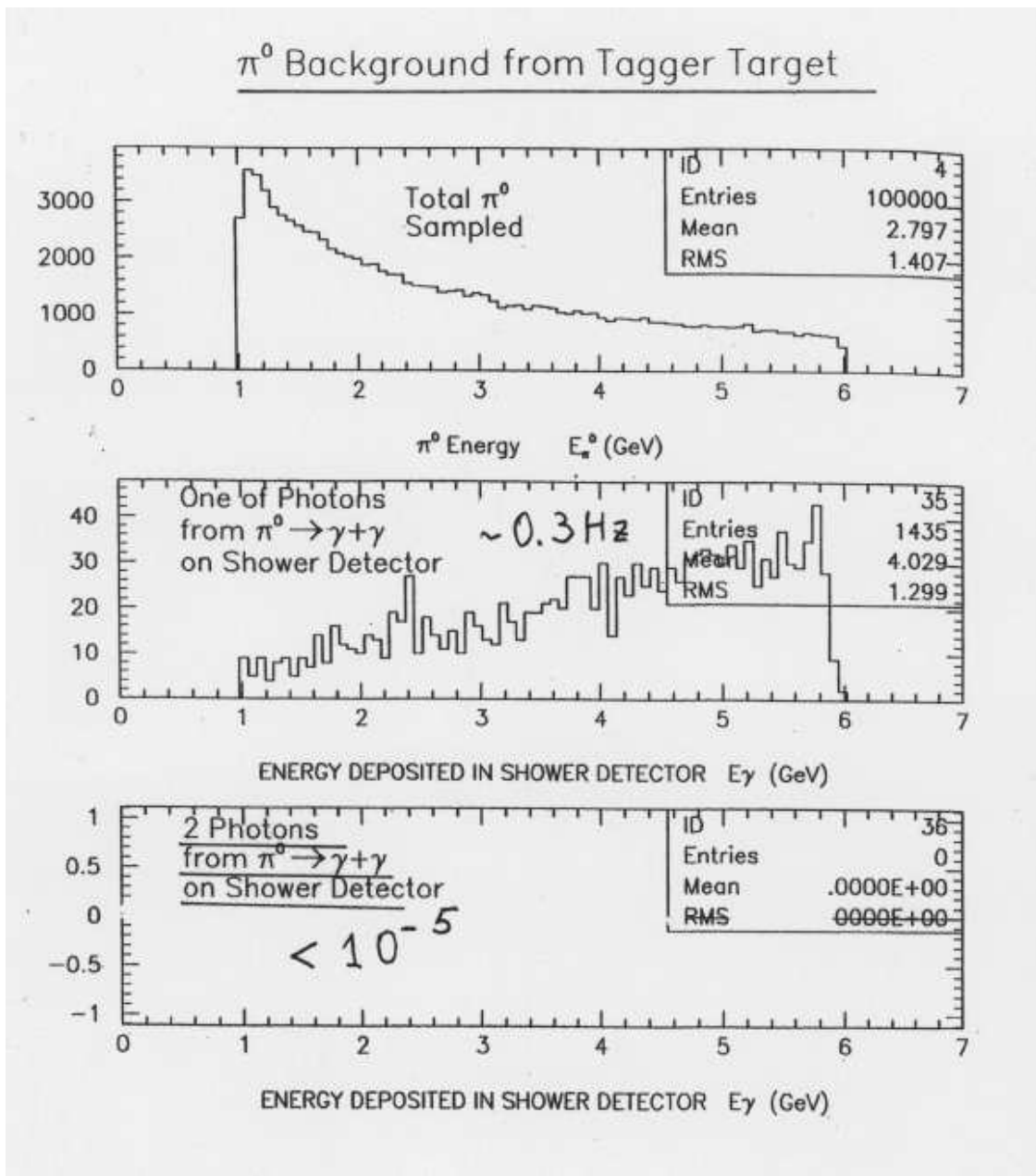


Figure 45: Acceptance of π^0 detector to π^0 's produced upstream of the Primakoff target. (a), energy distribution of photopions. (b), resulting spectrum of single photon events striking detector. (c) illustrates that the two photon acceptance for these pions is negligible.

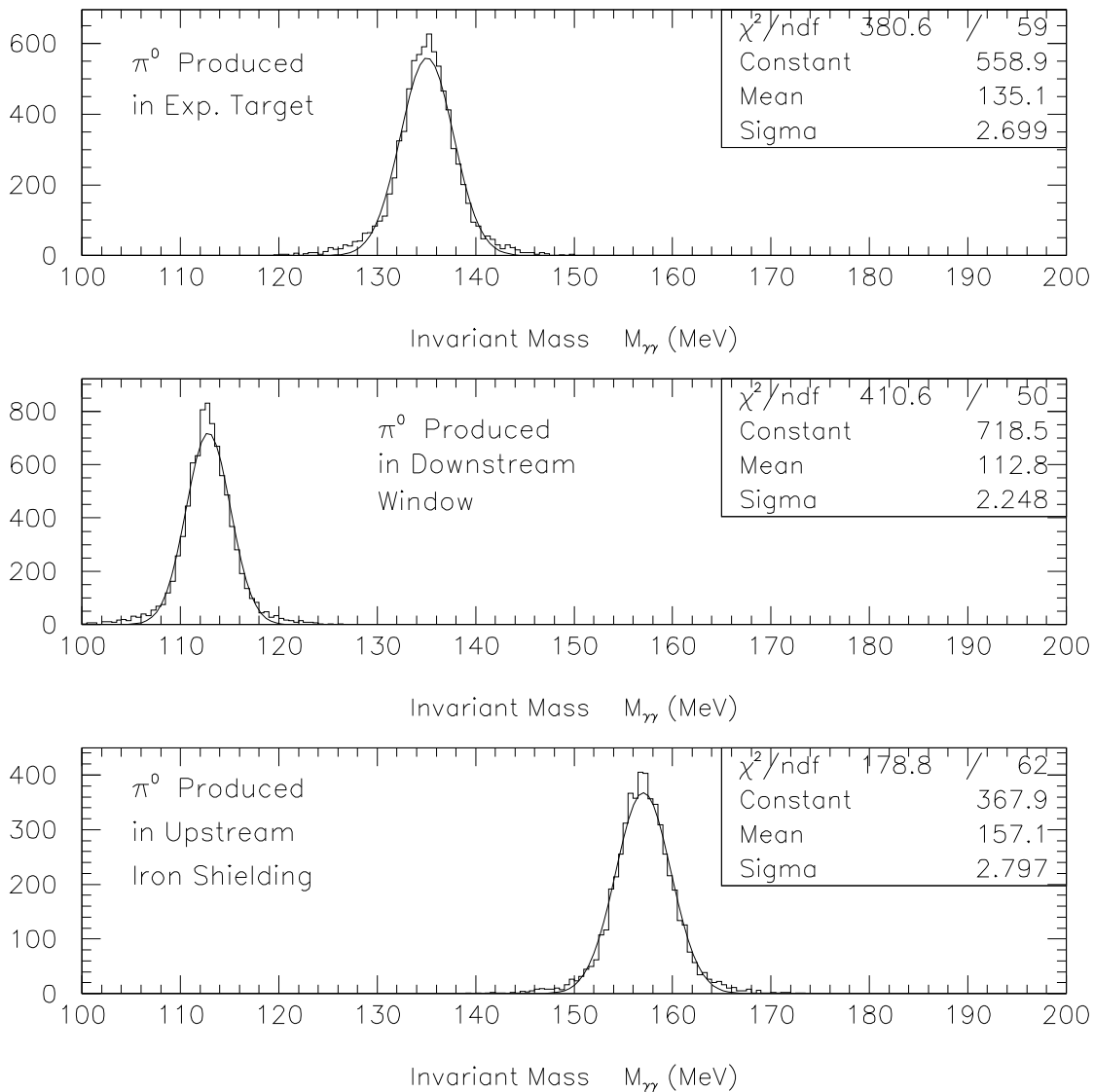


Figure 46: Reconstructed invariant mass distributions for (top), π^0 's produced in the Primakoff target, (middle) in the vacuum window between the Primakoff target and the π^0 detector, and (bottom) those produced in the iron shielding near the exit of the tagger magnet.

coherent pion production cross section (see equation 5) must each be corrected for final state interactions of the outgoing pion[62][63]. Since the pions from the Primakoff effect are produced mostly peripherally, the effect of pion final state interactions on the electromagnetic form factor is small. On the other hand, pions produced within the nuclear interior have a large probability to interact with the nucleus.

The Coulomb form factor is well known and has been calculated in the context of the Glauber theory. Using reference [64] as a starting point, we have performed such a calculation for realistic nuclear charge distributions[56], and modified the calculation for the case of π^0 photoproduction[65]. The electromagnetic form factor is given by:

$$F_{e.m.} = 2\pi q_t \int b^2 db dz J_1(q_t b) \exp\left(-\frac{\sigma A}{2} \int_z^\infty \rho(b, z') dz'\right) (b^2 + z^2)^{-3/2} \int_0^{\sqrt{(b^2+z^2)}} dr r^2 \rho(r) \quad (28)$$

where $\rho(x)$ is the charge density, \vec{q}_t is the transverse momentum transfer to the pion, b is the impact parameter, z is the longitudinal coordinate, and σ is the average pion-nucleon total cross section for the outgoing pion. No distinction is made for the charge and matter densities. We have performed the calculation for ^{12}C and ^{208}Pb using realistic three parameter Woods Saxon distributions with parameters taken from [56]. The results of this calculation with and without distortion are shown in figure 47 for ^{12}C and ^{208}Pb .

Figure 48 illustrates the uncertainty in the distortion-modified Coulomb form factors for (a) ^{12}C , and (b) ^{208}Pb resulting from uncertainties in the measured charge density distributions.

The strong form factor is given by:

$$F_N = F_1 + F_2 \quad (29)$$

F_1 is the usual form factor taking into account nuclear absorption. F_2 , which was neglected in [62], describes the effect of rescattering of photopions. This is of particular interest in the present experiment since pions produced at modest angles can, as a result of final state interactions, rescatter to small angles under the Primakoff peak. F_1 is given by[65]:

$$F_1(q) = \int d^3x e^{i\vec{q}\cdot\vec{x}} \rho(\vec{x}) e^{-A\frac{\sigma'}{2} \int_z^\infty \rho(b, z') dz'} \quad (30)$$

and F_2 is given by:

$$F_2(q) = -\frac{\pi\sigma A}{q_t} \int_0^\infty J_1(q_t) b db \int_{-\infty}^\infty \rho(b, z) dz e^{-\frac{A\sigma}{2} \int_z^\infty \rho(b, z') dz'} \int_z^\infty \frac{d\rho(b, z'')}{db} dz'' \quad (31)$$

The results of the strong form factor so obtained are shown in figure 49(a) and 49(b), and the significance of this sometimes neglected term[62][12], F_2 , is illustrated in figure 50.

4.4 Experimental uncertainties

We intend to control the experimental errors to make a measurement of the π^0 lifetime with a less than 1.5% precision. The various contributions to this error are shown below:

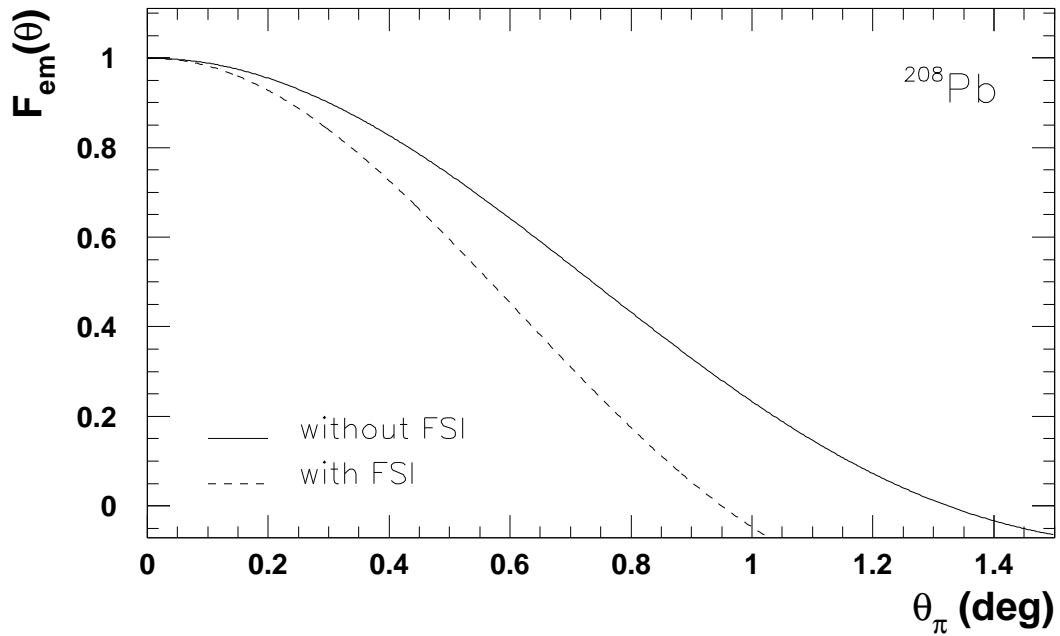
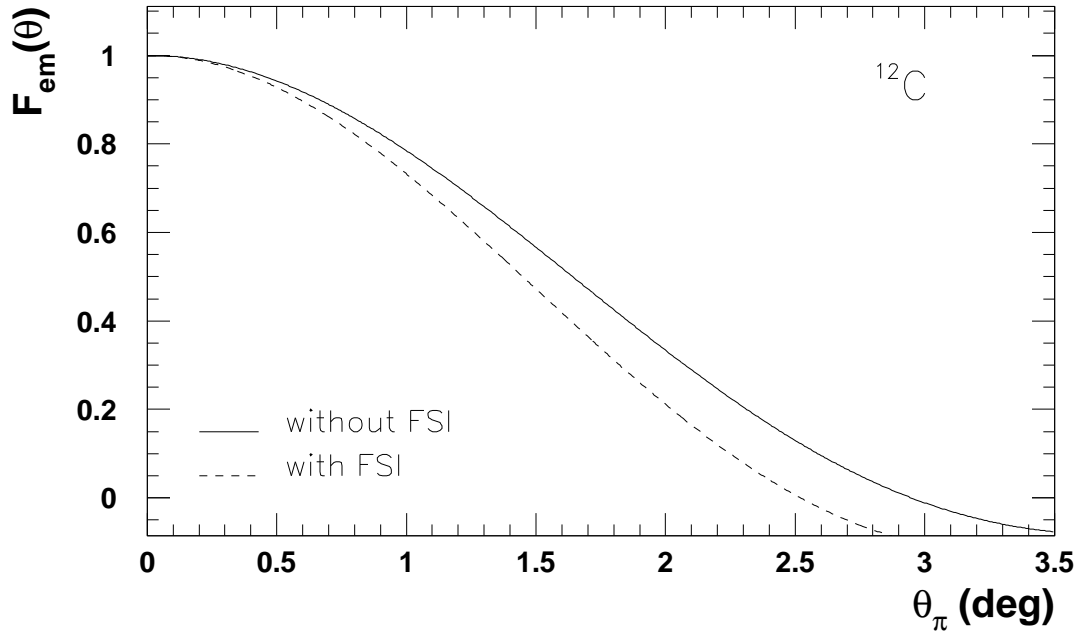


Figure 47: Coulomb form factor with and without distortion for (a) ^{12}C , and (b) ^{208}Pb .

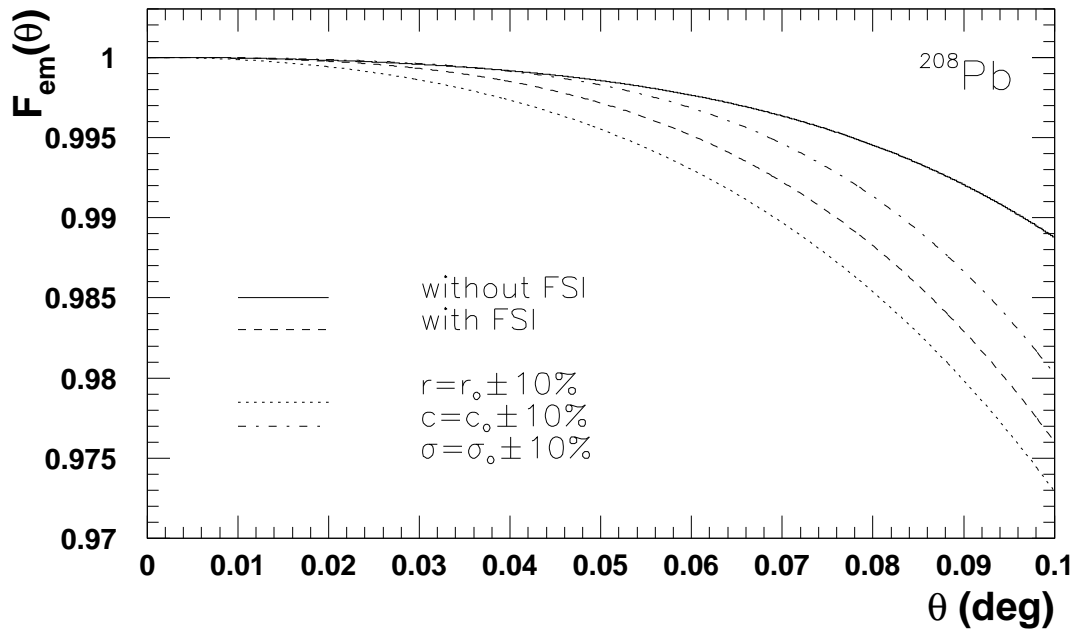
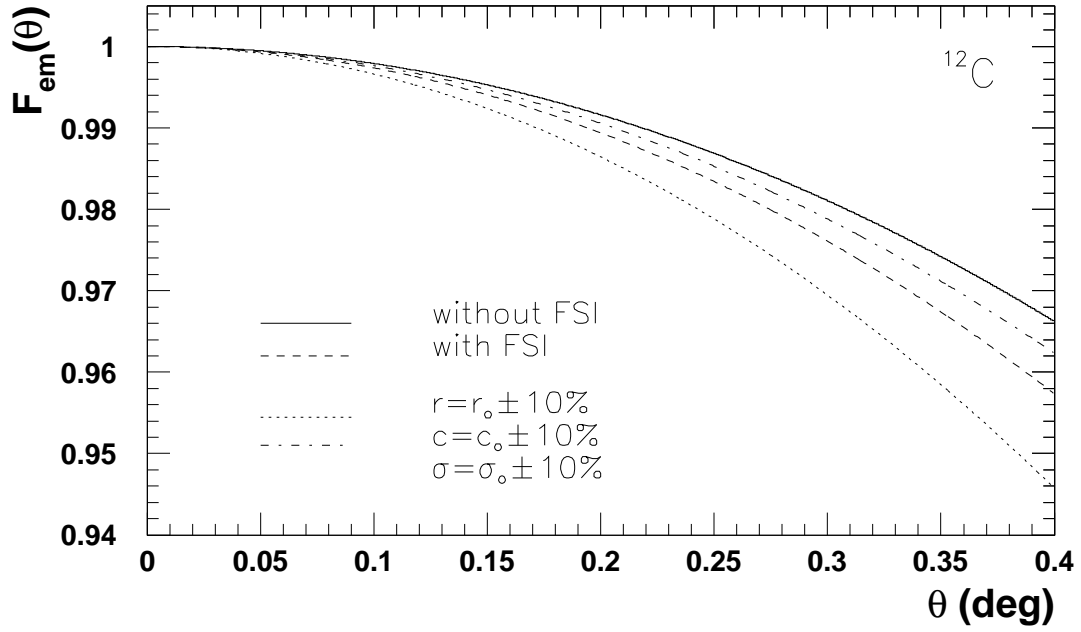


Figure 48: Effect of uncertainties in the Coulomb form factor with distortion due to uncertainties in charge density distributions for (a) ^{12}C , and (b) ^{208}Pb .

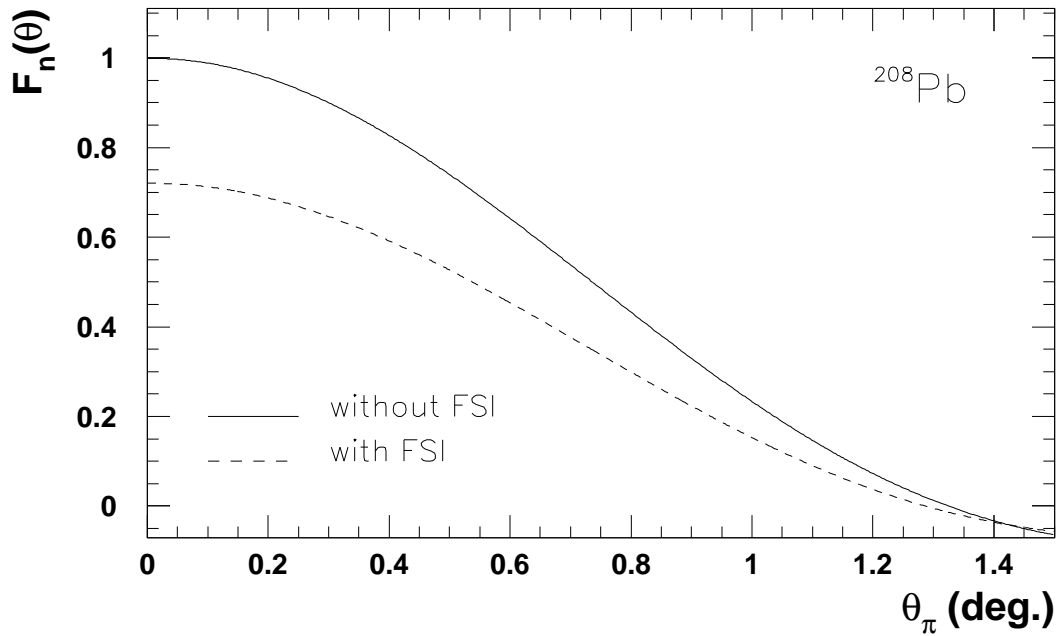
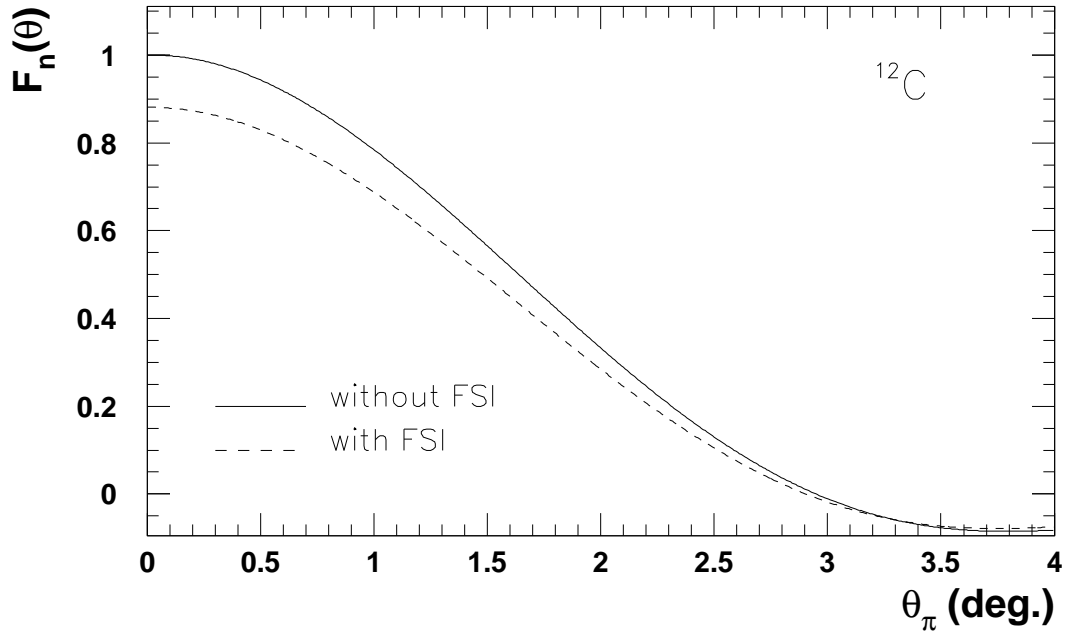


Figure 49: Strong form factor with and without distortion for (a) ^{12}C , and (b) ^{208}Pb .

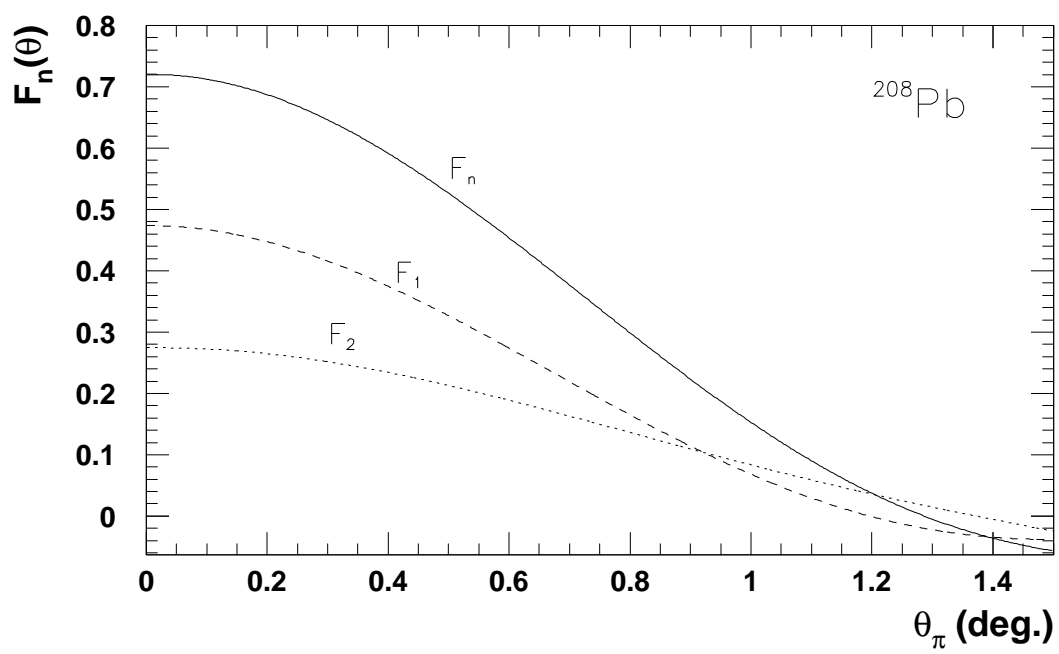


Figure 50: F_1 and F_2 for ^{208}Pb .

statistical	0.4%
target thickness (atoms/cm ²)	0.7%
photon flux	1.0%
π^0 detector acceptance and misalignment	0.4%
background subtraction	0.2%
beam energy	0.2%
distorted form factor calculation errors	0.4%
total	1.4%

The total error was estimated by adding the individual errors in quadrature, and represents the expected pion lifetime error from a combined fit of the three Primakoff targets. The errors that are presented are meant to be conservative, *i.e.* we anticipate that we should do no worse than the values given here.

The absolute photon flux will be monitored by measuring the tagging efficiency about once per day. The pair production luminosity monitor will be calibrated against the rates of the tagger at low beam currents, and will provide continuous real time relative monitoring throughout the data taking. We will also explore the possibility of making an absolute measurement of the luminosity via pair production in the target using a theoretical calculation of pair production which is expected to be accurate to better than 1%[72].

The targets for this experiment are ¹²C, ¹¹⁶Sn, and ²⁰⁸Pb, each with thickness 0.05 radiation lengths. The nuclear form factor will be fit to the data at the larger θ_{π^0} 's and, therefore, its uncertainty will contribute to the statistical error. Errors in the electromagnetic form factor originate from both uncertainties in the nuclear charge distributions and distortion effects. These isotopes were chosen in part because the ground charge densities have been measured in model-independent analyses of electron scattering data, and accurate knowledge of the charge density minimizes the uncertainty in the Primakoff vertex due to the charge form factor[66-71].

The π^0 detector acceptance uncertainty arises primarily from edge effects relating to the position resolution in the blocks near the edges of the detector. The edge effects are minimized by excluding the two outermost and innermost layers of lead glass blocks from the fiducial volume. We will control detector offsets to the 0.75 mm level in two ways. First, accurate surveying will fix the π^0 detector position with respect to the Hall. Second, position asymmetries of the photon singles on the detector will be sensitive to offsets with respect to the photon beam and will enable software alignments.

In estimating errors in background subtractions, a 30% uncertainty in calculated background π^0 rates was assumed. The effect of the beam energy uncertainty on the extracted lifetime arises from the energy dependence of the Primakoff cross section. With the Hall B tagger, we will be able to control the energy to 1×10^{-3} .

In conclusion, we believe that the error estimates given in the above table are robust. We believe that these or somewhat smaller errors can be achieved. We have discussed the individual ingredients in this section. We also would like to emphasize what was presented

in Section 3, namely that the study of the Primakoff peak as a function of Z , photon energy, and pion angle should add a great deal of confidence to the measurement and can be used to empirically determine the systematic errors.

5 Collaboration Management

Collaboration meetings will be held on a regular basis to facilitate communication between collaboration members. The collaboration itself will be managed by a Project Manager and a Steering Committee. The Project Manager's responsibilities will include supervision of the budget and all aspects of detector construction, and the monitoring of grant funds released to member institutions of the collaboration.

A Steering Committee will be formed to assist the Project Manager in the organization and management of the project. The Steering Committee will also provide governance for the collaboration between collaboration meetings. The committee will consist of those experiment spokesmen not serving in the capacity of Project Manager, plus a representative from Jefferson Lab. The Project Manager will be an ex officio member of the Steering Committee.

The experiment spokespersons serving on the Steering Committee are Daniel Dale (U. Kentucky), Samuel Danagoulian (North Carolina A&T State U), and Rory Miskimen (U. Massachusetts). The University of Kentucky has prime responsibility for photon beam luminosity monitoring, N. Carolina for the laser calibration system, and U. Massachusetts for the targets and DAQ electronics.

Ashot Gasparian will serve as Project Manager for the collaboration. Dr. Gasparian is a senior research scientist at Hampton University and is resident onsite at Jefferson Lab. Hampton University is the member institution with primary responsibility for the construction and assembly of the calorimeter.

The distribution of tasks within the Collaboration is summarized in the table in the following section.

6 Institutional Responsibilities

	Task description	Institution	Contact person
1.	Beamline instrumentation; Superharp and target ladder Intensity/Profile on-line monitoring	NC A&T SU. UKy YerPhI JLab,UMass	S. Danagoulian (NC A&T SU.)
2.	Tagged Photon system	Catholic U. GWU	D. Sober (Catholic U.)
3.	Pair spectrometer and Photon flux control	UKy, EKy U. Catholic U. NSU NC A&T SU.	D. Dale (UKy)
4.	Dipole: Vacuum box Magnetic field mapping	UKy NC A&T SU. Catholic U. KIPT Kharkov	D. Dale (UKy) L. Gan (Hampton U.)
5.	Targets	UMass	R. Miskimen (UMass)
6.	Electromagnetic hybrid calorimeter	Hampton U. ITEP Moscow NSU JLab	A. Gasparian (Hampton U.)
7.	Veto detector system	UMass	R. Miskimen (UMass)
8.	Light monitoring system	NC A&T SU.	S. Danagoulian (NC A&T SU.)
9.	Fast trigger, data acquisition	UMass UVA JLab	D. Lawrence R. Miskimen (UMass)
10.	Experiment optimization Monte-Carlo simulation	Hampton U. NC A&T SU. YerPhI UMass MIT NC Central U. Tomsk U. KIPT Kharkov	A. Gasparian (Hampton U.) D. Lawrence (UMass)
11.	On-line and off-line software development	UMass Hampton U. NC A&T SU.	D. Lawrence (UMass)

7 Milestone Schedule

	Task description	1999	2000				2001				
		4	1	2	3	4	1	2	3	4	
1.	Beamline instrumentation — Superharp & target box design order parts installation — Int.-profile mon. design & construction beam tests — Helium bag design installation		xxx xxx	xxx	xxx						
2.	Dipole deliver install — Vacuum box design build install — Magnetic field mapping prelim map final map — Power supply deliver install	xxx xxx xxx xxx		xxx		xxx xxx					
3.	Hybrid calorimeter — Lead glass detectors protype test deliver to JLab assemble beam tests — Lead tungstate crystals assemble prototype beam test order module assembly assembly in frame — Frame design construct	xxx xxx xxx xxx	xxx xxx	xxx xxx	xxx xxx	xxx xxx	xxx xxx		xxx		

	Task description	1999	2000				2001			
		4	1	2	3	4	1	2	3	4
4.	Targets — Targets X-ray scanner order measure	xxx		xxx	xxx					
5.	Veto scintillators prototype design construct beam tests	xxx	xxx	xxx	xxx	xxx				
6.	Light monitoring system order parts assembly test				xxx	xxx	xxx		xxx	
7.	Pair Spectrometer detectors design & construct support install support order detectors & electronics build detectors install detectors beam tests	x	xxx		xxx	xxx	x	x		
8.	Fast trigger and Data acquisition test analog delay DAQ prototype tests order UVA modules & cables assembly and debugging	xxx	xxx	xxx	xxx	xxx	xxx			
9.	On-line and off-line software development	xxx	xxx	xxx	xxx	xxx	xxx	xxx	xxx	
10.	Monte-Carlo simulation	xxx	xxx	xxx	xxx	xxx	xxx	xxx	xxx	xxx
11.	Experiment ready								xxx	xxx

8 Manpower Summary

A summary of the total manpower committed to the PrimEx experiment by its collaborators, in units of FTE's, is given in table 15.

Institution	Faculty	Research Scientist	Post-doc	student
Hampton University	0.2	0.5	1.0	2.0
University of Massachusetts	0.3		0.65	1.2
N.C. A& T SU	0.5		0.5	1.5
University of Kentucky	0.4		0.5	1.2
MIT	0.2	0.1	0.2	
Catholic University	0.1		0.15	
ITEP		2.0	0.5	0.5
Norfolk State University	0.4			0.5
Yerevan Physics Institute		0.5		0.5
Kharkov		0.25		0.25
University of Virginia	0.1	0.25		
North Carolina Central University	0.1			
Eastern Kentucky University	0.1			0.1
Tomsk Polytechnical University		0.25		0.25
total				

Table 15: Summary of total manpower for the PrimEx experiment.

9 Budget Summary

System/Item	PrimEx Request	JLab	Collaboration	Other
Beamline	\$25.0k	\$49.0k		\$83.0k
On-line Profile Monitor	\$15.0k			
Superharp/Target Ladder		\$14.0k		
Dipole/Power Supply				\$83.0k (BNL)
Shipment		\$5.0k		
refurbish and install		\$15.0k		
Vacuum Box		\$15.0k		
Helium Bag	\$10.0k			
Pair luminosity mon.	\$59.0k	\$36.0k	\$9.34k	
First Stage (4 telesc.)		\$36.0k		
Second Stage (8 telesc.)	\$59.0k		\$9.34 (UKy)	
Primakoff targets	\$15.8k		\$2.0k (UMass)	
HYCAL detector	\$416.0k	\$280.0k	\$590.0k	
Prototyping			\$40.0k(HU)	
Lead Tungstate detector	\$396.0k			
Lead glass detectors		\$180.0k	\$550.0k(ITEP)	
Frame		\$100.0k		
other	\$20.0k			
Veto Counter	\$25.9k			
Gain Monit. system	\$63.4k			
DAQ Electronics	\$355.3k	\$37.0k	\$19.1	\$168k
ADC(24 LRS 1881M)				\$168k (FNAL)
Fastbus crate w/contr.		\$22.0k		
CAMAC crate w/contr.			\$9.0k	
NIM bins	\$16.0k			
Electr. racks(5)		\$15.0k		
High Voltage 384 chan.	\$133.6k			
other	\$205.7k		\$10.1k	
Total	\$960.4k	\$402.0k	\$620.3k	\$251.0k

10 Summary

With a measurement of the neutral pion two-photon decay width, we are proposing a precision experimental test of the QCD axial anomaly, which is the only essentially parameter-free prediction of that theory. This experiment will reduce the present $\simeq 10\%$ uncertainty to $\simeq 1.4\%$, and is arguably one of the most important experiments that can be performed at the present TJNAF energy.

This experiment will use the high intensity, high energy photon tagging facility in Hall B, an array of lead glass detectors with a high resolution, and a PbWO_4 crystal insert. The experiment requires tight control of the systematic errors, made possible by the superior π^0 detection and knowledge of the absolute value of photon energies and fluxes provided by both the high quality TJNAF electron beam and the photon tagging facility in Hall B. Accordingly, we were awarded 22 days of beam time at 6 GeV, 7 days for carbon and 6 days of data taking each for the ^{116}Sn and Pb targets, and 3 days of empty target and detector calibration runs. Major new equipment for this experiment includes a multichannel hybrid lead glass/ PbWO_4 π^0 detector and a 1.5 Tesla·m dipole magnet for use as a sweeping magnet and pair production luminosity monitor.

References

- [1] See *e.g.* Dynamics of the Standard Model, J.F. Donoghue, E. Golowich, and B.R. Holstein, Cambridge University Press (1992).
- [2] J.S. Bell and R. Jaciw, Nuovo Cimento 60A, 47 (1969). S.L. Adler, Phys. Rev. 177, 2426 (1969).
- [3] R.M. Barnett *et al.*, Review of Particle Physics, Phys. Rev. D54,1 (1996).
- [4] J. Bijnens, A. Bramon and F. Cornet, Phys. Rev. Lett. 61 (1988) 1453.
- [5] J.F. Donoghue, B.R. Holstein, Y.C.R. Lin, Phys. Rev. Lett., vol. 55, (1985), 2766; J.F. Donoghue, B. Wyler, Nucl. Phys., B316, (1989), 289.
- [6] J. Bijnens, J. Prades, Z. Phys. C64, (1994), 475. J.Bijnens, private communication.
- [7] A.M. Bernstein, Nucl. Phys. A623 (1997) 178c.
- [8] D. Dale, A. Gasparian, Proposal to TJNAF PAC12, E-97- 009,(1997).
- [9] H.W. Atherton *et al.*, Phys. Lett., vol. 158B, no. 1, (1985), 81.
- [10] H. Primakoff, Phys. Rev. 81, 899 (1951).
- [11] A. Browman *et al.*, Phys. Rev. Lett., vol. 33, (1974),1400.
- [12] G. Bellettini *et al.*, Il Nuovo Cimento, vol. 66, no. 1, (1970), 243.
- [13] V.I. Kryshkin *et al.*, Sov. Phys. JETP, vol. 30, no. 6, (1970),1037.
- [14] G. Bellettini *et al.*, Il Nuovo Cimento, vol. 40, no. 4, (1965), 1139.
- [15] A. Browman *et al.*, Phys. Rev. Lett., vol. 32(1974) 1067.
- [16] D.A. Williams *et al.*, Phys. Rev. D, vol. 38, no. 5, (1988), 1365.
- [17] G. von Dardel *et al.*, Phys. Lett., vol. 4, no. 1, (1963), 51.
- [18] International Workshop on the Structure of the η Meson (1966), World Scientific, M. Burkardt, J. Goity, V. Papavassiliou, and S. Pate, editors.
- [19] E.P. Venugopal and B.R. Holstein, Phys. Rev. D, vol. 57, no. 7, (1998), 4397.
- [20] See *e.g.* D. Babusci *et al.*, Phys. Lett. B277 (1992) 158.
- [21] For a review of the theory see H. Bijnens in Chiral Dynamics: Theory and Experiment Springer Lecture Notes in Physics, Vol 513, A.M. Bernstein, D. Drechsel, and Th. Walcher, editors.

- [22] For a review of the past and possible future experiments on the two photon reaction producing two pions see The DAΦNE Handbook, INFN Frascati Report (1992), L. Maini, G. Panceri, and N. Paver editors.
- [23] M.K. Jones, *et al.* and the Hall A Collaboration, submitted to Phys. Rev. Lett., Oct. 5, 1999.
- [24] S.F. Pate, V. Papavassilou, G. Kyle, Proposal for Time and Gain Monitoring for G^0 . New Mexico State University (1997). S.F. Pate, private communication.
- [25] L. Bartozek *et al.*, NIM A301 (1991), 47.
- [26] T. Hehl *et al.*, NIM A354 (1995), 505.
- [27] M. Kobayashi and S. Sugimoto, KEK Preprint 83-9 (1983).
- [28] A. Ahmidouch, PhD thesis, Université de Genève (1992).
- [29] Hewlett Packard optoelectronics catalogue.
- [30] Hewlett Packard catalogue, www.hp.com/HP-COMP/led_lamps/hlmpcb15.html.
- [31] Murray Moinester, Private communication, COMPASS/SELEX Technical Reports, FNAL E781 H-688 (1995).
- [32] J.S. Bell *et al.*, Il Nuovo Cimento, vol. 51, no. 1, (1969), 47.
- [33] S. Adler, Phys. Rev., vol. 177, no. 5, (1969), 2426.
- [34] J. Bijnens *et al.*, Z. Phys. C, 46, (1990), 599.
- [35] A.M. Bernstein, Nucl. Phys. A623 (1997) 178c.
- [36] R.M. Barnett *et al.*, Review of Particle Physics, Phys. Rev., D54, (1996), 21.
- [37] See, *e.g.* Dynamics of the Standard Model, J.F. Donoghue, E. Golowich, and B.R. Holstein, Cambridge University Press (1992).
- [38] G. Bellettini *et al.*, Il Nuovo Cimento, vol. 40, no. 4, (1965), 1139.
- [39] D.I. Sober, A Guide to the Optics of the Tagged Photon Magnet, CLAS Note 91-012.
- [40] J. Arends, M. Breuer, H.D. Dahmen, P. Detemple, W. Schneider, D. Urban and B. Zucht, NIM A306 (1991), 89.
- [41] G.A. Alexeev, *et al.*, NIM A364, (1995), 307.
- [42] H. Stroher, G. Koch, V. Metag, R. Beck, B. Schoch, J. Vogt, NIM A269 (1988), 568.

- [43] Proposal for a High Resolution Spectrometer for Neutral Mesons, Los Alamos National Laboratory, December 1989.
- [44] B. Powel *et al.*, Nucl. Instr. and Meth., 198, (1982), 217.
- [45] A.S. Aleksanian *et al.*, Preprint YerFI-1239-25-90, (1990).
- [46] K. Mengel, R. Novotny, R. Beck, *et al.*, "Detection of Monochromatic Photons Between 50 and 790 MeV with a PbWO₄ - Scintillator Array", to be published (1999).
- [47] D.I. Sober, private communication.
- [48] T.J. Brodbeck, P. Coddington, J.V. Morris, D. Newton, T. Sloan, Nucl. Phys B136 (1978) 95.
- [49] J. Ballam, G.B. Chadwick, Z.G.T. Guiragossian, A. Levy, M. Menke, P. Seyboth, G. Wolf, Phys. Lett., vol. 30B, no. 6 (1969) 421.
- [50] Y. Eisenberg, B. Haber, Carmel, E. Peleg, E.E. Ronat, A. Shapira, G. Vishinsky, R. Yaari, G. Yekutieli, Phys. Rev. Lett., vol. 22, no 13 (1969) 669.
- [51] Y. Eisenberg, B. Haber, E.E. Ronat, Y. Stahl, G. Yekutieli, J. Ballam, G.B. Chadwick, M.M. Menke, P. Seyboth, A. Shapira, J. Gandsman, J. Grunhaus, A. Levy, Phys. Lett., vol. 34B, no. 5 (1971) 439.
- [52] D.O. Caldwell, V.B. Elings, W.P. Hesse, R.J. Morrison, F.V. Murphy, Phys. Rev. D, vol. 7, no. 5 (1973) 1362.
- [53] T.H. Bauer, R.D. Spital, D.R. Yennie, Rev. Mod. Phys., vol. 50, no. 2 (1978) 261.
- [54] P.L. Braccini, C. Bradaschia, R. Castaldi, L. Foa, K. Lubelsmeyer, D. Schmitz, Nucl. Phys. B24 (1970) 173.
- [55] H.-J. Behrend, F. Lobkowicz, E.H. Thorndike, A.A. Wehmann, Phys. Rev. Lett., vol 24, no. 22 (1970) 1246.
- [56] C.W. de Jager, H. de Vries, C. de Vries, At. Data and Nuc. Data Tables, vol. 14, no. 5 (1974) 480.
- [57] J.B. Bellicard and K.J. van Oostrum, Phys. Rev. Lett., vol. 19, no. 5, (1969) 242.
- [58] G.J.C. van Niftrik, Nucl. Phys. A131, (1969), 574.
- [59] J. Heisenberg, R. Hofstadter, J.S. McCarthy, I. Sick, B.C. Clark, R. Herman, D.G Ravenhall, Phys. Rev. Lett., vol. 23, no. 24. (1969), 1402.
- [60] J. Friedrich, F. Lenz, Nucl. Phys. A183 (1972), 523.
- [61] H. Euteneuer, J. Friedrich, N. Voegler, Phys. Rev. Lett., vol. 36, no. 3, (1976) 129.

- [62] G. Morpurgo, Nuovo Cimento, 31, (1964), 569.
- [63] C.A. Engelbrecht, Phys. Rev. 133, (1964), 988.
- [64] G. Faldt, Nucl. Phys. B43, (1972),591.
- [65] S. Gevorgyan, private communication.
- [66] L.S. Cardman *et al.*, Phys. Lett. 91B, 203 (1980).
- [67] W. Reuter, *et al.*, Phys. Rev. C26, 806 (1982).
- [68] I. Sick, Phys. Lett. 116B, 212 (1982) .
- [69] J.M. Cavedon, *et al.*, Phys. Lett. 118B, 311 (1982) .
- [70] B. Frois, *et al.*, Phys. Rev. Lett. 38, 152 (1977).
- [71] H. Euteneuer, *et al.*, Nucl.Phys. A298, 452 (1978).
- [72] L. Maximon, private communication.
- [73] A. Margarian *et al.*, Direct Measurement of the Lifetime of the Heavy Hypernuclei at CEBAF. JLAB Experiment E-99-003.